DEDICATION

This thesis is dedicated to my father;

MICHAEL OGUNLEYE OTOKITI

the fountain of all my aspirations, who died just as I commenced this work, and to those affected by his death.

A STUDY OF THE VACUUM STREAM DEGASSING OF MOLTEN IRON

A Thesis

presented for the degree of Doctor of Philosophy

of the

University of London

and

Diploma of Imperial College

by

Ajibade Ogunleye

John Percy Research Group
in Process Metallurgy,
Department of Metallurgy &
Materials Science,
Imperial College of Science
& Technology, Prince Consort
Road, London SW7 2BP.

May 1976.

A B S T R A C T

Some practical and fundamental aspects of stream degassing of gas-saturated molten iron, involving the spontaneous nucleation and growth of gas bubbles in both smooth and rough nozzles were studied.

Pure iron saturated with different gases at one atmosphere was discharged through nozzles, of different roughness and length-diameter ratios, into an evacuated chamber at low pressures down to 10^{-3} mmHg.

The apparatus allowed inspection of the stream as it emerged from the nozzle. High speed cine photographs of the streams were taken. Because of the rather low discharge coefficients obtained, auxiliary experiments were carried out with oxygen saturated and degassed silver contained in alumina tube to permit a realistic correlation between the present work and the earlier model studies.

Break-up of nitrogen saturated molten iron was limited by the combined effect of the low solubility and diffusivity of the gas in the liquid. The break-up of hydrogen saturated iron occurred readily to an extent depending on the availability of suitably sized refractory pores for the spontaneous nucleation of gas bubbles. The saturation of the melt with various mixtures of

$CO - CO_2$ posed major experimental problems arising from the chemical attack of the alumina materials.

The Fe - C - O and Fe - N - S investigated indicated that the amount and nature of adsorbed species were very important for stream break-up to occur.

The results demonstrate that in the rough nozzles the flow characteristics were too poor to be used as a basis for modelling flows in larger nozzles.

Suggestions and recommendations for future work to circumvent the materials problems and to identify the current work with industrial practice are made.

LIST OF TABLES

Number Page

LIST OF FIGURES

Page

TABLE OF NOTATION

TABLE OF NOTATION

Arabic Symbols

a	cross sectional area of nozzle
A	cross sectional area of crucible
A	interfacial area
C	concentrations
C_{fm}	mean friction factor
C_D	discharge coefficient
d	nozzle diameter
D_X	diffusivity of X
e	mean height of roughness projections inside nozzle
E	$(1 - \rho_g / \rho_L)$
f_X	Henrian activity coefficient of X
g	gravitational acceleration
G	mass flux density
G	Gibbs free energy
h	depth of liquid metal
h_X	Henrian activity of X
I	nucleation frequency (as for 3.40)
k	mass transfer coefficient
k	Boltzmann constant
K_L	entry loss coefficient
K	equilibrium constant
l	nozzle length

l_c cavity depth

m,n constants

M mass of charge

ΔP pressure difference

P pressure

$P_a + \rho_L g h$ nozzle entry (upstream) pressure

Q volumetric flow rate

r bubble radius

r_c crucible radius

R bubble radius

S fractional rate of random surface renewal

v velocity

V volume

Δt time interval

t time

T temperature, °K

$\underline{X}$, [X] dissolved X

Greek Symbols.

β growth rate constant (equ. 5.3)

Θ growth rate parameter (equ. 6.16)

δ boundary layer thickness

δ gas/liquid volume ratio

ρ_L liquid density

ϕ defined by equation 3.45

Ξ dimensionless surface tension (equ. 3.46)

θ contact angle

τ dimensionless growth time

σ surface tension

Δ overall change

ν kinematic viscosity

μ dynamic viscosity

Subscripts.

a atmospheric pressure

b bulk saturation

e exit of nozzle

e equilibrium (concentration)

g referred to gas phase

L referred to liquid phase

m mean

o embryo radius

o critical state

s referred to solid phase

s surface saturation

t total (pressure drop)

v vacuum pressure

Superscript

* denoting critical state

Abbreviations

OFN oxygen-free nitrogen gas

PTFE polytetrafluoroethylene

TABLE OF CONTENTS

CHAPTER 1: INTRODUCTION

CHAPTER 1. INTRODUCTION.

The increasing demand for higher quality materials, at lower costs, poses a challenge to the process metallurgist: the attainment of higher process efficiency through the unambiguous understanding of the sequence and specific role of the process parameters.

Commercial application of large-scale liquid state vacuum treatment is almost exclusively limited to steelmaking. The vacuum degassing process of molten steel has shown popularity in the manufacture of 'killed steel' ingots for forging qualities where the normal hydrogen content of the steel would require prolonged heat treatment to eliminate the danger of the formation of internal cracks that can occur up to several weeks after casting. The process is also employed for fully 'killed' bearing-manufacturing qualities and for thick rolling stock.

More recent applications include vacuum carbon deoxidation of 'unkilled' steels so that when deoxidisers are subsequently added the quantity of nonmetallic inclusions formed is reduced.

An up-to-date historical survey of the numerous proposals, their developments, essential features and commercial applications was recently published (1). The principal degassing processes employed commercially in steel-

making include:

(1) Circulation and vacuum lift degassing;

(2) Ladle degassing;

(3) Stream degassing.

An insight into the relative importance of these processes in world vacuum degassing may be gained from the statistics given in Table 1.1 (2), (2a).

Type	No. of units	Annual Capacity (10^5Kg)
Undisclosed Ingot	5)) 6)	2.07
Circulation and vacuum lift	36	37.63
Ladle	67	28.66
Stream	126	77.85
Total	240	146.21

Table 1.1

RELATIVE IMPORTANCE OF THE MAJOR DEGASSING PROCESSES IN 1967.

It is a common knowledge that the amounts of hydrogen, nitrogen and oxygen found in vacuum stream degassed steels are all much in excess of the equilibrium quantities. Steel streams degassed at 0.1 mm-Hg. are known to contain H, N, O that would be in equilibrium with 1-5 mm Hg, 3-10 mm Hg. and 60-150 mm Hg. of H_2, N_2, CO respectively. Apart from the implied low process efficiency the process appears more effective for hydrogen removal than for nitrogen removal and carbon deoxidation.

The principal and common feature of all the variants of stream degassing process is the disintegration of the metal stream into fine droplets as it enters into an evacuated chamber. The finer the droplets, the greater is the overall surface area of metal exposed to vacuum, and the more efficient is the degassing process.

The logical question is, what parameters significantly enhance the attainment of optimum stream disintegration? The roles played by nozzle characteristics and gas content of the molten iron are likely to be of particular importance.

The main drawback of stream degassing process is the considerable heat loss during the process. This requires a high degree of charge superheat with attendant excessive

furnace wear and an increase in the likelihood of refractory inclusions entering the steel. This is the main reason why the stream degassing processes have been falling in popularity recently. (1a)

One of the essential requirements for the acceptance of a research proposal is that the experimental conditions must be controllable with a high degree of precision (3); as a result many university-based projects simulating high temperature industrial processes have been limited to room temperature model studies. In addition, work at room temperature avoids the materials problems invariably accompanying high temperature studies. However many governments (4), industrial establishments, and their agencies have often criticised pure science research and model studies and are in favour of applied research projects closely identifiable with specific industrial problems.

Richardson, Bradshaw and Warner (5) initiated the stream degassing project at Imperial College. Mizoguchi, Baxter and Robertson (6) have done further work. Of particular interest is the work of Mizoguchi on silver-oxygen system with the molten metal contained either in 'Nimonic 75' or 'Inconel 600'. He concentrated mainly on the measurement of flow rates and on the nucleation and growth of bubbles in the nozzle.

In the current work our objectives were twofold:

(1) Using molten iron containing dissolved gases to follow up the model studies undertaken earlier to obtain a correlation and an assessment of their general applicability, and

(2) to concentrate on the break-up downstream of the nozzle exit in the vacuum chamber.

The main emphasis was placed on the 'mission orientated' attempts to establish a more realistic laboratory investigation of an industrial problem. The investigations were to be confined mainly to the spontaneous nucleation and growth of bubbles in refractory nozzles from dissolved gases.

The thesis will contain a review of closely related previous work; in chapter three, theoretical background to thermodynamics and kinetics relevant to vacuum degassing, bubble nucleation and growth will be summarised.

Because of the decision to study the degassing of molten iron, it was necessary to design a special apparatus. The design and the philosophy on which it was based will be described in chapter four. Despite successful preliminary experiments, results obtained during the final phase of the programme were limited due to the experimental difficulties encountered - mainly resulting

from the attack of materials by molten iron and crucible failure resulting from the poor thermal shock resistance of alumina. The experimental difficulties are also listed in chapter four.

The results are contained in chapter five. Chapter six contains the analysis, interpretation and discussion of the results which are correlated with similar laboratory studies and relevant plant observations. Comments are made on the industrial significance and possible applications. Chapter seven contains a summary of the conclusions and recommendations and suggestions for future work.

The appendices contain the raw data used for the calculation of discharge coefficient and all related parameters, the data on the kinetics of nitrogen and carbon monoxide bubble growth in molten iron in the vacuum chamber. Comments are made on the kinetics of iron melt saturation originally planned as part of the current programme.

C H A P T E R 2

REVIEW OF PREVIOUS WORK

2.1 SOME RELATED LABORATORY STUDIES

2.2 SOME RELATED INDUSTRIAL OBSERVATIONS.

CHAPTER 2. REVIEW OF PREVIOUS WORK.

2.1 Some Related Laboratory Studies.

Warner (5) (5a) pioneered the current programme. His experiments involved the silver-oxygen and iron-carbon-oxygen systems treated to various levels of saturation. The saturated molten metals were discharged into a vacuum tank through a 5 mm diameter porous refractory nozzle in the case of experiments with molten iron and through a 2 mm diameter by 6 mm long cylindrical 'Nimonic 75' nozzle in the case of silver. He observed the stream behaviour within a field 9-22 cm. downstream of the nozzle exit with a high speed cine-camera. A typical run consisted of about 2.3 kg. mild steel melted under argon in an alumina tube and pre-treated by bubbling into the melt a gas mixture of carbon monoxide and carbon dioxide (10/1) at a flow rate of 0.5 litres/minute for ten minutes. Warner found that explosive disintegration occurred at an initial tank pressure of 0.1-0.2 mm Hg. He reported no break-up of streams in experiments in which the same charge mass and composition was saturated for six minutes and below, and therefore concluded that a critical condition must exist for carbon and oxygen concentrations in molten iron before stream break-up could occur. The melt analysis (shown

in table 2.1) does not seem to justify this conclusion.

There were a number of features of Warner's experiments which were unsatisfactory: the nozzle exit was not visible so that the initial mode of break-up was not directly observed. The large change in stream behaviour between runs after 6 and 10 minutes was greater than expected from the C and O analyses. Furthermore it was unclear whether break-up was caused by entraintment of residual gas in the porous nozzle or by spontaneous bubble growth in the nozzle from the dissolved gas.

Time since the commencement of bubbling (minutes)	C		O	
0	0.00	0.00	0.0404	0.0419
2	0.01	0.01	0.0449	0.049
6	0.01	0.01	0.057	0.056
10	0.02	0.01	0.059	0.060

Table 2.1

TYPICAL ANALYSIS AND SATURATION LEVEL OF WARNER'S IRON MELT.

Mass of charge	:	2.27 kg.
Melted under	:	High purity argon
Charge temperature	:	1600°C
Gas mixture (solute)	:	CO/CO_2 (10/1)
Volumetric flow rate	:	0.5 litres/minute.

Warner showed that for silver saturated with oxygen at partial pressures greater than 0.2 atmosphere and flowing through nozzles of l/d = 3 (Reynolds number, Re = 3000) break-up occurred at tank pressures of the order of 0.5 mm Hg. For pure oxygen-saturated silver flowing through the same nozzle he suggested that maximum disintegration of the stream did not necessarily occur at the lowest tank pressures and that break-up produced from a sharp-edged nozzle was less violent than for streams from a parallel-sided nozzle.

According to Warner only two of the many possibilities of heterogeneous nucleation were feasible in his system: (1) Heterogeneous nucleation in pores and other cavities in the nozzle. The necessary condition for nucleation is that the bubble should not be carried along during its formation by the stream of molten metal before it reaches the critical size.

(2) Heterogeneous nucleation on gas entrained in the nozzle. Warner argued in favour of the latter which could occur within the nozzle if metal streams trapped pockets of gas against the nozzle wall and dragged them into midstream by turbulence and other stream instabilities. They may subsequently grow by diffusion of gas from the surrounding liquid or collapse. He then pro-

posed a kinetic model of bubble nucleation and growth to interpret his observations.

ASSUMPTIONS OF WARNER'S KINETIC MODEL.

(a) A hemispherical gas embryo of radius r_v and pressure P equal to the vacuum tank pressure P_v.

(b) That the bubble is suddenly entrained in the stream, and later grows by diffusion of gaseous species from the surrounding liquid into a spherical shape to form a stable nucleus.

Using Boyle's law and combining this with the relationship between pressure, surface tension and bubble radius we have:

$$P_v V_v = P_o V_o = P_o (4/3\pi r_o^3) \quad \ldots\ldots\ldots\ldots 2.1$$

$$P_o = P_v + 2\sigma/r_o \quad \ldots\ldots\ldots\ldots 2.2$$

Assuming hemispherical cavities of radii 0.05, 0.01 cm Warner evaluated the radius and pressure inside the bubble in the stream for various initial cavity radius and chamber pressure. His calculations revealed that:

(1) At low oxygen saturation (P_{O_2} = 0.05 atm) the bubble nucleus from an entrained gas embryo was unstable.

(2) At P_{O_2} = 0.1 atm the nucleus was stable only at tank pressure close to 10 mm Hg, with embryo radius greater than 0.05 cm.

(3) At higher oxygen saturation the nucleus from an

embryo greater than 0.05 cm. radius was always stable. However, at low tank pressures embryos of radius 0.01 cm. were unstable.

Baxter (6) followed up Warner's work on molten silver but modified the system to enable him to observe the nozzle exit, and used parallel-sided 'Nimonic 75' nozzles of l/d ratios 2.3, 3.0, 6.0 and diameters 6.4, 4.8 and 2.4 mm respectively. He studied the effects of oxygen levels in silver and tank pressure on the stream behaviour by taking high speed cine photographs. His classifications of the observed stream behaviours were:

(1) With degassed silver, contracted single phase flow.

(2) with air-saturated silver at tank pressures of about 1 mm Hg; intermittent bubble growth within an essentially single phase flow.

(3) with oxygen-saturated silver at pressures of about 100 mm Hg and above; intermittent bubble growth within a single phase flow.

(4) with oxygen-saturated silver at pressures of the order of 1 mm. Hg; a violently disintegrated two-phase flow.

Baxter reported increased break-up with air-saturated silver flowing through nozzles of greater l/d ratios.

He did not confirm Warner's observation that maximum break-up occurred at intermediate chamber pressure.

Mizoguchi (7) followedup Baxter's work on molten silver. He investigated the behaviour of pure silver containing various quantities of dissolved oxygen and discharged at atmospheric pressure through rounded-entry 'Nimonic 75' nozzles into a vacuum tank at various pressures. He employed two different types of nozzles of 2.38, 4.76 mm diameter and 1/d ratios 5.33 and 2.67 respectively. Flow rates and static pressures of the stream within the nozzles were measured. He also made observations of the stream behaviour downstream of the nozzle using a high speed camera, and developed a theory correlating the static pressure, the volumetric ratio of gas to liquid, and mass flow rate to confirm choking. He finally estimated the volumetric ratio of the gas forming within the nozzle. The results of his work are summarised below.

(1) The mass flow rate of the degassed silver ($P_{O_2} \sim 10^{-3}$ atm) continuously increased when the total pressure drop, ΔP_t was increased by lowering the tank pressure at constant upstream pressure. The mass flow rate at any total pressure drop,

$$\Delta P_t = \left(P_a + \rho_L gh - P_v \right) \qquad \ldots\ldots\ldots\ldots\ 2.3$$

$P_a + \rho_L gh$ = upstream pressure

P_v = tank pressure.

was found to be 91.5% of that predicted by Bernoulli equation. Observation of the stream in the vacuum chamber showed that the flow was single phase. Static pressure measurement in the nozzle revealed that pressure at nozzle exit was very close to the chamber pressure while that at the midpoint was about 40 mm Hg. higher than the chamber pressure, thereby suggesting frictional pressure drop downstream of the nozzle.

(2) The mass flow rate obtained for air-saturated silver (P_{O_2} = 0.205 atm.) through a 4.76 mm diameter nozzle was the same as of the degassed silver at chamber pressure $P_v \geqslant 100$ mm Hg. but was slightly reduced at P_v of 2-8 mm Hg. The stream exhibited intermittent bubble growth outside the nozzle exit only at chamber pressures of 10 mm Hg. and below, suggesting a pronounced decrease in the rate of bubble nucleation.

(3) Oxygen-saturated silver discharged through the 4.76 mm diameter nozzle featured metastable single-phase behaviour at chamber pressure $\geqslant$ 300 mm Hg. and the relationship between mass flow rate and total pressure drop was the same as for degassed silver. At chamber pressure

$\leqslant$ 200 mm Hg. the mass flow rate was independent of chamber pressure but was dependent on and increased with nozzle entry pressure. Observation of the stream showed homogeneous bubbly flow at chamber pressures $\leqslant$ 100 mm Hg., i.e. the static pressure at the nozzle exit was higher than and independent of chamber pressure; for example it remained at about 180 mm Hg. when the chamber pressure was varied between 10 and 100 mm Hg. This confirmed that the flow was choked.

Mizoguchi then postulated that nucleation mechanism was heterogeneous and occurred on nozzle wall cavities but that the initial growth was suppressed by viscous and inertial effects. The observed bubble growth rate in the stream in the vacuum chamber was in conformity with Scriven's parabolic law of diffusion-controlled growth at chamber pressure of between 200 and 300 mm Hg. At much reduced chamber pressures bubble growth outside nozzle exit was considered too complex for analysis.

Apart from applications to stream degassing in process metallurgy, single and multi-phase flow systems attract interests in other fields, notably chemical and mechanical engineering. It is now generally believed that the flow of superheated liquids in tubes is annular and becomes choked whereas that of oxygen-saturated silver is

homogeneous bubbly flow.

Eisenklam and Hooper (8) investigated and classified the behaviour of water jets, containing no dissolved gases, flowing through glass capillary tubes of different l/d ratios, in terms of their Reynolds number:

(1) For the range $400 \geqslant l/d \geqslant 10$ a glassy section was followed by axisymmetric break-up for $Re \leqslant 3000$.

(2) For $l/d \geqslant 400$, and $3000 \leqslant Re \leqslant 10{,}000$, the flow either remained laminar or changed to turbulent. In the former case a glassy section was followed by the jet atomisation; in the latter a ruffled jet emerged without any atomisation.

(3) At $Re > 12{,}000$ the flow was turbulent and jet disintegration was complete at the tube exit.

(4) For $l/d < 10$, and $3000 \leqslant Re \leqslant 1000$ the flow was semi-turbulent with a characteristic flat velocity profile and assymetric jet break-up supposedly due to air friction.

Using 'Freon 11' saturated with its own vapour at ambient pressure and temperature Min. et al (9) investigated the dependence of critical flow rate and flow regime on nozzle designs and pressure. Their results revealed that :

(i) two-phase choked flow occurred at low downstream

pressures and

(ii) high l/d ratios resulted in lower flow rates.

They classified the flow regimes in terms of a 'modified cavitation number' $\acute{Ca}$ where

$$\acute{Ca} = 2(l/d)(P_b - P_v)\ \rho_L/G^2 \quad \ldots\ldots\ldots\ldots\ 2.4$$

for $\acute{Ca} < 9$; metastable single phase flow

for $9 < \acute{Ca} < 15$; unstable flow

for $15 < \acute{Ca}$; two phase choked flow.

Charan (10) investigated the two-phase non-equilibrium flow of dichlorodifluoromethane through a round-entry nozzle and revealed that the flow was sensitive to nozzle design, particularly to orifice entry radius if not well rounded. He observed choking with lagged nozzles as lagging prevented heat transfer to the evaporating steam from the nozzle wall. With unlagged nozzles the results showed an increase in flow rate with decreasing downstream pressure because of the additional evaporation caused by heat transfer.

Silver and Mitchell (11) investigated the critical behaviour of superheated water varying the downstream pressure between 0 and 25 psig. at constant upstream pressure of 30 psig. The critical static pressure at the nozzle exit, measured with pressure tapping nozzle, agreed with theoretical predictions and was well above

and independent of the downstream pressure. Choking was confirmed when the downstream pressure was lowered at a constant upstream pressure.

Simpson and Silver (12) considered the nucleation of vapour bubbles at a frequency determined in accordance with nucleation theory,and a growth rate determined by heat conduction in the liquid using Reiss and Frankel's heterogeneous nucleation theory for vapour nucleation in superheated liquids. They derived a parabolic growth equation which they combined with the momentum equation. The resulting theory predicted choking and also a large pressure gradient in the nozzle close to its exit.

Fauske (13) investigated the critical two-phase flow in steam-water system. Using an annular flow model he developed a theory which predicted a relationship between critical mass flow rate and critical pressure in excellent agreement with experimental results.

2.2 SOME RELATED INDUSTRIAL OBSERVATIONS

Chedaille et al (14) observed violent expansion and splashing of vacuum-cast steel which led to ingot defects, as a result of which stream limiters made of refractory-lined cylinders were subsequently employed. They attributed the splashing to choking of the two-phase flow at the end of a convergent nozzle and that the gas bubbles at

a relatively high pressure at the nozzle exit expanded rapidly on flowing through the chamber.

Inclusions were found in the ingot as a result of refractory particles falling from the lining. To overcome the problems convergent-divergent nozzles were successfully designed and employed (the design was based on the theory of two-phase flow (14) (15))to obtain a gradual pressure decrease within the divergent section of the nozzle and hence less vigorous splashing of metal stream.

Meadowcroft and Milbourne (16) injected argon into a stream of molten steel through porous nozzle walls in order to break away the deoxidation products which were blocking the nozzle during pouring into a continuous casting mould. They found a critical argon flow rate, for a given nozzle, above which splashing occurred and below which blocking of the nozzle by the deoxidation products occurred. The critical argon flow rate would correspond to when the static pressure of the stream at the nozzle exit reaches the ambient pressure. Above the critical flow rate the stream is choked and the static pressure of the stream exceeds atmospheric pressure causing stream splashing at the nozzle exit.

Hornak and Orehoski (17) have also reported the two-phase and splashing characteristics of molten steel in an

industrial plant.

Turton (18) and Knaggs(19) have demonstrated the features, industrial operation and problems associated with typical stream degassing plants within the British Steel Corporation. A summary of the common refractory materials used in vacuum stream degassing plant is shown in table 2.2.

In industrial practice the duration of steel stream fall is normally about one second to minimise heat losses by radiation. Sharp (20a) took high speed cine photographs of a stream degassing process of an industrial plant and observed droplet formation from collapsing gas bubbles within the stream.

The importance of drop size on degree of degassification has been theoretically demonstrated by Richardson and Bradshaw (20b) who calculated the fraction of solutes removed as a function of droplet radius and fall duration as shown in table 2.3.

In a similar exercise Hokansen (21) plotted graphs of total oxygen removed as a function of time and tank pressure. These are shown in fig. 2.1.

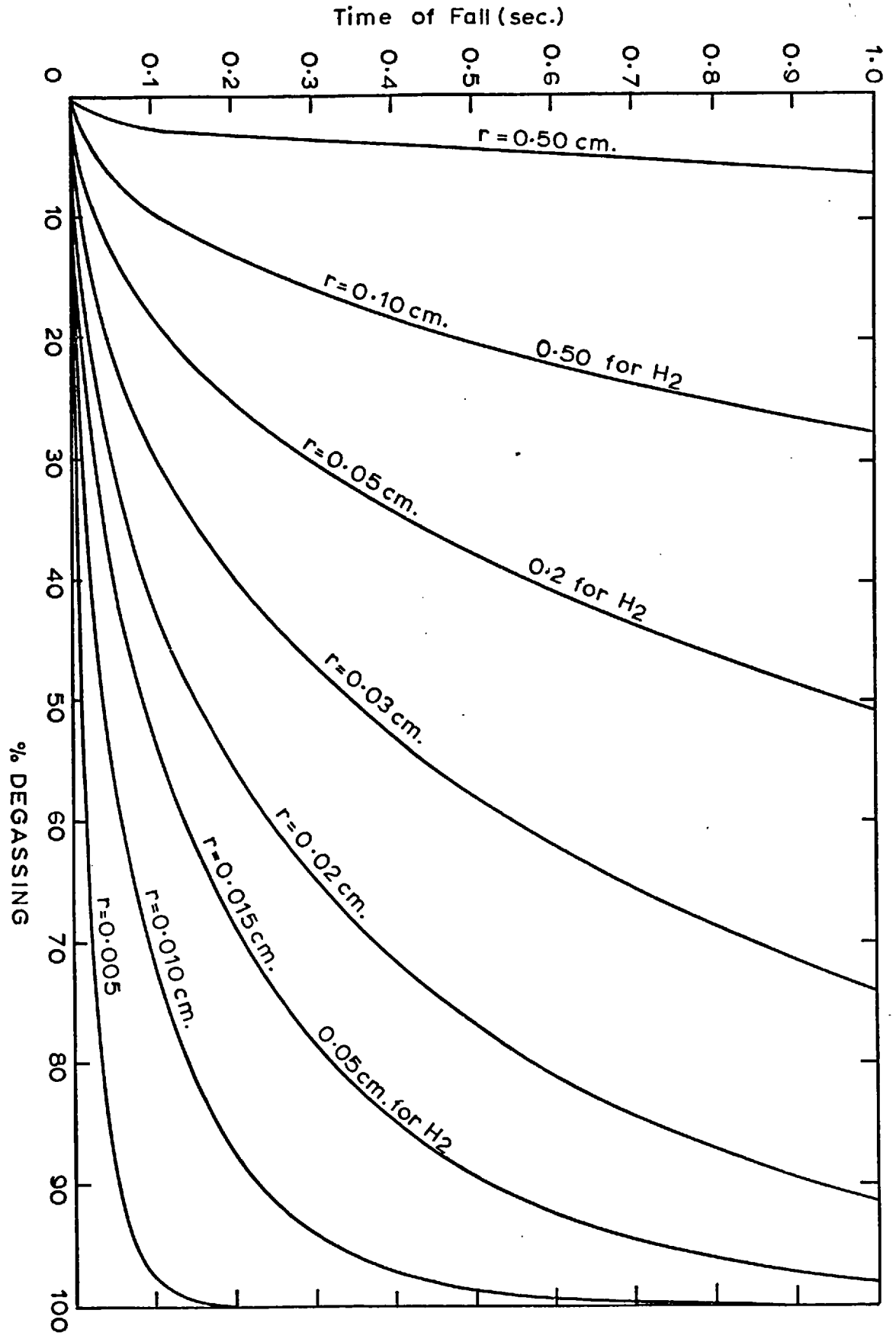

FIG.2.1 PERCENTAGE DEGASSING (OXYGEN REMOVAL) AGAINST DROPLET SIZE & TIME OF FALL FOR A DIFFUSION CONTROLLED PROCESS (21)

SUMMARY OF REFRACTORY USAGE IN INDUSTRIAL VACUUM STREAM DEGASSING PLANTS. (18)(19)(20)

Type of process	Maximum steel temp °C	Furnace ladle (service conditions)	REFRACTORIES USED				Service conditions	Receiver
			Ladle lining	Stopper rod	Nozzle	Stream limiter		
ladle to ladle	1700	high superheat, slag cover	standard fireclay bricks but life improved with 80% alumina brick	fireclay, but diameter may be increased for improved life	unfired magnesite	unfired magnesite	turbulence of metal	standard fireclay bricks
ladle to mould	1640	some superheat, slag cover, pronounced wash line when topping up for large ingots	bottom 80% alumina bricks; upper wall standard fireclay bricks	fireclay, but carbon coated fireclay when topping up is required	fired magnesite	fired magnesite	spreading stream	dense 42% alumina bricks used in mould heads

Table 2.2

Gas	Drop radius (mm)	Time of fall (secs)			
		½	1	½	1
		M/M_∞ *	M/M_∞	M/M_t **	M/M_t
H	1	0.70	0.85	0.66	0.80
	3	0.28	0.39	0.26	0.37
N	1	0.19	0.26	0.17	0.23
	3	0.06	0.09	0.05	0.08
O	1	0.19	0.26	0.19	0.26
	3	0.06	0.09	0.06	0.09

TABLE 2.3

INFLUENCE OF TIME OF FALL AND DROP RADIUS ON LOSS OF H_2, N_2 AND O_2 BY UNSTEADY STATE DIFFUSION.

* M/M_∞ is the fraction of gas removed in the given time to that which would be removed in infinite time.

** M/M_t is the fraction of total solute removed from a steel containing originally:
5×10^{-4} wt -% H, 4×10^{-3} wt-% N, 0.015 %C and 0.10%C.

C H A P T E R 3

THEORETICAL BACKGROUND.

3.1 THERMODYNAMIC CONSIDERATIONS.

3.1.1 Solubility of nitrogen and hydrogen in pure molten iron

3.1.2 Dissolution of carbon and oxygen in pure molten iron.

3.1.3 Effect of alloying elements on the solubility of gases in molten iron.

3.2 KINETIC CONSIDERATIONS.

3.2.1 Various possible kinetic controlling steps.

3.2.2 Mass transfer theories applicable to stirred melts.

3.2.3 Gas saturation of iron melt.

3.3. BUBBLE NUCLEATION

3.4. BUBBLE GROWTH.

3.5.1 Jets and drop formation

3.5.2 Rayleigh break-up.

CHAPTER 3. THEORETICAL BACKGROUND.

3.1. THERMODYNAMIC CONSIDERATIONS.

3.1.1. Solubility of nitrogen and hydrogen in pure molten iron.

The solubility of a diatomic gas in liquid metals is directly proportional to the square root of its partial pressure above the melt. Gaseous nitrogen and hydrogen exist as diatomic molecules and dissociate to form dilute solutions with liquid iron at steelmaking temperatures. The general equilibrium representation of hydrogen and nitrogen is of the form:

$$(\tfrac{1}{2})\ X_2 = [X] \quad \ldots\ldots\ldots \quad 3.1$$

$$K_X = h_X / P_{X_2}^{1/2} \quad \ldots\ldots\ldots \quad 3.2$$

These solutions obey Henry's law and hence equ. 3.2 may be written as

$$[\text{wt-\%X}] = K_X\ P_{X_2}^{\frac{1}{2}} \quad \ldots\ldots\ldots \quad 3.3$$

At 1600°C

$$K_N = 4.5 \times 10^{-2}\ \text{wt-\%} / \text{atm}^{\frac{1}{2}} \quad \ldots\ldots\ldots \quad 3.4$$

$$K_H = 2.7 \times 10^{-3}\ \text{wt-\%} / \text{atm}^{\frac{1}{2}} \quad \ldots\ldots\ldots \quad 3.5$$

These values were obtained from references (22) and (22a).

In liquid iron the temperature dependence of K_X and hence the solubility of nitrogen (22) and hydrogen (22a) at 1 atmosphere partial pressure is given by:

$$\log_{10} K_H\ \text{wt - \% / atm}^{\frac{1}{2}} = (-1670/T - 1.68) \quad \ldots\ldots \quad 3.6$$

$$\log_{10} K_N\ \text{wt - \% / atm}^{\frac{1}{2}} = (-188.1/T - 1.246) \quad \ldots\ldots \quad 3.7$$

The temperature dependence of solubility is small, for example between 1535 and 1700°C the solubility of hydrogen in pure iron at 1 atmosphere increases from 0.0025 to 0.0030 wt-%.

3.1.2 Dissolution of carbon and oxygen in pure, molten iron.

The equilibrium pressure of oxygen in oxygen-saturated liquid iron ranges between 10^{-6} and 10^{-4} mm Hg. between 1535°C and 1650°C. This is too low for direct measurement, hence oxygen solubility in iron is experimentally varied and investigated using controlled mixtures of either CO - CO_2 or H_2 - H_2O.

It has been shown conclusively (23) that carbon and oxygen are each dissolved atomically and that the carbon-oxygen reaction occurs by the reaction:

$\underline{C} + \underline{O} = CO$ at the gas/liquid interface.

For the reactions between carbon and oxygen dissolved in liquid iron at sufficiently low concentrations of both species Henrian activities of carbon and oxygen are considered:

$$\underline{C} + \underline{O} = CO \quad \ldots\ldots\ldots\ldots \quad 3.8$$

$$CO + \underline{O} = CO_2 \quad \ldots\ldots\ldots\ldots \quad 3.9$$

$$CO_2 + \underline{C} = 2CO \quad \ldots\ldots\ldots\ldots \quad 3.10$$

the addition of equ. 3.9 and 3.10 yields equ. 3.8.

$$K(3.9) = P_{CO_2}/P_{CO}.h_O \quad \ldots\ldots \quad 3.11$$

$$\Delta G^\circ \text{ (3.9) cals/mole} = -38{,}050 + 20.72T \quad \ldots\ldots \quad 3.12$$

$$K(3.10) = P^2_{CO}/P_{CO_2}.h_C \quad \ldots\ldots \quad 3.13$$

$\Delta G°(3.10)$ cals/mole = 34,500 - 31.07T 3.14

$K(3.8) = P_{CO}/h_O h_C$

$= K(3.9)\ K(3.10)$ 3.15

At 1600°C

$K(3.9)$ $(wt\text{-}\%)^{-1} = 0.8126$ 3.16

$K(3.10)$ atm/wt-% = 580.546 ..... 3.17

Hence

$K(3.8)$ atm/$(wt\text{-}\%)^2$ = 471.75 ..... 3.18

h_O (wt-%) = $P_{CO_2}/P_{CO}.K(3.9)$ 3.19

h_C (wt-%) = $P^2_{CO}/P_{CO_2}.K(3.10)$ 3.20

Values of h_O and h_C for some CO - CO_2 mixtures are shown in table 3.1. The equilibrium constant [wt-%C x wt-%O]/P_{CO} atm, has the value of 0.002 at 1600°C when the carbon concentration is less than 0.20 wt-% (24).

3.13. The effect of alloying elements on the activity coefficient of gases in iron.

Alloying elements affect the activity coefficient of gases in iron. Values of interaction coefficient, e^y_x in liquid Fe - x - y alloys are available in standard texts (22b) (22c). The interaction coefficient $e^y_x = \partial(\log_{10} f_x)/\partial(wt\text{-}\%y)$, and gives the variation of activity coefficient of x with respect to additions of y.

Vol - %		h_O	h_C	h_C/h_O	$(h_C/h_O)(D_C/D_O)^{\frac{1}{2}}$
CO	CO_2	(wt. %)	(wt. %)	–	–
99	1.0	0.0124	0.169	13.582	38.233
98	2.0	0.025	0.083	3.294	9.273
96	4.0	0.051	0.040	0.774	2.179
94	6.0	0.079	0.025	0.323	0.909
92	8.0	0.107	0.018	0.168	0.473
90	10.0	0.137	0.014	0.102	0.287
85	15.0	0.217	0.008	0.038	0.107

Table 3.1

HENRIAN ACTIVITIES OF SOME CO - CO_2 MIXTURES IN MOLTEN IRON AT 1600°C.

These can be used to predict the solubility of gases in more complex alloys under any partial pressure.

If both simple and complex alloys are under the same partial pressure of gas, the activities will be the same and as they obey Henry's law, these can be represented as shown below:

h_x = [wt-%x] in pure iron 3.21

h_x = [wt-%x] f_x in iron alloy 3.22

where $f_x = f_x^x . f^y_x \ldots f^i_x$ 3.23

for an Fe - x - y ..... solution.

For example, for iron with a typical analysis given below (the type used in the current investigation)

Impurities:	C	Si	Mn	P	S	Cr	Ni	Cu
wt-% :	.03	.01	.12	.005	.01	.005	.005	.01

$f_N = 1.05$, $f_H = 1.005$

and so the influence of the alloying elements on activity is negligible.

3.2 KINETIC CONSIDERATIONS.

3.2.0 Various Possible Kinetic controlling steps.

The transition of a dissolved gas from a liquid metal to the gas phase comprises a number of consecutive steps, the slowest of which determines the overall process rate. (Fig.3.1 shows a schematic representation of typical modes of rate controlling steps in a gas desorption process.)

These steps include:

(i) convective transport of atoms from the bulk towards a zone near the surface.

(ii) transport from the zone by diffusion and convection to the surface.

(iii) transition of the gas atoms from the dissolved to the adsorbed state at the interface.

(iv) chemical reaction of gas atoms in the adsorbed layer.

(v) desorption of gas molecules from the surface.

(vi) diffusion of gas molecules into the surrounding space.

In the stream degassing process another important step may be the

(vii) removal of bulk gas from the chamber by the pumping system.

For gas bubble-liquid metal reactions the controlling mechanism may be any, or a combination of:

(i) gas diffusion within the bubble as in the decarburisation of steel with oxygen or carbon dioxide.

(ii) saturation of the bubble with the reaction products as in steel dehydrogenation by argon purging.

(iii) mass transfer through the liquid boundary layer at

the gas-metal interface, for example, carbon deoxidation by argon purging.

(iv) chemical reaction at the gas-metal interface as in the nitrogenation of steel at high oxygen activities.

Several examples are available showing where each of these steps may be rate determining:

Decarburisation of liquid iron at 1700°C at very low carbon concentrations is believed to be chemically controlled.(25)

Richardson and Bradshaw have suggested that when reaction at a gas-metal interface involves a change in atomicity as in the evolution of H_2, N_2 and CO the chemical step may be rate determining at low solute concentrations (20b).

It is currently believed that the transfer of oxygen gas from large rising bubbles into molten silver at 900°C is liquid transport controlled (20b) and that transfer of carbon (1-4%) out of an inductively stirred drop of liquid iron into CO_2 by the reaction

$$[C] + [CO_2] = 2CO \qquad \text{.....3.25}$$

is controlled by transport in the gas phase (26).

Where two reacting species are involved, as for carbon deoxidation, the transport of the species in smaller concentration becomes rate controlling. Gas

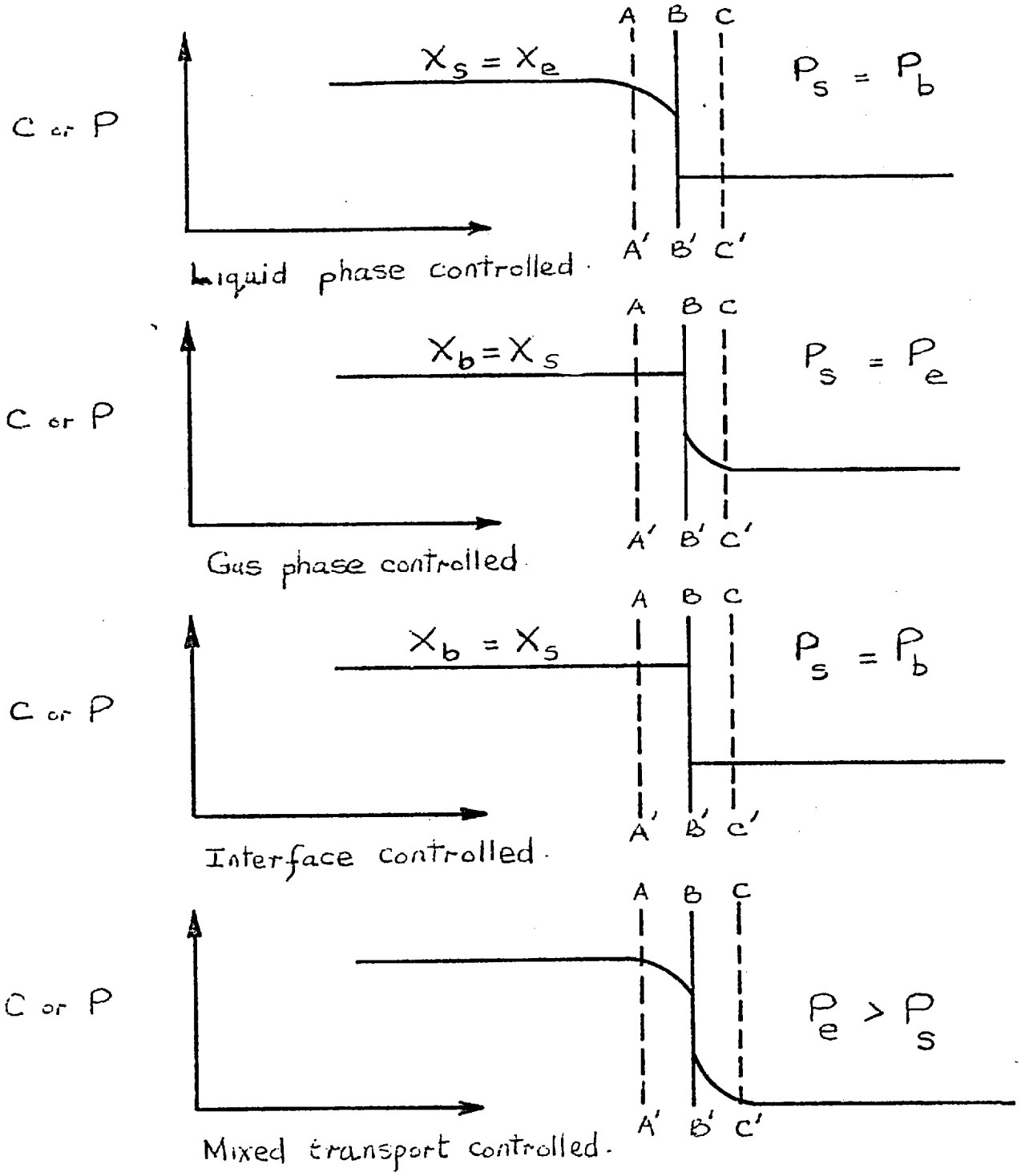

Fig. 3.1

SCHEMATIC REPRESENTATION OF VARIOUS MODES OF RATE CONTROL STEPS IN GAS DESORPTION.

phase transport is not likely to be slow under conditions of low pressure, high temperatures, large temperature gradients and continuous removal of gas - all featuring in vacuum degassing processes.

3.2.1. Theories of convective mass transfer at a gas-metal interface of a stirred melt.

The hydrodynamic theories discussed in the following section consider flow characteristics adjacent to interfaces and assume that the bulk of the liquid phase is well stirred either mechanically, electromagnetically or by natural convection. Each then predicts the mass transfer coefficient, k_L, as a means of estimating the rate of approach to equilibrium conditions. The mass transfer coefficient relates the flux density to the driving force. In the normal case the mass transfer coefficient remains constant during the mass transfer process.

All the flux equations for the evolution of gaseous species from the surface of a stirred melt controlled in the liquid phase are of the form:

$$dn/dt = k_L A (C_b - C_e) \quad \ldots\ldots\ldots\ldots \quad 3.26$$

where k_L varies according to the model applied. Many models have been developed, each with specific areas of validity.

(i) Film Theory.

The main feature of the film theory is that convective stirring keeps the bulk concentration of the melt uniform except at a thin static boundary layer of thickness δ in which the concentration decreases linearly from C_b to C_s.

The main disadvantage of the model is the difficulty associated with estimating the values of δ. King (27) suggested that δ is a function of diffusion coefficient and the degree of convective stirring, being larger for larger values of D and smaller for high flow velocity of convective currents past the boundary. Riddiford (28) also suggested that D/δ has an exponential dependence on temperature. Based on the film theory the mass transfer coefficient, k_L is given by:

$$k_L = D/\delta \qquad \ldots\ldots\ldots\ldots \quad 3.27$$

(ii) Danckwert's Surface Renewal Model (29)

The model rejects the presence of a thin static boundary layer in favour of a non-restrictive, total turbulence. It is assumed that the gas-liquid interface contains small liquid elements, which are continuously brought up to the surface from the bulk liquid by eddies. Mass transfer out of the eddies occurs by unsteady molecular diffusion; when it arrives at the surface, each fluid element is considered to have a concentration equal to that within the bulk system. The life time at the surface for a liquid element is given by:

$$t = d/v \qquad \ldots\ldots\ldots\ldots \quad 3.28$$

where d is the length of the contacting surface and v is the velocity of the fluid element going to the surface. A parameter, S, the fractional rate of random surface renewal is introduced and the mass transfer coefficient is given by

$$k_L = (DS)^{\frac{1}{2}} \qquad \ldots\ldots\ldots\ldots \quad 3.29$$

and 1/S is a measure of the average life time of surface elements.

For stirred cells k_L values lie in the range 10^{-1} and 10^{-4} cm/sec. depending on stirring conditions and the presence of surface active agents at the interface (30).

Gas $(C_S) = C_e$

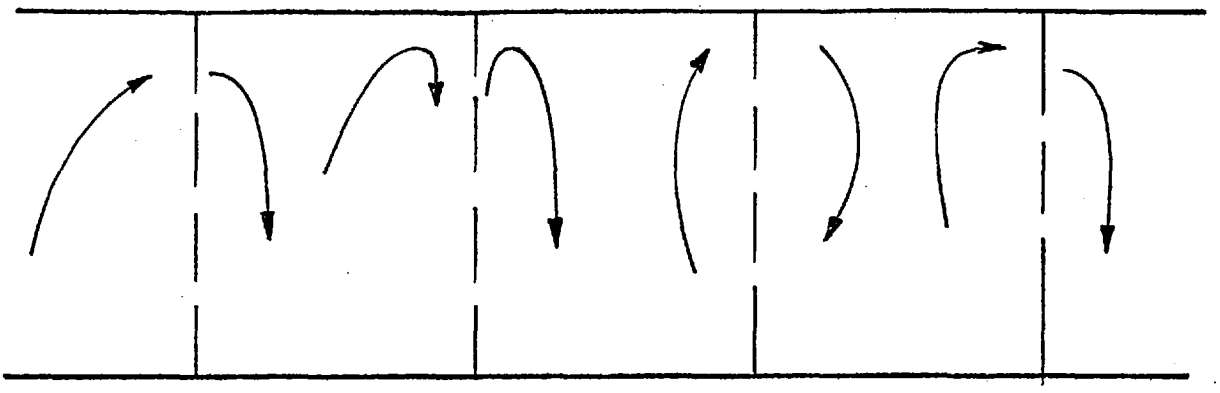

Melt $(C) = C_b$

SCHEMATIC REPRESENTATION OF DANCKWERT'S SURFACE RENEWAL MODEL.

Fig. 3.2.

(iii) Kraus Natural Convection Model (21a)

The Kraus model also rejects the static boundary layer and proposes a situation where natural convection currents, caused by density differential as a result of radiation heat losses from gas-metal interface, accomplish surface replenishment with fluid "pockets" from the bulk. The pocket then travels a distance (λ) with a velocity (v) parallel to the surface discharging its contents by unsteady state diffusion. Essentially the model assumes that convection arises only from density differences and that flow at the surface is friction free. The mass transfer coefficient is given by:

$$k_L = (Dv/\lambda)^{\frac{1}{2}} \quad \ldots\ldots\ldots 3.30$$

Kraus derived an expression relating v and λ to fundamental quantities:

$$\lambda/v = (\bar{\nu}\rho C_p/gXq)^{\frac{1}{2}} \quad \ldots\ldots\ldots \quad 3.30a$$

where ρ, C_p, X, $\bar{\nu}$ are the density, specific heat, coefficient of thermal expansion and kinematic viscosity respectively of the melt; g and q are the acceleration due to gravity and upward heat flow density at the free surface respectively.

Typical values of k_L for diffusing species in molten iron for a friction-free surface are of the order of 0.025 cm/sec, and could be as low as 0.004 cm/sec for one with a contaminated surface (20c). The slowing-down in the latter case may be attributed to the formation of a diffusion barrier at the melt surface resulting in an increase in surface equilibrium concentration. This effect has been detected as a hindrance to the mass transport of nitrogen in liquid iron (21b) (21c).

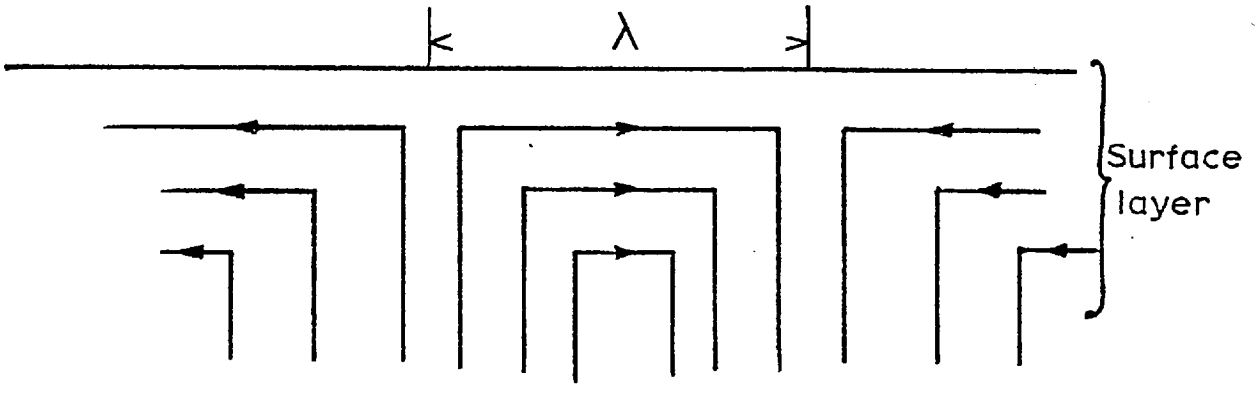

SCHEMATIC REPRESENTATION OF CONCEPT OF LIFE TIME.

Fig. 3.3.

(iv) Machlin Rigid Flow Model.

The model is applicable only to induction-stirred, cylindrical melts or those with similar forced convection flow. Interaction between eddy currents induced in the melt and the medium frequency field of an induction coil produces flow lines with negligible flow velocity gradient normal to the surface and in a direction radially outwards from the centre. Thus an element appears in the centre, discharges its contents by diffusion as it flows across the surface, and is then mixed into the bulk at the wall. The thickness of the diffusion boundary layer is assumed to be materially thinner than the depth of flow. The model predicts

$$k_L = 2(2Dv/\pi r_c)^{\frac{1}{2}} \quad \ldots\ldots\ldots 3.31$$

where v is the flow velocity at the crucible wall, D, the diffusion coefficient, r_c, the crucible radius, D and v are the only unknown variables.

A common feature of the Danckwerts, Kraus and Machlin models is the rejection of a thin static boundary layer and a concept of life time - the average time spent by a fluid element at the surface of the liquid. They assume a surface layer within which flow velocity is constant with depth and parallel to the surface. The

Kraus convection model allows a more accurate estimation of mass transfer coefficient on the basis of the system parameters and is valid for a melt stirred by natural convection currents caused by heat losses from the surface.

The validity of the different models for a particular process can be tested by measuring the dependence of the rate on diffusivity. For example in stirred liquids k_L is frequently proportional to $D^{\frac{1}{2}}$ which supports the surface renewal type models.

3.2.2 Gas Saturation of Iron Melt.

Assuming that the rate of nitrogen pick-up for iron is controlled by mass transfer in the liquid phase boundary layer an overall mass balance gives

$$k_L A(C_s - C_b) = V dC_b/dt \quad \ldots\ldots 3.32$$

$$\text{thus } dC_b/(C_s - C_b) = (k_L A/V)dt \quad \ldots\ldots 3.33$$

integrating equ. 3.33

$$-\ln(C_s - C_b) = k_L At/V + \text{constant} \quad .. 3.34$$

when $t = 0$, $C_b = 0$, the constant in equ. 3.34 becomes $-\ln C_s$

$$\text{therefore } -\ln(1 - C_b/C_s) = k_L\, At/V \quad \ldots\ldots 3.35$$

$$\text{therefore } t = -[V/(k_L A)][\ln(1-C_b/C_s)] \quad \ldots\ldots 3.36$$

$$= -[2.303V/(k_L A)][\log(1-C_b/C_s)] \quad \ldots\ldots 3.37$$

where t is the time required to attain C_b/C_s degree of equilibrium saturation.

A graph of $\log(1 - C_b/C_s)$ against time, t would give a slope given by

$$- k_L A/2.303V \qquad \ldots\ldots 3.38$$

The only unknown factors in equ. 3.38 for gas bubbles-agitated liquid would be the effective area, A.

Once the right hand side of equ. 3.38 is known, say for the nitrogenation of molten iron, standardising the bubbling procedure, mass of charge, crucible dimensions, and melt temperature, it should be possible to estimate the times required to attain various levels of equilibrium saturation for the dissolution of other gases in molten iron if their diffusivities are known since, essentially,

$$k_{L_{(1)}}/k_{L_{(2)}} = (D_1/D_2)^{\frac{1}{2}} \qquad \ldots\ldots\ldots 3.38a$$

3.3(a). HOMOGENEOUS NUCLEATION.

It has been shown by many workers (2), (5), (6) and (7), that bubbles are nucleated in the nozzle and that gas-liquid two-phase flow emerges from the nozzle when a gas-saturated liquid is discharged under certain conditions.

For a bubble in a solution of its own gas to be stable

$$P_b = P_a + \rho_L gh + 2\sigma/r^* = P_b^* \quad \ldots\ldots\ldots 3.39$$

for $r > r^*$, $P_b < P_b^*$

and the dissolved gaseous species will diffuse into the bubble and it will grow.

The embryo bubbles for which $r < r^*$ are all unstable and exist only by virtue of local fluctuations in free energy throughout the liquid. The main problem is to calculate the number of bubbles of critical size present in the liquid and the rate at which they become stable under specified conditions.

The equation given below has been developed for the rate of spontaneous production of bubbles of dissolved gas above the critical size in a supersaturated liquid.

$$J = \mathcal{Z}\beta^* A^* N \exp.(-\Delta F^*/KT) \quad \ldots\ldots 3.40$$

where J = number of bubbles formed per unit volume per sec.

$\mathcal{Z}$ = non-equilibrium factor

β^* = rate of gain of a molecule by the bubble of critical size

A^* = area of bubble of critical size

N = total number of atoms per unit volume

For nucleation to occur significantly J must be greater than 1 bubble $cm^{-3} sec^{-1}$.

Bradshaw (31) applied equ. 3.40 to hydrogen bubble

formation in molten steel and calculated that the degree of supersaturation required for a substantial rate of nucleation was of the order of 10^4 atmospheres. He also considered the homogeneous nucleation of hydrogen, nitrogen and also CO gas in molten steel exposed to vacuum and concluded that homogeneous nucleation was very improbable. Since the contact angle of molten steel in real systems was of the order of 100 — 150° , Bradshaw concluded that even the presence of a flat substrate would only allow comparatively minor reductions in the degree of supersaturation required for homogeneous nucleation.

However, other workers have shown that apparently homogeneous nucleation of gas bubbles can occur in levitated iron droplets with gas supersaturation of the order of 10 atm. (25)(32) It would appear therefore, that nucleation of gas bubbles under industrial steelmaking conditions is possible, and that the basis of the derivation of equ. 3.40 is not valid. Typical oxygen and nitrogen contents of industrial steels are shown in table 3.2.

OXYGEN CONTENT		NITROGEN CONTENT	
Before	after	Before	after
degassing (10^{-3} wt%)		degassing (10^{-3} wt%)	
10.2	6.5	9.2	7.1
9.5	4.6	8.1	7.4
7.3	2.8	6.8	6.2
9.4	4.7	6.4	6.3
10.0	5.3	7.6	6.5
11.2	5.0	9.4	7.3
7.6	3.6	7.2	6.8

Table 3.2

OXYGEN AND NITROGEN CONTENTS OF TYPICAL INDUSTRIAL STEELS BEFORE AND AFTER DEGASSING (33)

The carbon-oxygen level at which boiling ceases has been investigated in a ladle degassing unit by Kraus (21a) who obtained for the minimum carbon and oxygen levels capable of supporting a bubble:

$$K(3.9)h_C h_O = P_{CO} \geq P_a + \rho_L g h + 2\sigma/r \quad \ldots\ldots \quad 3.41$$

Bennett (34) has observed the cessation of CO boil at [C] = 0.2, [O] = 8 x 10^{-4} wt-%.

3.3(b). HETEROGENEOUS NUCLEATION.

For nucleation to occur readily at a solid boundary, the adhesion between the liquid and solid must be a minimum. This implies large values of contact angle, θ .

Bradshaw considered the effect of small cavities on solid surfaces and suggested that a cavity of 10^{-3} cm. radius would serve as a nucleation site in the molten steel system at a moderate degree of supersaturation of the order of $\frac{1}{2}$ - 2 atm if the contact angles were less than 90°. With higher contact angles, lowering of the supersaturation required will occur and in addition will reduce the probability of the liquid filling the cavity completely. Furthermore the proposed nucleation mechanism would work endlessly if the bottom of the cavity was so sharp that a small gas embryo would always be left in the cavity, after releasing each bubble nucleus, to spark off the subsequent ones.

The sequence of nucleation in a right angle conical-shaped cavity based on the above postulate is shown in Figure 3.4.

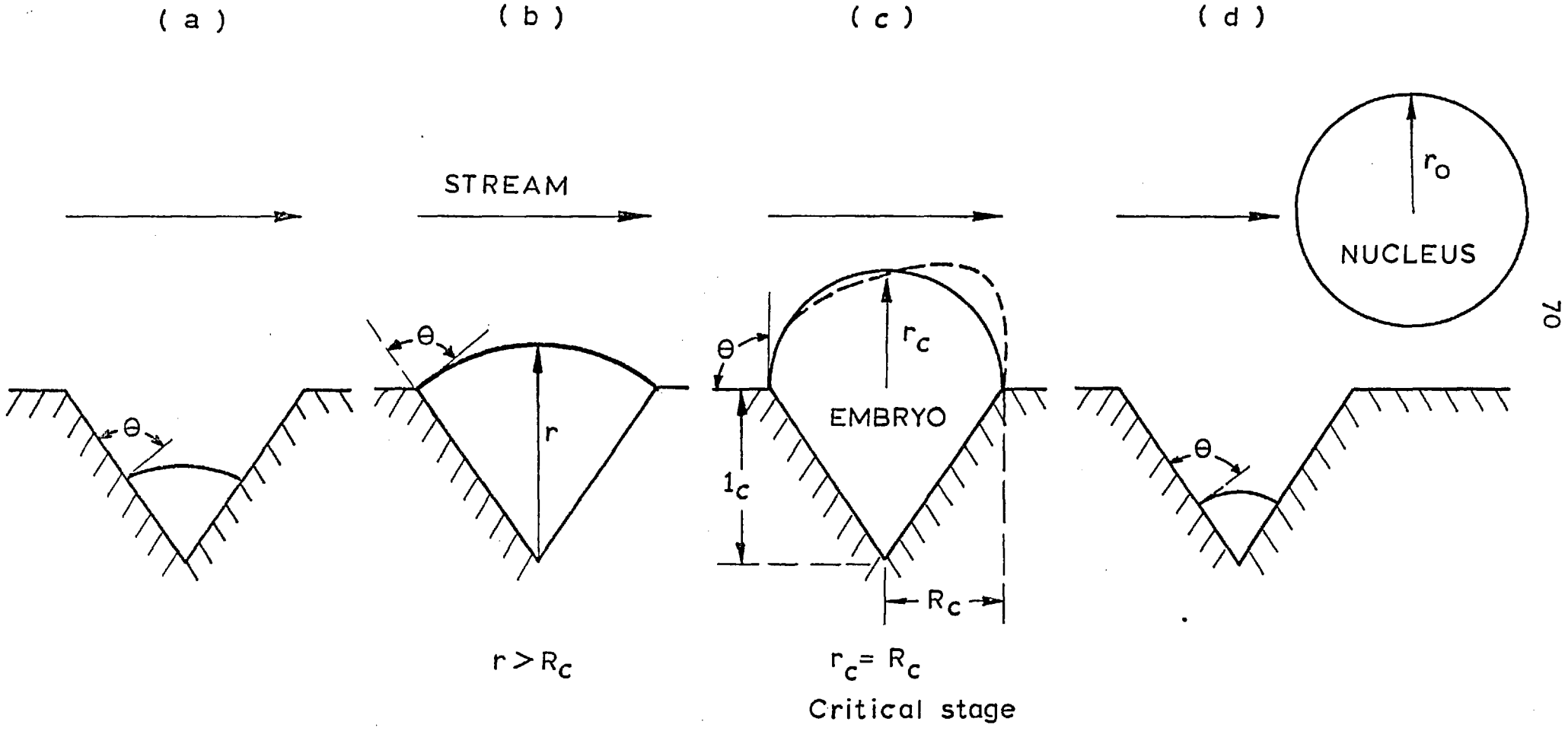

FIG. 3.4. SEQUENCE OF NUCLEATION ON A CAVITY ON NOZZLE WALL (contact angle θ=90°)

Delve and his coworkers (25a) attributed the filling of refractory pores with slag in a Dortmond-Hörder degassing unit to pronounced decrease in the observed degassing rate.

In an oxygen saturated silver melt flowing through a 'Nimonic 75' nozzle Mizoguchi et al (7) showed that stream break-up is also dependent on the level of oxygen in silver and have discussed the important factors limiting the rate of bubble growth. These include:

(i) Diffusion of solute elements in the liquid

(ii) Chemical kinetics at the phase boundary

(iii) Surface tension

(iv) Viscosity

(v) Solubility of gas in the liquid

(vi) The pressure of the chamber into which the stream is discharged.

Davies et al. (35) investigated the potential of refractory surfaces to facilitate carbon monoxide growth in relation to surface porosity. They suggested that significant surface porosity was a prerequisite and caused bubble nucleation provided the refractory material was unreactive to the melt, and the surface tension of the melt did not favour cavities being filled with molten metal. They suggested that pores with radii satisfying the rela-

tionship:

$$2\sigma/[P_{CO}-(P_a + \rho_L gh)] \leq r_{pore} \leq -2\sigma\cos\theta/(P_a + \rho_L gh) \quad \ldots\ldots 3.42$$

are theoretically suitable for bubble nucleation. The limits for bubble nucleation suggested by equ. 3.42 will only hold if the bubble does not spread before becoming hemispherical. Furthermore the situation in practice will be more complicated since cavities do not have simple and regular geometric configurations.

The composition of their refractories is shown in table 3.3.

The available pore sizes for boil initiation calculated from pressure drops and expression for minimum value of cavity radius to sustain growth:

$$r_{min} = 2\sigma/[P_{CO} - (P_a + \rho_L gh)] \quad \ldots\ldots 3.43$$

lie in the range 0.025 - 0.045 mm. They showed that this range is theoretically useful for contact angles $\sim$ 140°. The boil was observed to start from a calculated pore size of 0.04 mm with isolated bubbles from 0.08 mm diameter pores. This agreed with the measured pore sizes. They observed that the high silica content of group C materials rendered them highly chemically reactive and a slag was formed between silica, iron and dissolved oxygen. This was normally much more wet-

Group & No.	COMPOSITION OF REFRACTORIES wt-%				mean pressure drop to initiate a boil mmHg.	measured pore size mm.
	MgO	Cr_2O_3	Al_2O_3	SiO_2		
A1	68.7	11.8	10.4	1.9	424 ± 36	0.1 -0.01
A2	48.4	20.4	18.3	3.0	455 ± 34	0.1 -0.01 majority at 0.05
A3	94.7	-	0.05	1.65	446 ± 6	0.1 -0.01 majority at 0.05
B1	0.2	-	84.3	11.5	604 ± 42	$r \leq 0.03$; $r \sim 0.1$
B2	-	-	84.5	12.0	623 ± 25	0.06 -0.01
C1	0.2	-	61.0	32.1	700	High silica content rendered refractories reactive. Liquid slag formed.
C2	44.5	-	-	50.0	700	

PROPERTIES OF TYPICAL REFRACTORIES USED FOR THE INVESTIGATION OF THE SIGNIFICANCE OF PORE STRUCTURE ON BUBBLE GROWTH. (After Davies et al.) (35)

T A B L E 3.3.

ting than iron and thus filled the pores which would normally be available for bubble nucleation .

3.4. BUBBLE GROWTH.

Scriven (36) considered the mass transfer controlled growth of a single spherical bubble, neglecting the effects of liquid viscosity, inertia and surface tension. He arrived at the following solutions:

$$r = 2\beta(Dt)^{\frac{1}{2}} \quad \ldots\ldots\ldots\ldots\ldots\ldots \quad 3.44$$

$$\beta = f(\phi, E)$$

$$\phi = (\rho_L/\rho_g)[(C_b - C_{sat})/(1 - C_{sat})] \quad \ldots \quad 3.45$$

$$E = (1 - \rho_g/\rho_L) \quad \ldots\ldots\ldots\ldots\ldots\ldots \quad 3.46$$

He showed that in the case where $\rho_g \ll \rho_L$, β was equal to ϕ .

Gale (37) studied experimentally the growth of artificially-nucleated, isolated CO_2 and nitrogen bubbles in viscous dimethyl siloxane and classified their growth into three distinctive stages:

(i) a retarded slow growth stage attributable to surface tension, viscosity and inertial effects.

(ii) a second stage in accordance with Scriven parabolic growth theory.

(iii) a third stage with accelerated growth rate as the bubbles moved away from their point of formation.

Rosner and Epstein (38) theoretically analysed the

effect of surface tension and initial bubble size on the growth of isolated gas bubbles controlled by diffusion and/or chemical kinetics under the following assumptions:

(a) mean values for the physical properties of liquid

(b) negligible viscous and inertial effects

(c) reversible nth order ex-solution kinetics.

They derived relationships between dimensionless bubble radius (r/r_0) and dimensionless growth time (τ) for given dimensionless surface tension (ξ) for a

(i) diffusion controlled growth and

(ii) chemical kinetic controlled growth.

In the case of large supersaturation simplified solutions were obtained and these are given below:

(a) chemical kinetic controlled growth (second order).

$$\tau = r/r_0 - 1 + \xi.\ln(r/r_0) \quad \ldots\ldots\ldots \quad 3.46(a)$$

where $$\tau = (\rho_L/\rho_g)\ k\ C_b^2\ t/r_0 \quad \ldots\ldots\ldots \quad 3.46(b)$$

$$\xi = 2\sigma/P_L r_0 \quad \ldots\ldots\ldots \quad 3.49$$

(b) diffusion controlled growth

$$\tau = (r/r_0)^2 - 1 + \frac{10}{3}.\xi.(r/r_0-1) - 2(1+\xi)(1-r_0/r) + 4/3\ \xi^2.\ln(r/r_0) - 2/3\ \xi.(1+\xi)(1 - r_0^2/r^2) \quad \ldots\ldots\ldots \quad 3.46(c)$$

where $$\tau = 4D(\rho_L/\rho_g)^2\ B^2(t/r_0^2)(1+B) \quad \ldots\ldots \quad 3.47$$

$$-B = (C_V - C_b)/(1 - C_b) \quad \ldots\ldots\ldots \quad 3.48$$

$$\sum = 2\sigma/P_L r_0 \quad \ldots\ldots\ldots \quad 3.49$$

The resulting graphs (figure 3.5) illustrate the effect of surface tension on the initial bubble growth rate for diffusion controlled growth and show how the limiting case approached Scriven's parabolic growth law.

Fig. 3.5(a) illustrates the actual growth of a spherical bubble and the departure from the parabolic law at the beginning.

3.5.1 Jet and Drop Formation.

The variety of flows obtainable in chemical engineering processes may be demonstrated by the flow patterns in a vertical tube evaporator which consists of vapour, drops, annular, slug, bubbly, liquid flows and their combinations. In certain cases flow regime changes are attributed to instabilities arising from wave amplification which may propagate continuous or discontinuous changes.

A bubbly flow pattern is characterised by a suspension of discrete bubbles in a continuous

(a) Kinetically controlled growth (eqt. 3.46 a)

(b) Diffusion controlled growth (eqt. 3.46 c)

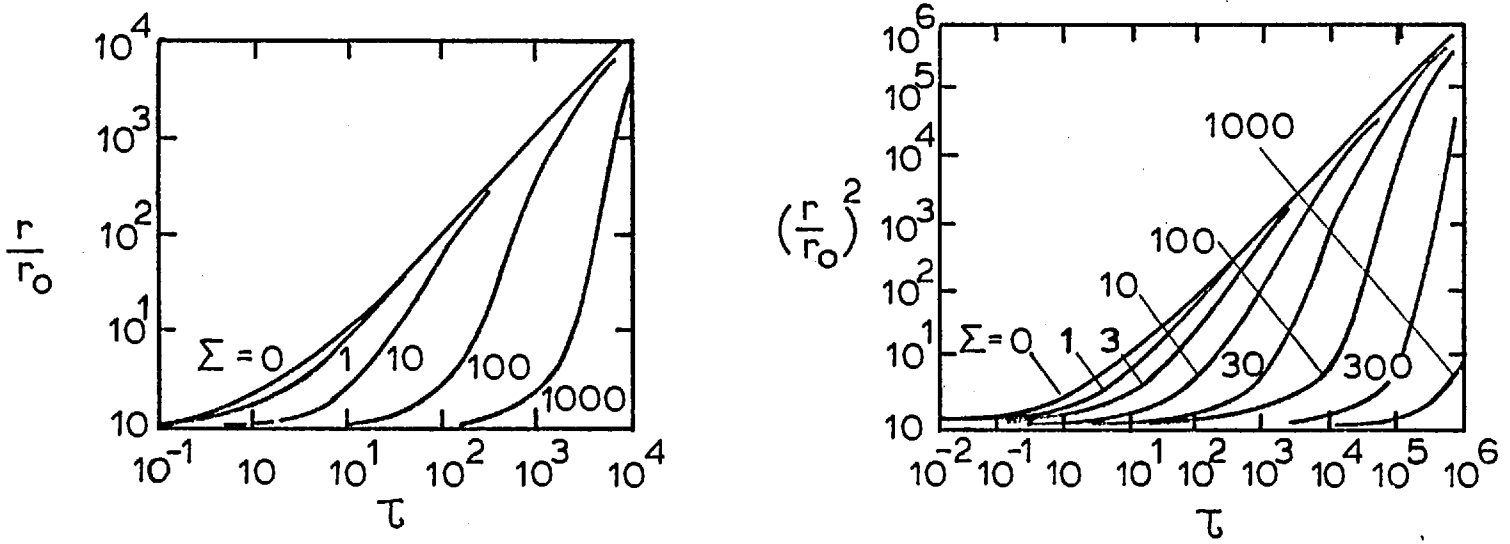

FIG.3.5 SURFACE TENSION EFFECT ON BUBBLE GROWTH (38)

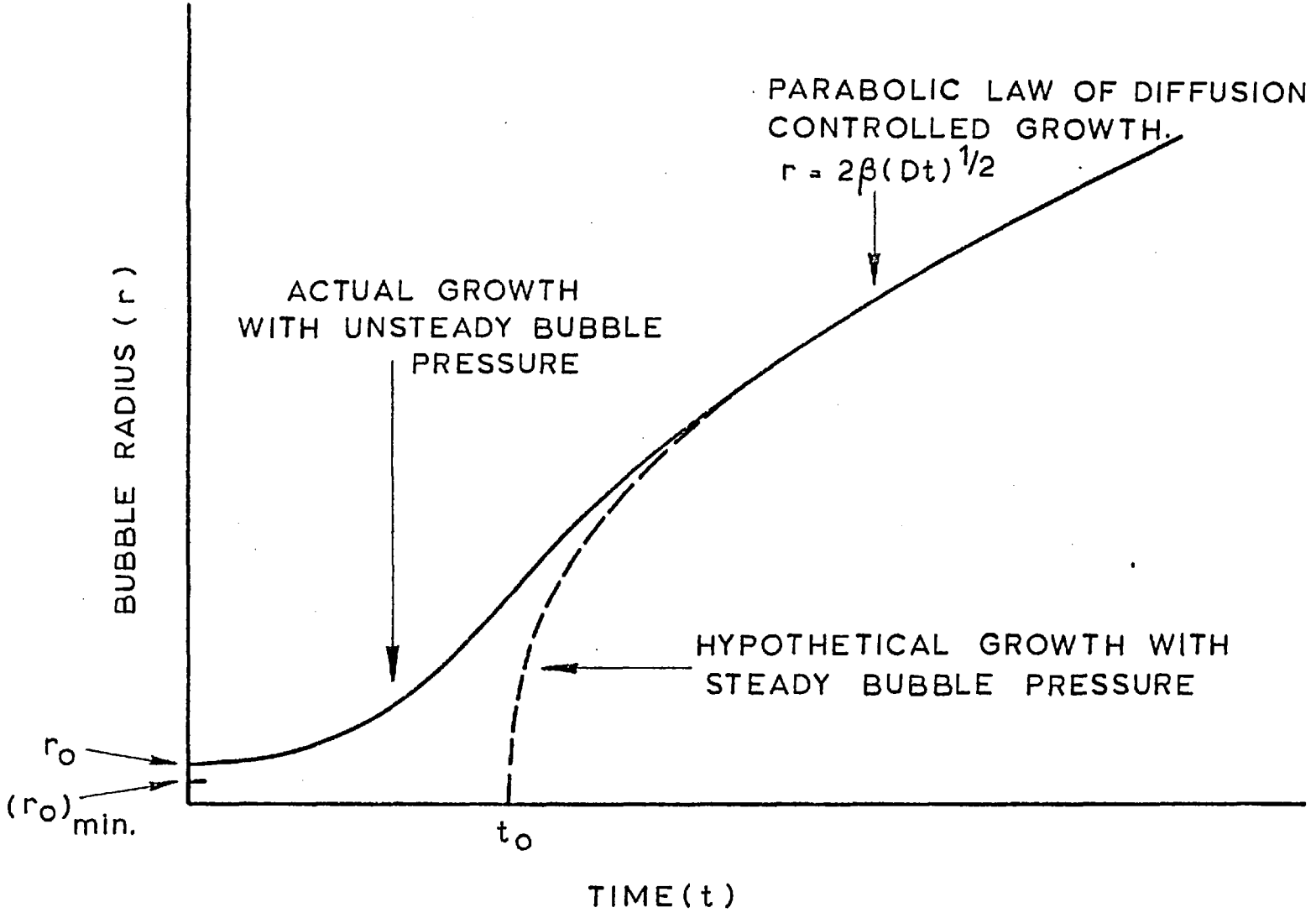

FIG. 3.5(a) BUBBLE GROWTH, EARLY RETARDATION (37)

liquid; the regime may vary from an isolated bubble to quasi-continuum flow of a foam; invariably interaction between surface tension, viscosity, inertia and buoyancy have pronounced effects on bubble shapes and trajectories.

3.5.2. Rayleigh Jet Break-up

The visual changes that occur as the flow rate of a single phase liquid through a nozzle is increased havebeen investigated (39). At low flow rates, drops form individually at the nozzle tip and grow in size until the buoyancy force overcomes surface tension and the drop is released. At increased flow rate a point in reached - jetting point - where a very short continuous liquid neck exits between the nozzle tip and point of drop detachment. Further increase in flow rates rapidly lengthens the jet which appears as a smooth column of liquid with occasional transient lumps called RAYLEIGH JET which finally appears ruffled at its outer end with less uniformity than at the earlier stage; this occurs at or near the maximum length of jet corresponding to the critical liquid flow rate above

which the jet length decreases again until jet break-up retreats again to the nozzle tip and atomisation occurs.

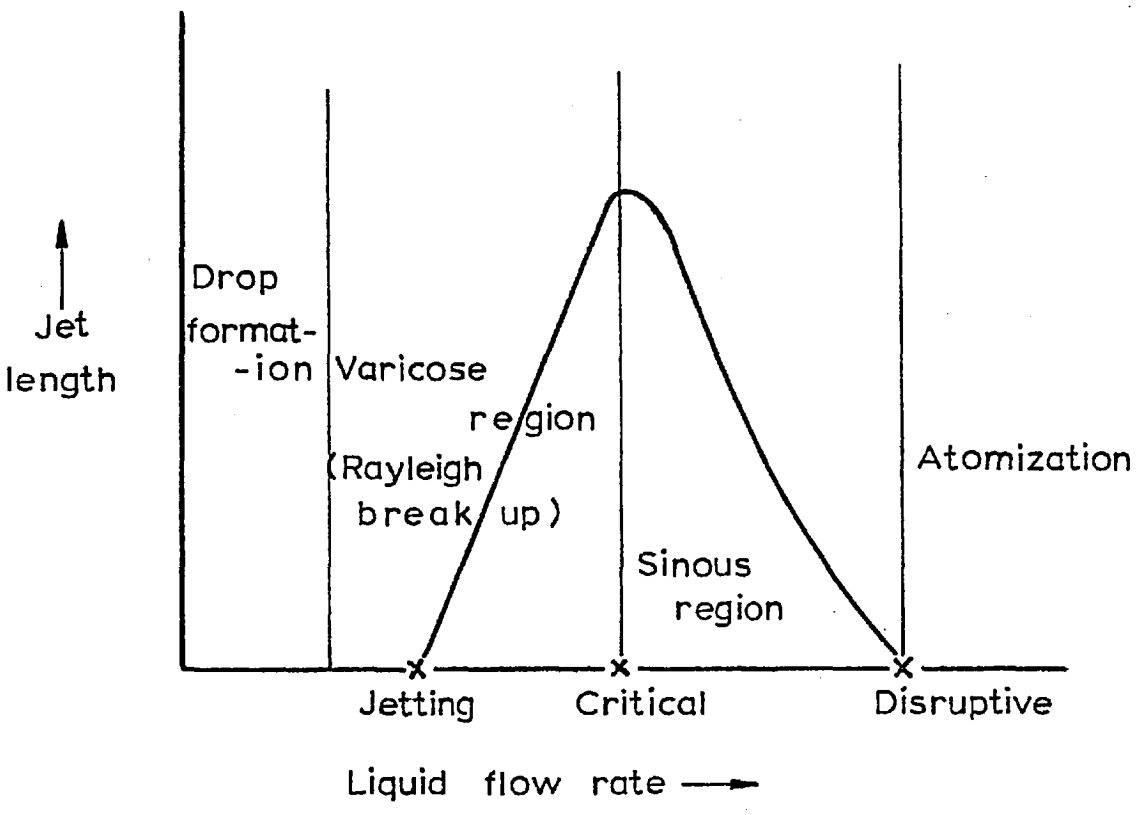

FIG. 3.6.

FLOW REGIMES OF JETS (After Richardson and Merrington)(40)

Rayleigh (41), (42) and (43) considered the collapse of a non-viscous, irrotational liquid jet and showed that a small axisymmetric disturbance of amplitude equal to one half diameter of the undisturbed liquid jet would cause a break-up. The above description will be appropriate for the situation where stream break-up occurs in the absence of bubble nucleation and growth.

C H A P T E R 4.

EXPERIMENTAL METHOD.

4.5 MAJOR EXPERIMENTAL PROBLEMS

4.5.1 Introduction

4.5.2 Preferential attack of alumina at solid-liquid metal-gas interface

4.5.3 Reduction of alumina by graphite susceptor

4.5.4 Chemical attack of alumina

4.5.5 Spalling of alumina.

CHAPTER 4.

EXPERIMENTAL METHOD.

4.1 DESIGN OF APPARATUS

The earlier stage of the programme was devoted to formulation of a design and proposals for preliminary experiments to assess the suitability and limitations of the components of the final apparatus.

The optimum requirements of the final system included:

1. A crucible with adequate refractoriness, high temperature strength and chemical inertness to molten iron at 1600°C both under reducing and oxidising conditions.

2. Since the crucible would have to be movable so that it could be held inside a high frequency coil for melting, and swiftly lowered below the coil to photograph the stream from the nozzle exit, good resistance to thermal shock was essential. A lever- or push button-operated pneumatic system, with adequate flow regulators was also required for precise and quick positioning of the crucible.

3. The stream behaviour was presumed to be dependent on the geometry and surface properties of the nozzle. For meaningful comparisons to be made between different

runs the consistency of the properties of nozzle materials would have to be guaranteed.

4. In the event of a forced choice of material with poor resistance to thermal shock - in which case a campaign would last several hours - flexibility was required such that a number of runs would be possible per heat. In addition the same apparatus should be suitable or adaptable for investigating the behaviour of other gas-saturated molten metals such as silver.

5. In order to heat the small refractory alumina crucibles used slowly and evenly and to provide adequate coupling with the induction coil it was necessary to use a separate susceptor.

6. A controlled atmosphere was required, and hence the system had to be gas-tight. Tank pressures down to 10^{-3} mmHg were contemplated since this was the pressure range of commercial interest.

7. Measurement of stream flow duration was necessary to characterise quantitatively its behaviour. The time measuring technique used previously by Mizoguchi (7) was based on the electrical conductivity of the probes, molten silver and crucible used. In the case of a ceramic crucible another device based on a different principle was required.

4.2 APPARATUS

4.2.1 FURNACE AND VACUUM EQUIPMENT

The basic melting and vacuum facility consisted of a vacuum melting and casting unit (type IM 28 1b) with a 400 volt, 3000 Hertz, 50 kilowatt power supply. At the side of the unit was a window for observing the interior of the furnace. The vacuum pumping equipment consisted of an oil vapour booster pump (Type 9B3) capable of an ultimate vacuum of the order of 10^{-4} mmHg. and backed by a rotary pump, type GKS47.

4.2.2 GENERAL

The apparatus used for the steel experiments was based on the experience gained separately by Warner (5), Baxter (6) and Mizoguchi (7). Major modifications were made in the light of the factors enmumerated in Section 4.1.

The high refractoriness and chemical inertness required of a container for molten iron, combined with costs and other supply criteria made the final choice of thermal recrystallised alumina inevitable. The less refractory materials tested during the preliminary trials included 'Pythagoras 1800' and mullite and were all found to be inadequate. Fig. 4.1 shows a 'Pythagoras 1800' tube that

failed at 1450°C when the wall (3mm thick) was subjected to a pressure differential of one atmosphere.

A separate susceptor was required between the induction furnace and crucible. Hence the iron charge was contained in high purity thermal recrystallised alumina tube located inside a graphite susceptor by a water-cooled brass holder (Fig. 4.2) which, in turn, was positioned on top of an arrangement incorporating a pneumatic-powered and lever-operated bellows (Fig. 4.3) for quick and precise positioning of the charge container. A schematic diagram of the overall apparatus is shown in Fig. 4.4.

4.2.3 PNEUMATIC SYSTEM

The pneumatic circuit is shown in Fig. 4.5 and consisted of two-port valves for stopping a cylinder in midstroke, and locking it in position. Two flow regulators were linked to each cylinder for adjusting the speed of the movement of the pistons; these were adjusted to ensure that the plane of the top of the flange was always horizontal, otherwise during the movement of the pistons the alumina could be inclined to the susceptor with disastrous consequences. A line pressure of 100 lb/in^2 was required to maintain the system in the fully extended position with the chamber at about 10^{-3} mm Hg.

A 'PYTHAGORAS 1800' CRUCIBLE (WALL THICKNESS 3mm) THAT FAILED AT 1450°C WHEN SUBJECTED TO A PRESSURE DIFFERENTIAL OF ONE ATMOSPHERE.

FIG. 4.1

ALUMINA CRUCIBLE ATTACHED TO THE BRASS CRUCIBLE-HOLDER.

FIG. 4.2

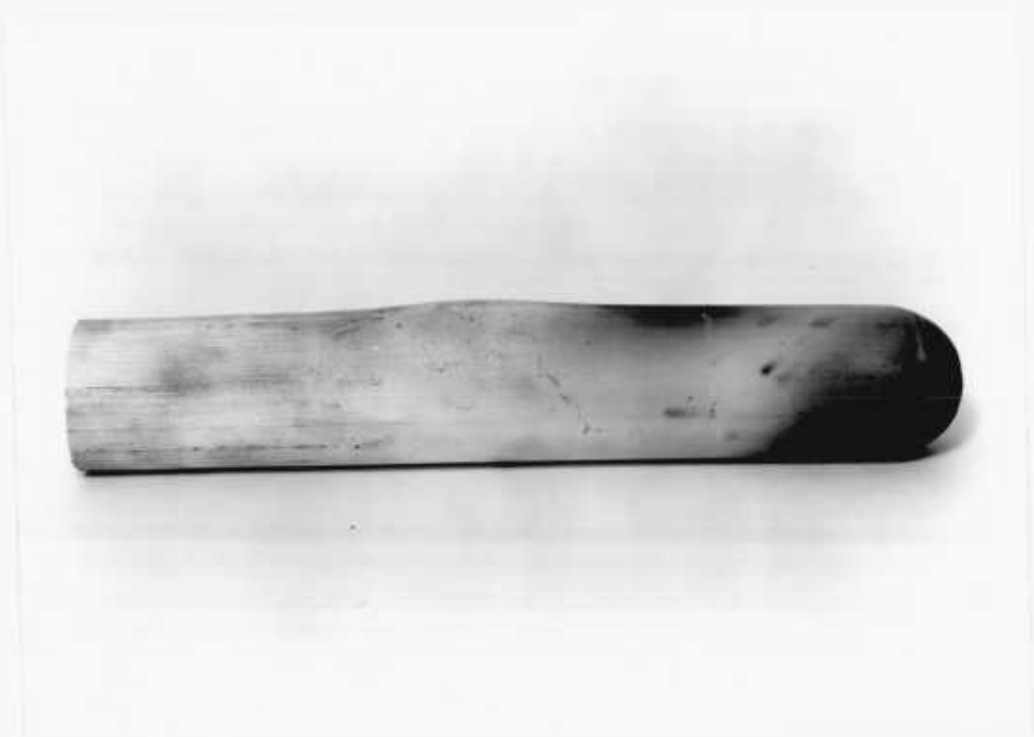

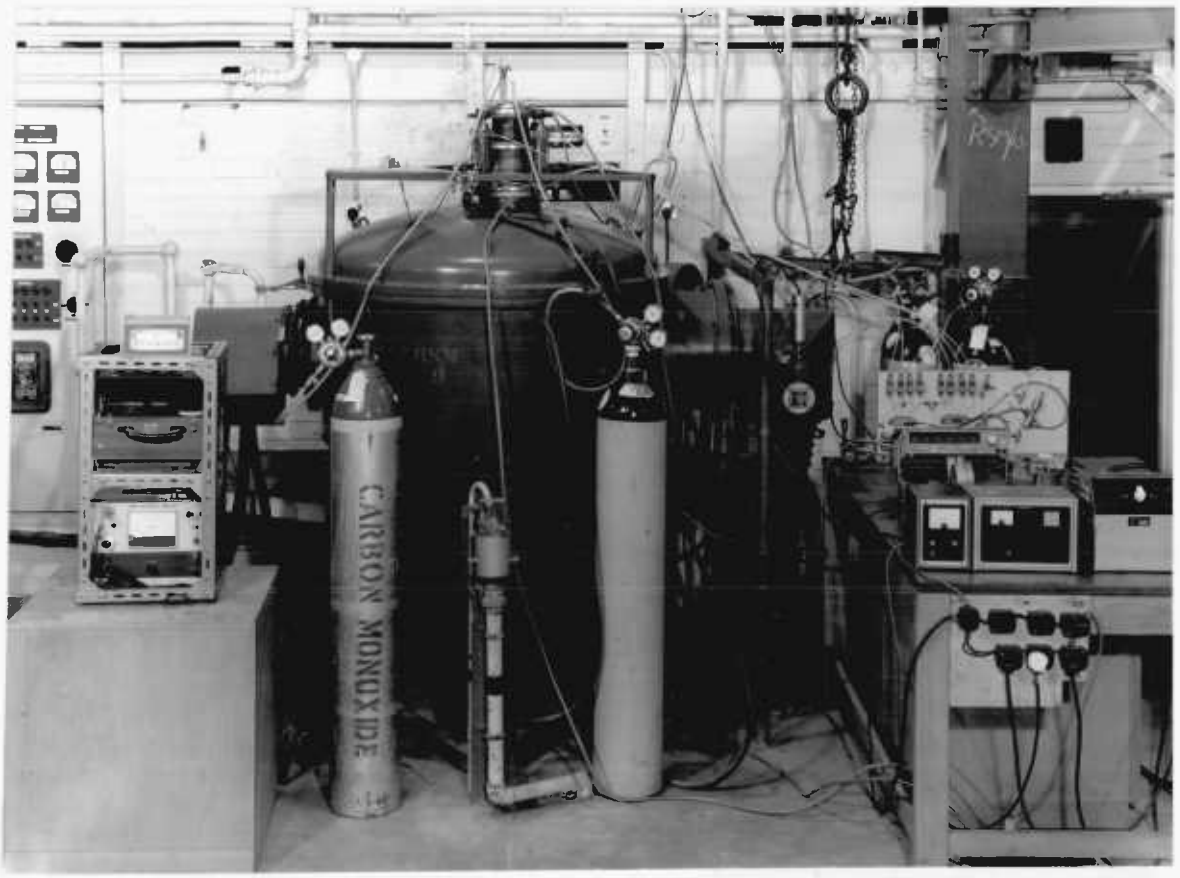

FIG 4.3

THE EXTERNAL APPEARANCE OF THE ENTIRE EXPERIMENTAL SYSTEM.

KEY to

the schematic representation of the apparatus for stream degassing of molten iron (Fig. 4.4.)

1. Thermocouple
2. Stopper rod
3. Surface gas lance
4. Melt gas lance
5. Allan screw for tightening brass lid
6. Brass top lid
7. Brass crucible-holder (water-cooled)
8. Top of bellow arrangement
9. Bellows
10. Brass clip fastened to alumina crucible
11. Compression plate
12. Allan screw for tightening compression plate
13. Alumina crucible
14. Platform for bellow arrangement (water-cooled)
15. Graphite susceptor-holder (water-cooled stainless steel)
16. Screw for fastening susceptor to mild steel flange
17. Mild steel flange
18. Top lid of chamber
19. Refractory cement support for induction furnace
20. Iron charge in alumina crucible
21. Induction coil
22. Graphite susceptor
23. Steel drum
24. Plumbago
25. Steel disc (platform)
26. Observation window through which stream is photographed
27. Melt observation (silica) window. 28. Main vacuum chambe

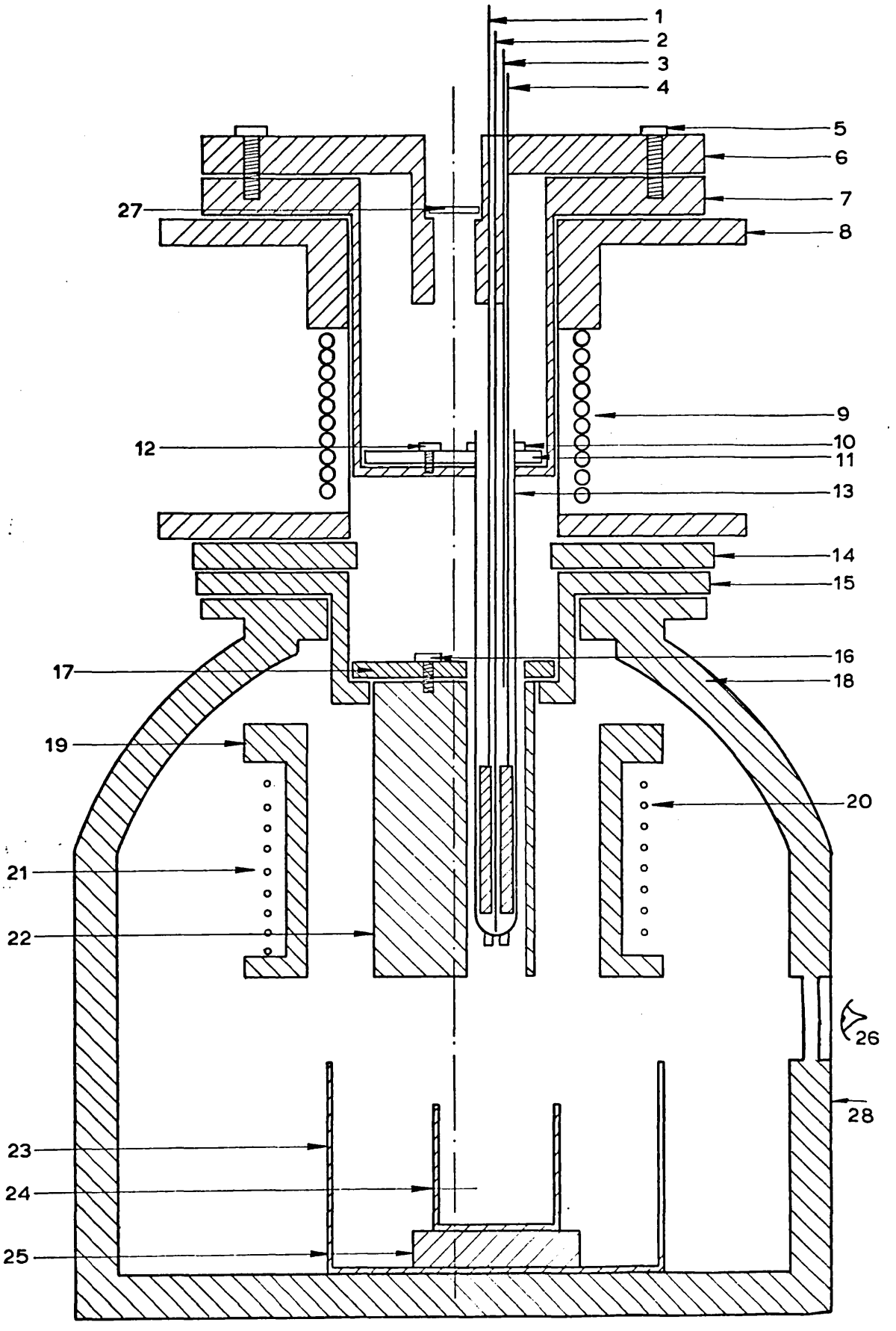

FIG.4.4 SCHEMATIC REPRESENTATION OF THE APPARATUS FOR STREAM DEGASSING OF MOLTEN IRON (KEY TO NUMBERS ON OPPOSITE PAGE)

Key to Fig. 4.5

A	Three piston lever operated 5 port valve S/562
B	Air/oil reservoirs.
C	Sub base mounted valves (M/1702)
D	Shuttle valve (S/575)
E	2-port poppet valve (S/534)
F	Manifold
G	Unidirectional flow regulators (S/650)
H	Cylinders with pistons.

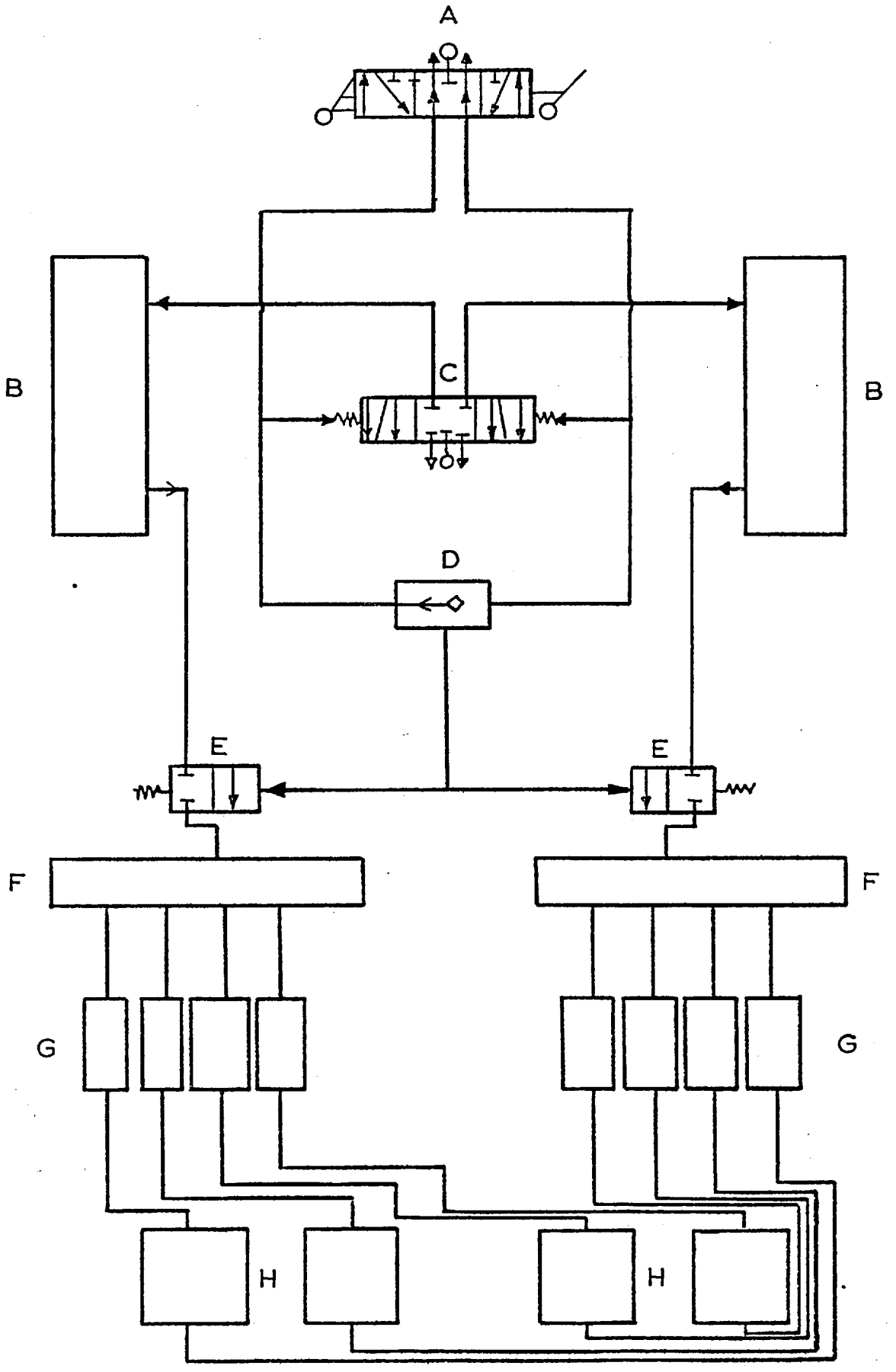

FIG. 4.5. PNEUMATIC CIRCUIT

4.2.4 BRASS TUBE-HOLDER

The photographs and detailed schematic representation of the brass tube holder are shown in Figs.(4.2)(4.6)(4.7). The tube holder was designed to take up to three tubes at a time and was heavily watercooled. Illustrations of the detailed design are shown in Fig (4.6) and (4.7).

Two 36mm diameter stainless steel rods were designed for plugging off whichever of the three holes was not in use for holding alumina tubes. The tubes and plugs were each firmly held by a brass clip at the top, and tightly sealed to the base of the arrangement with a compression plate and O-ring seals. The underside of the bottom flange adjacent to the hot graphite was made of a copper sheet to enhance rapid heat transfer from the hot zone to the cooling water.

4.2.5 TOP LID

A separate gas-tight lid was designed. Essentially this consisted of a melt observation window and facilities for the possible use of three tubes simultaneously. Guides were provided through which the probes were located to ensure that no probes were touching each other or in direct contact with the crucible.

4.2.6 GRAPHITE SUSCEPTOR

A schematic representation of the graphite susceptor

is shown in Fig. 4.8; a photograph of a crucible attached to the brass holder and protruding through the base of the susceptor is shown in Fig. 4.9. The graphite was machined from a 120 mm diameter, 340 mm long CS grade graphite cylinder. It contained three channels, each with a diameter of 44 mm with centre on radius 26mm. The graphite was bolted to a 132 mm OD, 6 mm thick stainless steel flange with three matching holes. In operation the flange was positioned on the lower flange of a water-cooled stainless steel holder located on the vacuum chamber lid. Before use, the graphite was "degassed" by maintaining it at 1600°C for eight hours under vacuum.

4.2.7 ALUMINA CRUCIBLE

Each alumina tube was 480 mm long, 28.5 mm ID, 35.5 mm OD nominal, with a tolerance of ±2 mm as ordered; those with OD of 2mm greater than specified were either rejected or ground down on a diamond-carborundum impregnated wheel while those significantly undersize were wrapped up to size with 'PTFE' tape in sections where the tube dimensions were critical. Brass clips were attached to the top of each tube to prevent it from slipping into the chamber under vacuum.

The choice of small ID tubes brought about operational difficulties: there were not enough clearances

between the probes and this sometimes resulted in clustering of the probes as illustrated with Fig. 4.10. Fig. 4.11 also shows tube failure resulting from tube erosion because of the inclination of a gas lance against the side of a crucible. The problem was finally eliminated by the provision of special guides attached to the top lid as described in section 4.2.5.

The idea of a possible choice of larger tubes had to be discarded because it implied higher failure rate with the more expensive materials since the thickness would be greater and hence more susceptible to failure by thermal shock.

4.2.8. NOZZLES

Holes were drilled through the base of the tubes with a chamfer at the nozzle entry to prevent flow separation. This was confirmed on a single phase flow of degassed iron which showed no evidence of stream expansion or contraction. The nozzle diameters were measured before and after each run to check for nozzle deformation and erosion using a travelling microscope. The nozzle length was measured using a micrometer with a special attachment. This is illustrated in Fig. 4.12. The nozzle length was always less than the thickness of the base of the tube, by the depth of the chamfer and was generally

of the order of 2-3 mm.

4.2.9. STOPPER ROD

The stopper rod (Fig. 4.13) consisted of two lengths of 5 mm diameter thermal recrystallised alumina held together by a stainless steel sleeve 5.5 mm ID, 6.5 mm OD, 40 mm long. The overall length of each stopper rod could vary between 830 and 930 mm. The longer of the two components was initially 670 mm long and tapered at both ends to facilitate reuse of the same rod before being retapered to a point with a half vertical angle of 22½°. It was important that the joint, which was normally made with 'Araldite', should not be less than about 300 mm from the metal-gas interface, when using a 90 mm long cold charge. The length of the rod projecting above the top lid carried a brass sleeve, 5.5 mm ID, 7 mm OD, 25 mm long with side arms for springloading the rod to ensure that it was not displaced from the orifice during the heat as a result of mechanical agitation which often occurred during gas bubbling and movement of the bellows. It was essential to grind off 1 mm of the taper and smooth the outermost tip to a hemispherical configuration to avoid deformation of the nozzle during manipulation of the stopper rod or blocking of the nozzle by a fractured stopper rod tip.

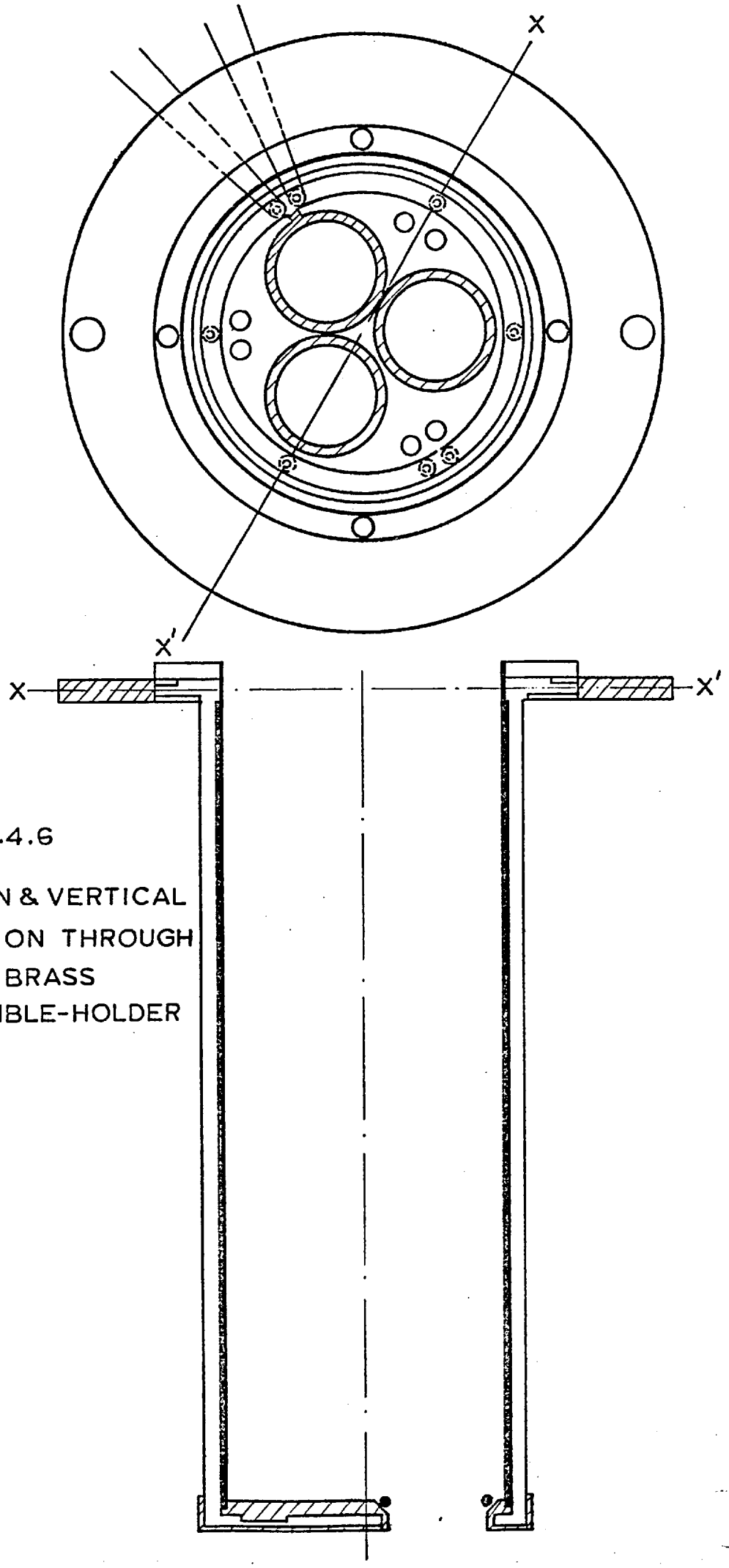

FIG.4.6

PLAN & VERTICAL SECTION THROUGH THE BRASS CRUCIBLE-HOLDER

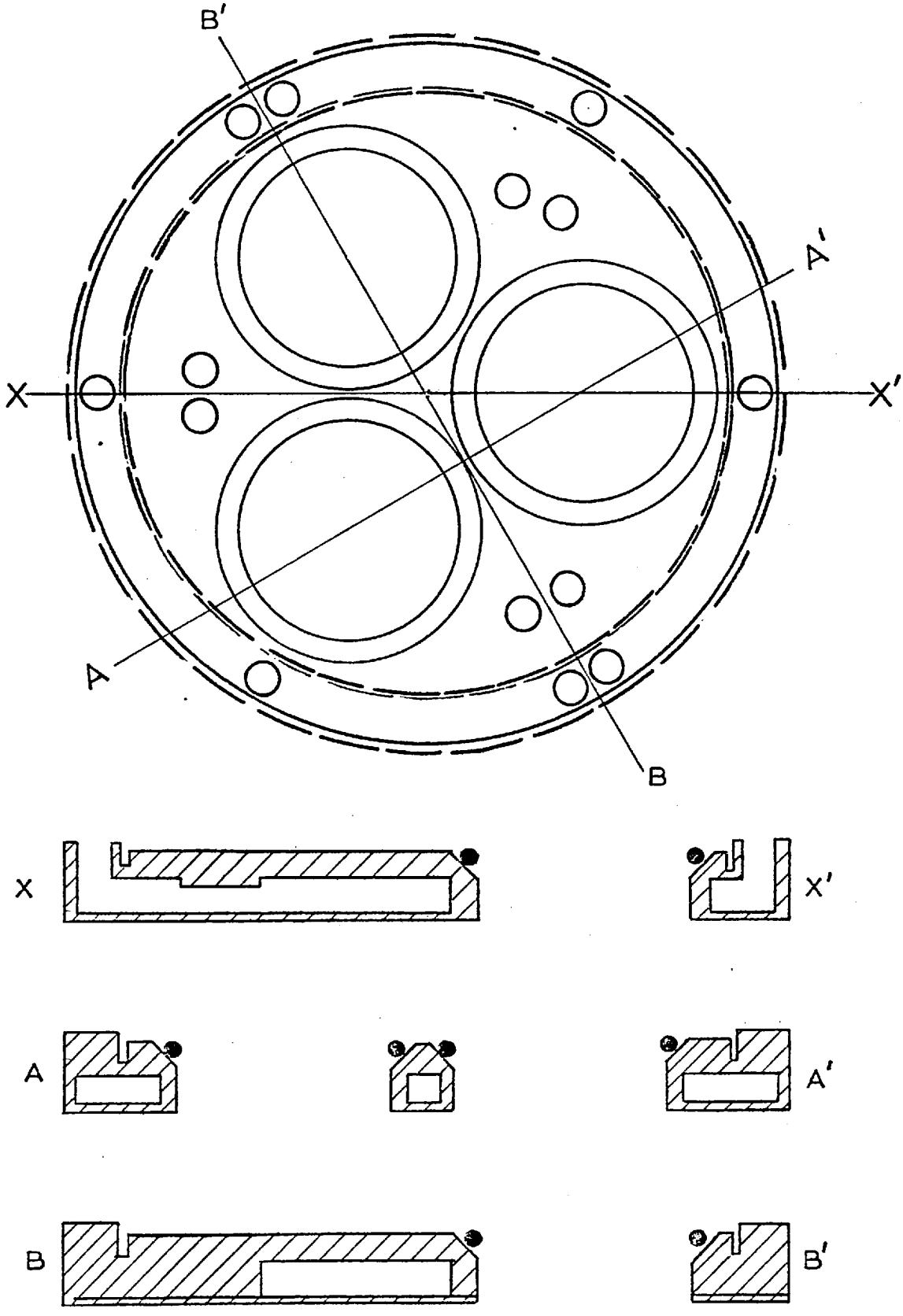

FIG. 4.7 THE PLAN AND SECTIONS THROUGH THE BASE OF THE BRASS CRUCIBLE HOLDER.

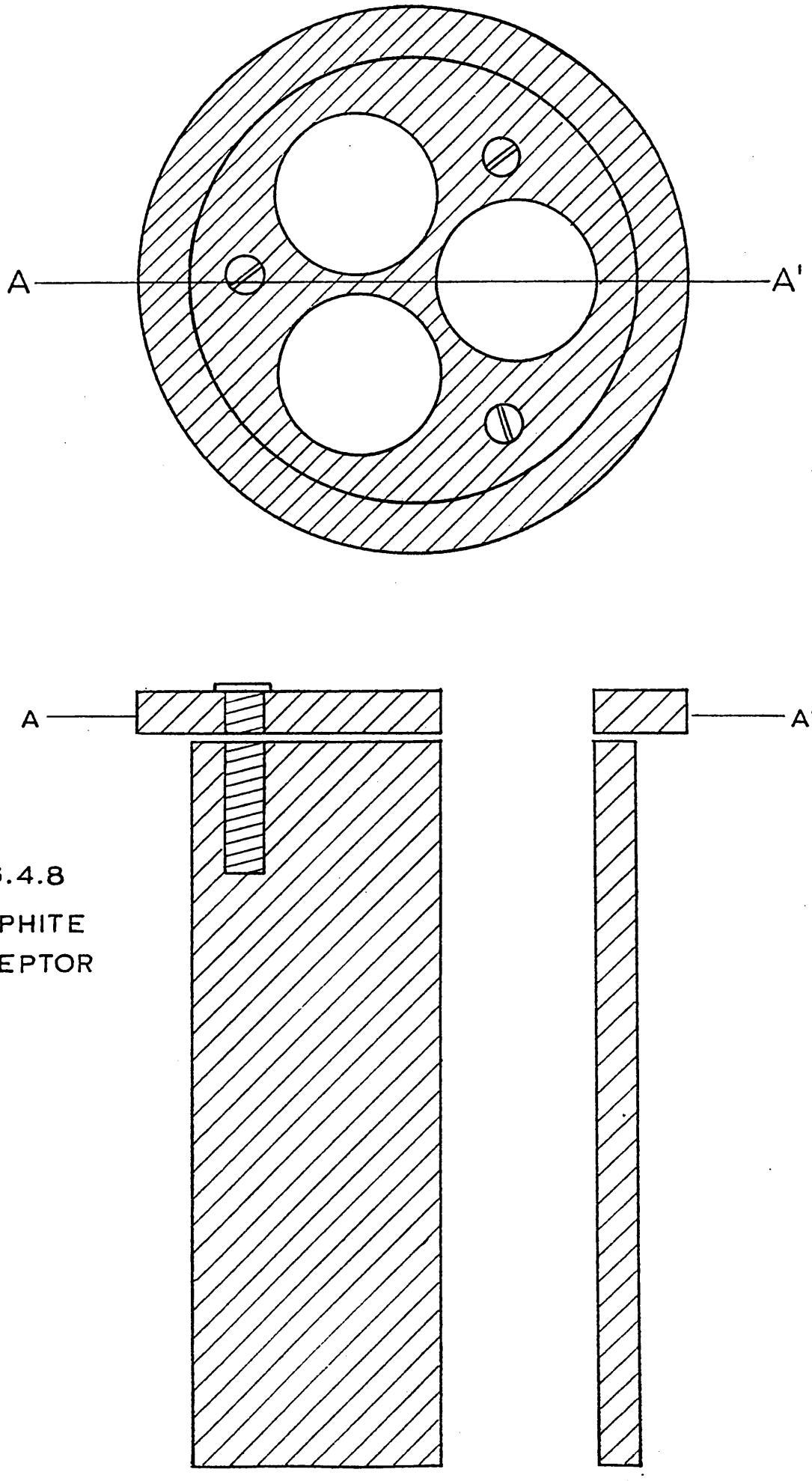

FIG.4.8
GRAPHITE
SUSCEPTOR

AN ALUMINA CRUCIBLE ATTACHED TO THE BRASS HOLDER AND PROTRUDING THROUGH A GRAPHITE SUSCEPTOR.

FIG. 4.9

AN EXAMPLE OF THE CLUSTERING OF PROBES INSIDE AN ALUMINA CRUCIBLE IN THE COURSE OF A RUN

FIG. 4.10

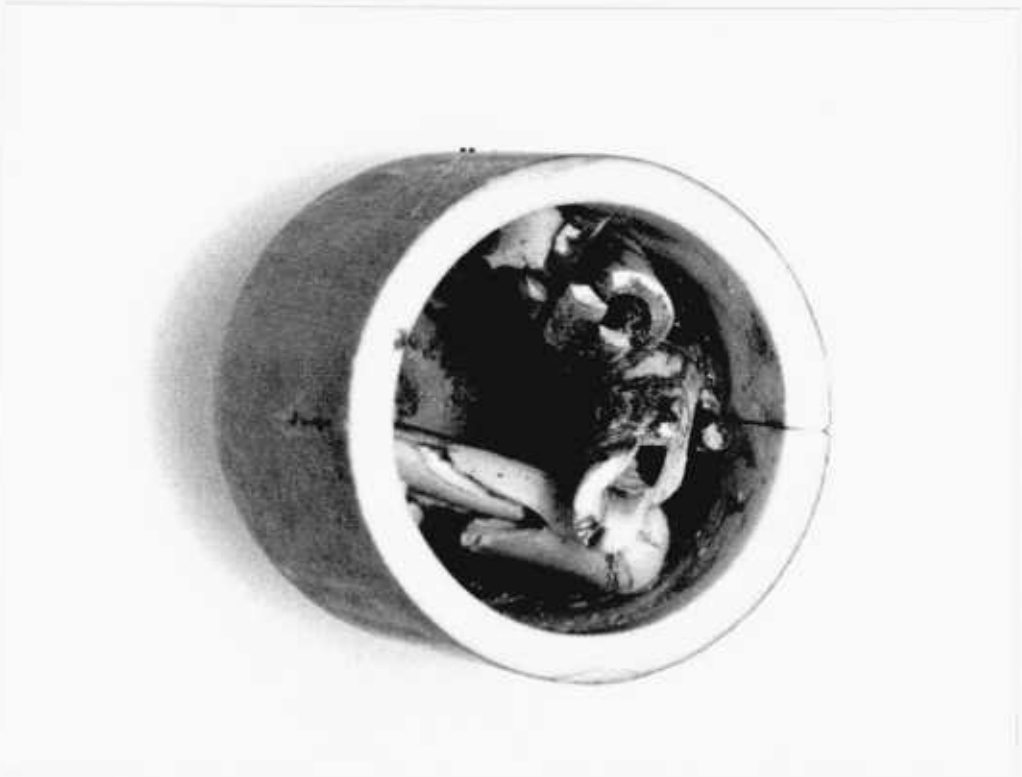

THE EROSION OF AN ALUMINA CRUCIBLE ARISING FROM THE INCLINATION OF A GAS LANCE AGAINST THE CRUCIBLE

FIG. 4.11

CHEMICAL ATTACK OF ALUMINA CRUCIBLE WITH IRON SATURATED WITH $96CO-4CO_2$ GAS MIXTURE.

FIG. 4.11(b)

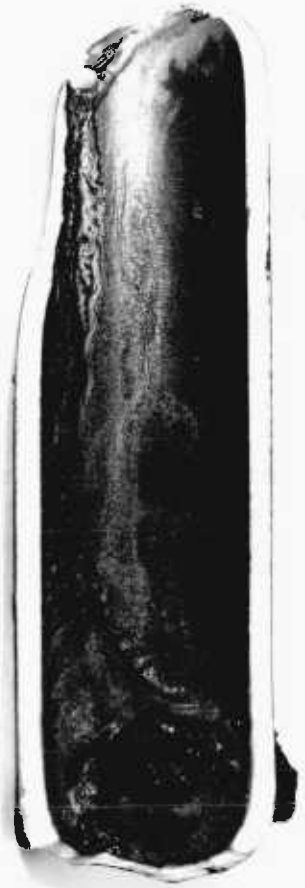

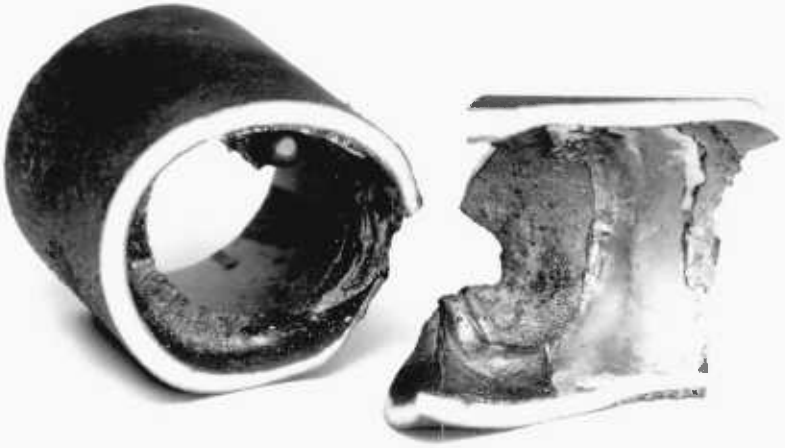

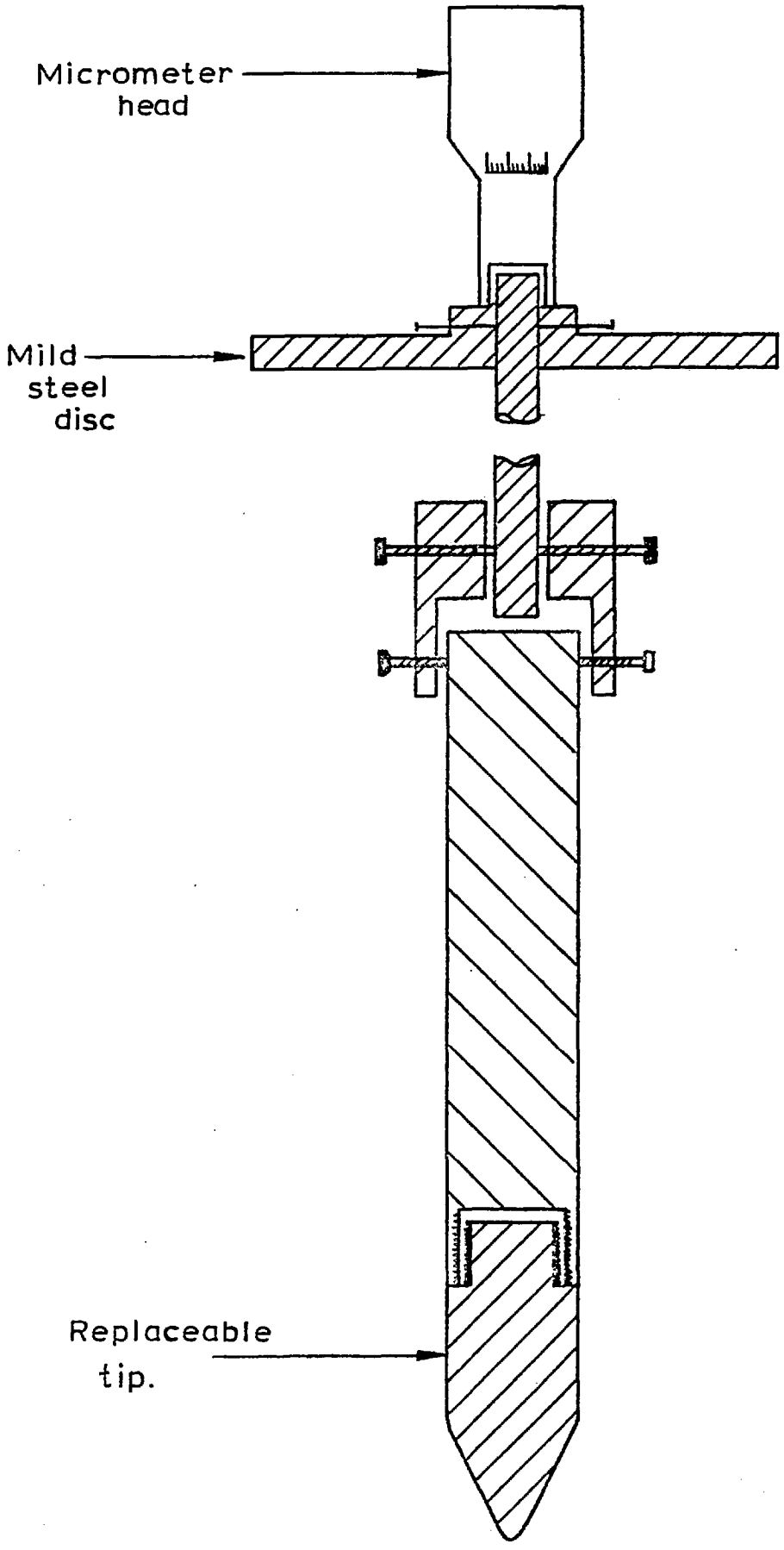

FIG. 4.12 ARRANGEMENT FOR MEASURING NOZZLE LENGTH

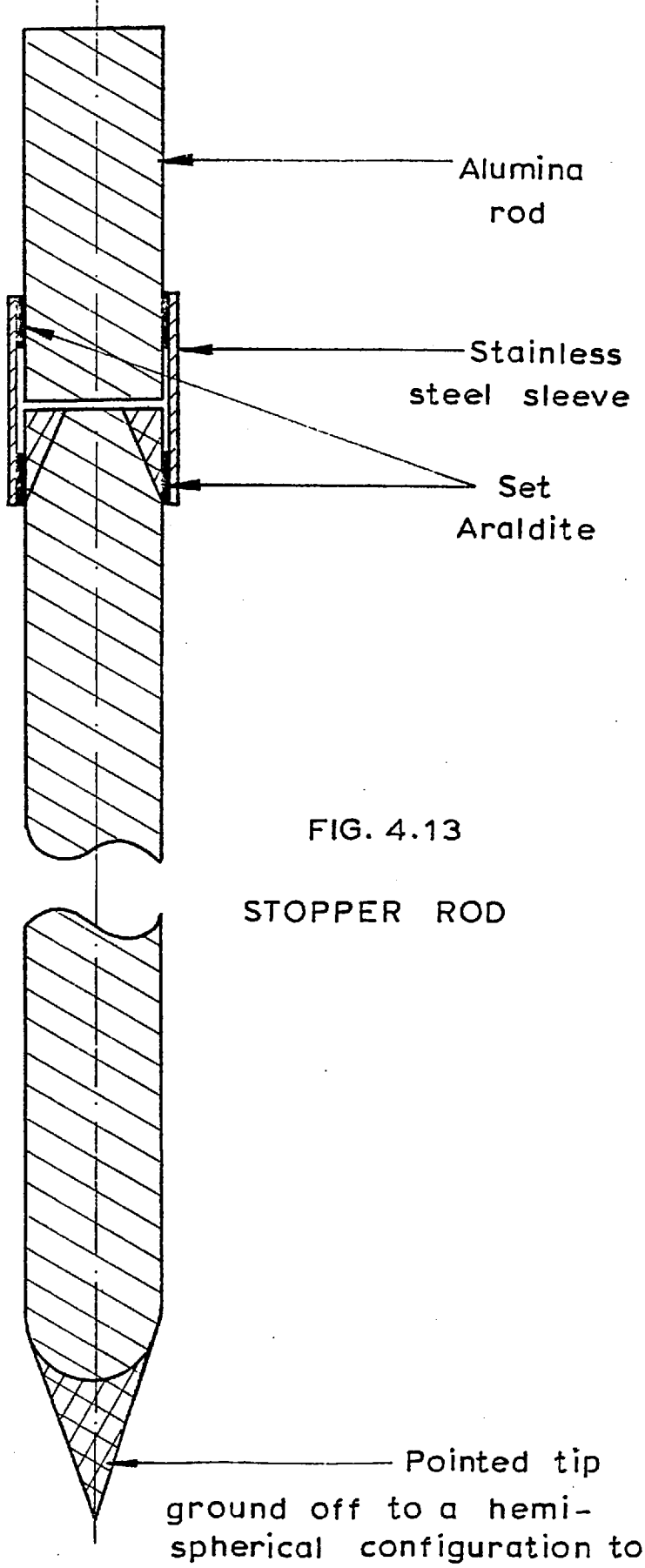

FIG. 4.13

STOPPER ROD

4.2.10 IRON CHARGE

Each charge weighed about 300 grams and consisted of a degreased Armco grade iron rod 25.4 mm diameter and 90 mm long at the centre of which a 9 mm hole was drilled through which the stopper rod was located. When alloying additions were to be made a 4 mm, or 2-2 mm, diameter blank holes were drilled at the top of the charge to take the alloying additions in powdered form; this was necessary to reduce the risk of attack of the alumina tube which would occur as a result of direct and prolonged contact between alloying additions and the tube. A typical analysis of the Armco iron used is given in Section 3.1.3.

4.2.11 HEATING AND COOLING CYCLES

A typical campaign lasted about 10 hours including heating, saturation, actual experimentation and cooling cycles. The optimum heating rate was 400°C per hour up to 800°C and subsequently 300°C per hour.

Heating was carried out with the bellows fully extended and the charge in the centre of the induction coil. Immediately after a run oxygen-free nitrogen was slowly bled into the chamber to 1 atmosphere pressure and the system cooled down to 800°C at 300°C per hour and subsequently brought to room temperature in a further 1½ hours.

The charge was heated under argon. The tank pressure was maintained at about 10^{-3} mm Hg until just before the run when the chamber pressure was adjusted to a predetermined value by bleeding an inert gas into the chamber to protect the graphite susceptor from oxidation.

The nozzle was always 'frozen' if the chamber was adjusted to pressures higher than 100 mm Hg. This restricted investigations to low tank pressures and any chamber pressure adjustment was made only just before the run.

4.2.12 MELT SATURATION

Two gas lances were used, one supplying gas into the melt, and the other above the melt. Each lance was made of a 2 mm bore, 4 mm OD alumina tube. The depth of immersion of the immersed lance was 50 mm below the melt surface. The orifice of the 'surface lance' was about 10 mm from the metal-gas interface. The gas flow-rates through the melt and surface lances were 80 and 100 cm^3/min respectively. Prior to bubbling the desired gas, the melt was purged with argon. Bubbling of the gas solute was for 30 minutes except when there was leakage and saturation was consequently terminated prematurely. During the flow of the metal stream the immersed lance was taken out of the melt with the supply of gas to the

surface via both lances continued, to prevent the transfer of gas solutes from the melt into the bulk gas phase.

4.2.13 PHOTOGRAPHY AND DURATION OF FLOW OF STREAM

The discharge operation was carried out manually by swiftly lifting the stopper rod out of the nozzle with the system in the heating position.

The system was lowered for photography after about two seconds of the start of stream flow and raised back into the heating position immediately after the film ran out. Thus the alumina crucible was not normally maintained at the lowest position for more than about six seconds. It was unnecessary to lower the system when no photograph was to be taken.

The discharge time was measured using an analogue photodetector which was suitable for detecting continuous changes in light level.

The detector collected the radiation from the steel stream when it emerged from the nozzle and the detector output was recorded. The output voltage from the circuit increased directly with light intensity. As the alignment of the photocell with the metal stream was not critical, the photocell was simply pointed at the position of the stream trajectory through the observation window.

The tank pressure was measured with Pirani and dial

gauges which were previously calibrated. The outputs from both the photocell and Pirani gauges were fed into a two-pen "Servoscribe" recorder throughout the run. Typical chamber pressure and intensity curves during the stream discharge are shown in Figs. (5.3), (5.4).

An advantage of the photocell-recorder arrangement was its continuity of response as opposed to an electronic timer which had to be reset manually if a stream flow was prematurely interrupted or if a few drops emerged prematurely from the nozzle.

A "Fastax" high speed movie camera - category V, type WF4ST - with 50 mm lens, was used with a peak framing speed of 2870 pictures per second, and always aligned with the tube orifice before the commencement of heating. The view seen by the camera included about 30 mm of the bottom of the alumina crucible, the nozzle exit and up to 300 mm downstream; where nozzle extensions were used only about 2 mm of nozzle was in the field of view. The brightness of the liquid iron at 1600°C provided adequate illumination.

An electronic circuit was designed to determine accurately which part of the stream discharge duration was photographed to correlate stream behaviour with small changes in tank pressure. Although a remote control

switch was designed so that one operator could lift the stopper rod and operate the camera its use was abandoned; instead mamual operation of the camera by a second observer was carried out to avoid film wastage arising from nozzle blockage. The camera was only started when a 'good' stream was observed. The same second observer also took control of the operation of the pneumatic system during the run.

The metal stream was received by a plumbago crucible prealigned with the alumina crucible, placed inside a steel drum at the base of the chamber. When vigorous break-up occurred it was usual to collect up to 60% of the charge in the form of powder outside the plumbago crucible, the majority from the chamber wall and some agglomerated. In the latter case analysis of powder became impossible.

4.2.14 EXTENDED NOZZLES

Stream break-up was not observed with nitrogen saturated iron employing short smooth nozzles even at tank pressures below 10^{-3} mmHg. Therefore a substantial effort was concentrated on the development of a technique for sintering alumina cement or another smooth narrow-bore alumina tube (extension nozzle) to the bottom end of the alumina crucible (substrate).

In either case the base of the substrate was ground flat and a former, in the form of a precision-machined rod was used to ensure alignment of the hole through the substrate with that of the extension nozzle. Satisfactory results were obtained with 101 grade of alumina cement powder, mixing 20 cc of binder (made up of 18 cc of orthophosphoric acid and 2 cc of sodium silicate) with 100 grams of the cement. A satisfactory preparatory technique included air drying for about 12 hours, oven drying in 3 stages at 50°, 100° and 200°C each for 12 hours. The former was removed after the third stage and the arrangement was fired either in a muffle furnace at 1400°C for 8 hours or fired 'in situ' during the heating of the charge.Where the extension nozzle was in the form of another refractory tube a two-stage sintering procedure ensured that no separation occurred between the substrate and extension nozzle. This is illustrated in Figs 4.14 and 4.15. This consisted of first cementing the extension tube to the substrate and oven-drying. Finally another layer of cement was placed between the outer insulator and the extension nozzle. Figs. 4.16 and 4.17 show the typical appearance of 'green' and used nozzles.

Key to Fig. 4.14.

1. Alumina crucible

2. Short, narrow bore alumina tube

3. Brass rod (former)

4. Fired alumina cement

5. Alumina tube (short)

6. Alumina cement

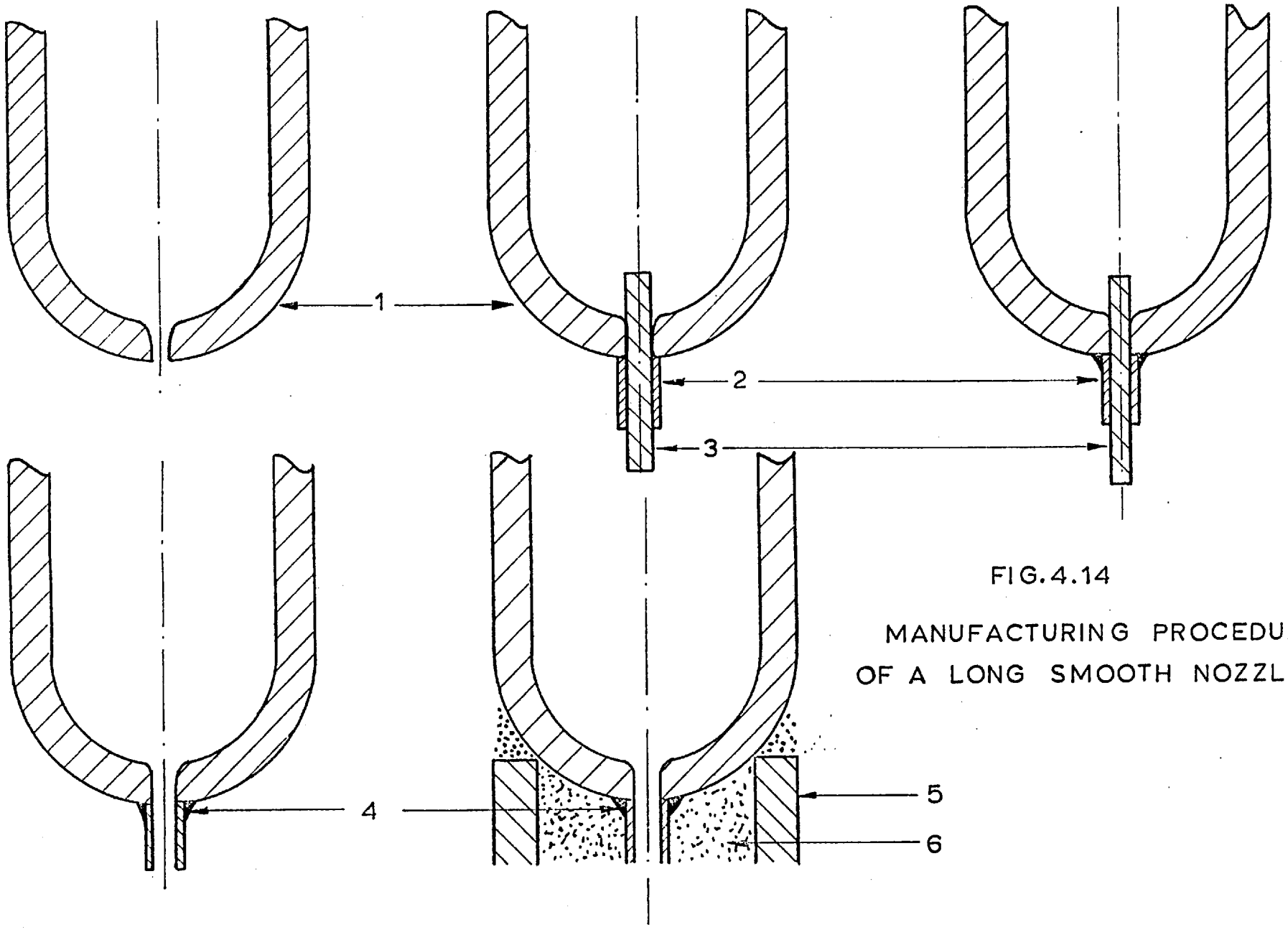

FIG. 4.14

MANUFACTURING PROCEDURE OF A LONG SMOOTH NOZZLE

Key to Fig. 4.15

1. Alumina crucible.

2. Brass rod (former).

3. Fired alumina cement.

4. Nozzle protuberances.

5. Short alumina tube.

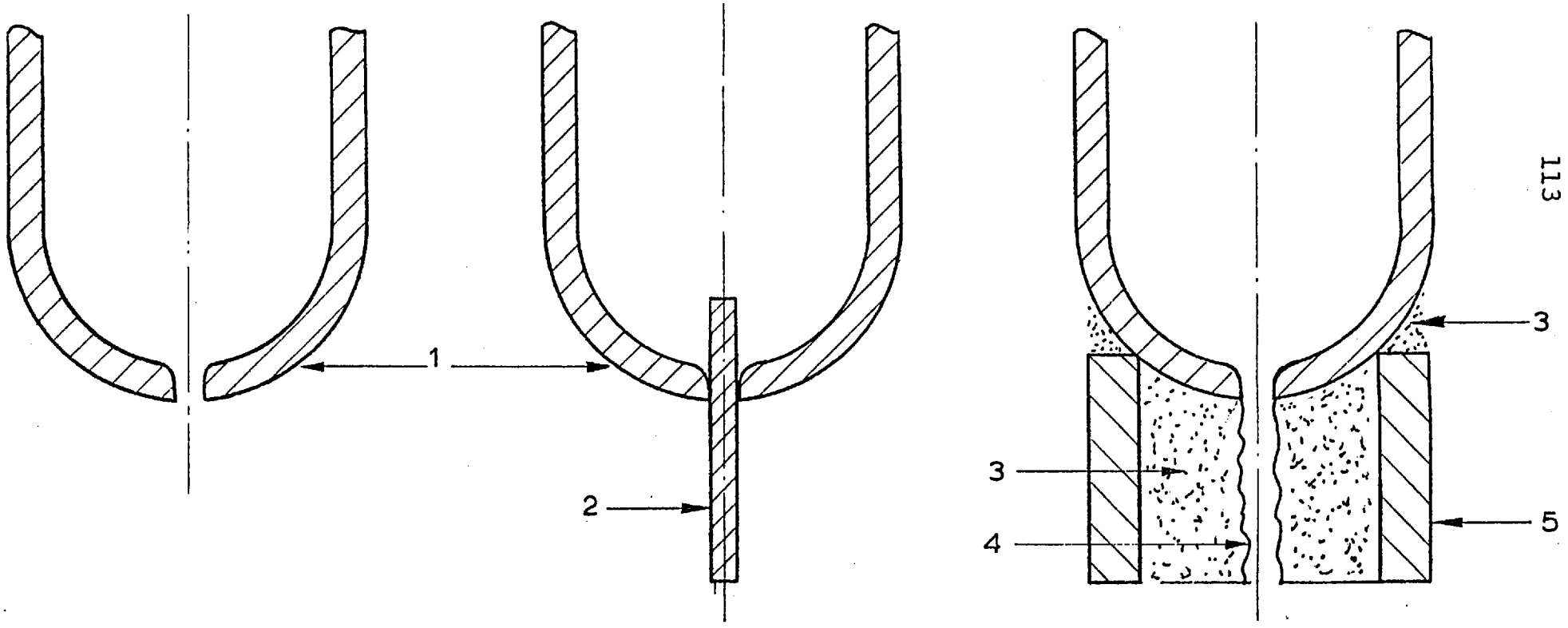

FIG. 4.15 MANUFACTURING SEQUENCE OF AN EXTENDED ROUGH NOZZLE

THE TYPICAL APPEARANCE OF A "GREEN" ALUMINA NOZZLE.

FIG. 4.16

THE TYPICAL APPEARANCE OF A "FIRED" AND USED ALUMINA NOZZLE.

FIG. 4.17

4.3 AUXILIARY EXPERIMENTS

4.3.1 MODIFICATION OF APPARATUS FOR SILVER OXYGEN IN NIMONIC 75.

An attempt was made to use the apparatus of Mizoguchi (7) to study the effect of length-diameter ratios of nozzles on silver stream behaviour. It was found that the electromagnetic coupling between the longer nozzles of length greater than half an inch and the induction furnace, coupled with the low thermal conductivity of Inconel 600, resulted in frozen nozzles. Separate furnaces were built for heating each nozzle. The power to the auxiliary furnace was supplied through leads incorporated at the base of the vacuum chamber.

The method also used by Mizoguchi to seal his nozzles into the base of the tundish proved inadequate in the situation where the joint was heated from below by the separate furnace. Each nozzle is now welded to the tundish. Although the modified apparatus was not used in the current exercise its suitability has been demonstrated.

4.3.2 SILVER-OXYGEN STREAMS THROUGH ALUMINA NOZZLES

Mizoguchi obtained discharge coefficient values for oxygen saturated silver flowing through Nimonic 75 nozzles.

In general these are high. (7)

The rather low discharge coefficient values obtained even for degassed iron suggested a significant contribution by frictional effects when alumina nozzles were used, hence some silver-oxygen runs were carried out in the same system used for molten iron to facilitate correlation. The silver was purified as described elsewhere (7) and cast in graphite mould into 1 inch diameter rods. Subsequent preparation was as for the iron rods described in section 4.2.10.

4.4. SUMMARY OF THE PRECEDURE FOR EACH RUN

4.4.1 GENERAL EQUIPMENT AND ROUTINE PREPARATION

1. Adjust flow regulator settings on pneumatic system for maximum speed.
2. Check, clean and grease all 'O'-rings and clean chamber, graphite susceptor, steel drum and plumbago crucible.
3. Prepare thermocouple, stopper rod, and both gas lances, making adequate provision for spares.
4. Take measurement of alumina tube and ensure that the charge to be used slides into the tube; look out for tube narrowing down at the bottom and if so machine down charge to suit.
5. Fasten alumina tube and stainless steel blanks to

the brass crucible holder. The procedure should be such that the entire charge is within the effective heating zone and that when system is lowered for photography the nozzle exit appears in the field of view of the camera (Fig. 4.19).

6. Check that pressure of gas in cylinder supplying the pneumatic line is not less than 600 lb/in^2.

4.4.2 RUN PROCEDURE

7. Check the electrical connections to illumination bulb inside chamber and shield adequately against metal spray.

8. Locate steel drum and plumbago crucible and ensure their alignment with the induction furnace.

9. Replace chamber lid.

10. Locate graphite susceptor in the stainless steel holder, position this on chamber lid and check that the plumbage crucible is aligned with the channel to be used to take the alumina crucible.

11. Cover stainless steel flange with steel disc, and switch on backing pump to test vacuum tightness. If the pressure attained is of the order of 0.4 torr within 10 minutes the chamber lid is correctly located and all seals O.K.

12. Position watercooled mild steel annulus on graphite-holder.

KEY to

the schematic representation of the optimum relative positions of crucible and induction furnace during the heating cycle (Fig. 4.19): Bellows fully extended.

Position	Distance from reference line (mm)
Y	817
X	812
W	802
V	582
U	562
T	552
S	537
R^1	497
R	472
Q	432
P	412
N	392
M	382
L	375
K	305
J	275
H	190
G	110
F	97
E	82
D	42
C	40
B	20

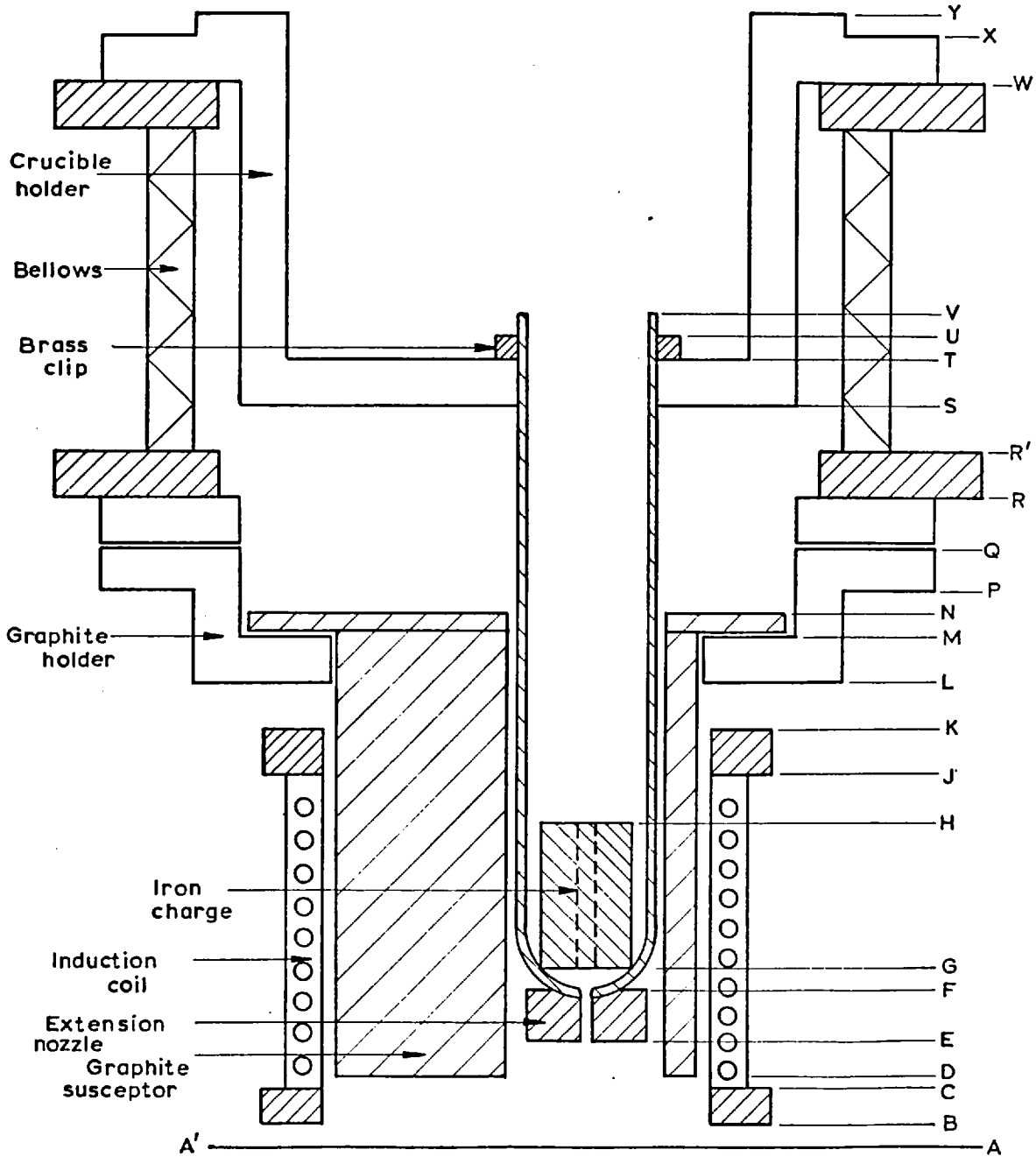

FIG. 4.19 OPTIMUM RELATIVE POSITIONS OF CRUCIBLE & INDUCTION FURNACE DURING THE HEATING CYCLE (Key to diagram on opposite page)

13. Locate bellows arrangement on steel annulus.

14. Locate brass-alumina arrangement.

15. Cover the flange of alumina-holder with steel disc and test system for air tightness as for 11.

16. Switch on illumination bulbs in chamber, lower system and align camera with bottom of alumina; after alignment ensure that susceptor and camera positions remain unchanged until after the run.

17. Remove the brass-alumina arrangement and carefully slide into the crucible the iron charge and reposition the arrangement on top of the pneumatic arrangement.

18. Locate the stopper rod and test for nozzle-stopper rod seal.

19. Locate top lid and test the system again for possible displacement of the stopper rod.

20. Raise the system to the 'heating position' and lightly springload the stopper rod.

21. Turn on all necessary water taps for water circulation through all components designed to be watercooled.

22. Switch on the HF.

23. Supply inert gas above charge.

24. Commence heating, increasing power input by 2 kilowatt every fifteen minutes up to 800°C and subsequently by

2 kilowatt every thirty minutes.

25. Continually check for leakage of gas through stopper rod-nozzle joint, and arrest any leakage by lightly rotating and further springloading the stopper rod.

26. Load camera and test for correct loading; check that timing light functions properly; lubricate camera and set voltage for film speed at 90 volts.

27. Link both Pirani gauge and photocell with recorder.

28. Test that photocell is set to respond to changes in light level, choosing the 1 and 20 volt ranges for pressure and photocell lines respectively and set recorder running at 30 mm/min.

29. When system was heated to 1480°C and above, alert personnel to watch out for arcing and metal leakage; (leakage may be arrested by rotating the stopper rod, and arcing may be arrested by increasing chamber pressure to above 1 mmHg.

30. Switch over from inert gas to the actual experimental gas (after purging the melt for at least five minutes) and, in the case of H_2 or CO- containing gas mixtures link top of chamber via rubber tubing to a bunsen burner to burn off escaping gases.

31. Switch on power supply to timing light, camera and master switch.

32. Ensure that the power setting on the HF will ensure a superheat of about 80°C (i.e. charge at 1600°C).

33. Adjust tank pressure as desired for the run.

34. Change recorder speed to 600 mm/min.

35. Measure charge temperature and pressure above the melt.

36. Lift the gas lance and thermocouple out of the melt.

37. Swiftly lift stopper rod out of melt. In the event of no stream emerging, leave system in heating position, and continue gas bubbling; further increase power by 4 kilowatts in two steps.

38. When photograph is to be taken the system should be lowered by the second observer operating the pneumatic controls after about 2 seconds of stream commencement. Camera should be operated manually when the bottom of the nozzle has reached the lowest position.

39. Raise the system back to the 'heating position' immediately after the film runs out.

40. Immediately after all the charge has run out of the crucible, shut off all pumps and commence bleeding nitrogen into the chamber.

41. All probes should be raised out of the hot zone and occasionally rotated to ensure that they do not touch either the crucible or each other.

42. Cool system at the same rate as it was heated up to avoid tube failure.

The total work involved for each run normally took about one man-week. This included the time spent in making up extension nozzles, stopper rods, gas lances, testing for leak tightness and optimisation of vacuum chamber, flanges, stopper rod - crucible, and all the other ancillary equipments.

4.5 MAJOR EXPERIMENTAL PROBLEMS

4.5.1 INTRODUCTION

Various authors have considered the problems experienced in the use of refractory oxides to contain molten iron (44) (45)(46).

These oxides rarely consist of a homogeneous material, for example impurities such as Fe_2O_3 and SiO_2 are often found in 'high purity' thermal recrystallised alumina crucibles which may have their origin in the raw materials. In service these reactive impurities may be the cause of local softening.

During contact with iron melts iron oxides may be precipitated at the crucible surface or embodied in the material by diffusion. For example Fischer, Hoffmann and Brotzmann (47)(48) have reported the partitioning of oxygen between iron melts and alumina, zirconia or magnesia crucibles. Oxygen in iron originally containing

(O) = 0.15 wt-% in a magnesia crucible was reduced by 50% while the crucible FeO content at the surface correspondingly increased from the initial level of 0.4 to 5.2 wt-%. They showed that within one hour the FeO diffused up to 5mm into the nonporous magnesia crucibles, suggesting structural softening.

The major problems encountered in this work were concerned with the failure of alumina crucibles and stopper rods. Other problems, though of secondary severity, included a long campaign time per heat and the wide tolerances involved with the specifications of refractory materials. In the case of oversize tubes this meant either a high rejection rate of the alumina tubes as supplied or a substantial effort in grinding down to suitable size (section 4.2.7).

4.5.2 PREFERENTIAL ATTACK OF ALUMINA AT SOLID-LIQUID METAL-GAS INTERFACE.

There was evidence of macroscopic groove formation along the meniscus contour of the crucible-melt-gas interface. The attack was more severe with the more oxidising gases, and particularly if the contact time between the melt and crucible was prolonged beyond about thirty minutes, as was often the case when the nozzle was blocked. The attack may be due to any of the following:

1. Erosion of the solid surface by the stirred molten iron.

2. Preferential dissolution of alumina by the liquid-gas surface layer due to certain special properties of the surface layer.

3. Chemical attack for which the simultaneous presence at the surface of all three phases is essential.

The same phenomenon had been observed by other workers, (46)(47). In our system once the thickness of the crucible at any section was reduced below a critical value, the thickness could no longer withstand the pressure differential of one atmosphere and consequently cracked.

4.5.3 REDUCTION OF ALUMINA BY GRAPHITE SUSCEPTOR

Thermodynamically the decomposition of alumina by the reaction:

$$Al_2O_3 + 3C = 3CO + 2Al \quad \ldots\ldots\ldots\ldots\ldots 4.0$$

is feasible at high temperatures ($> 1700°C$) and very low pressures. If during the campaign the crucible was resting against the graphite, localised reduction in crucible thickness occurred leading to failure.

4.5.4 CHEMICAL ATTACK OF ALUMINA

Chemical attack of alumina was frequently encountered

with iron melts saturated with $CO-CO_2$ mixtures, the problem intensifying with increasing oxygen potential of the gas mixture.

The thermodynamics of Fe - O - Al are well documented (49)(50)(51)(52)(52). Fig. 4.20 shows the $FeO - Al_2O_3$ equilibrium diagram. Many workers have investigated the formation of hercynite during steelmaking by the reaction of molten steel when aluminium is added as a deoxidiser (50a) (52) (54) (55). McLean and Ward (52) investigated the thermodynamics of the reaction

$$Fe(l) + \underline{O} + Al_2O_3(s) = FeO.Al_2O_3 \quad \ldots\ldots\ldots 4.1$$

They measured the solubility of oxygen in liquid iron which was equilibrated with alumina and hercynite between 1550 and 1750°C (52); from their own work and other data they produced a diagram showing the relationship between the activities of aluminium and oxygen to predict the relative stability of hercynite and alumina (Fig. 4.21).

Pillay et al. equilibrated mixtures of hydrogen gas and water vapour with molten iron contained in an alumina crucible at 1600°C and measured the oxygen content. They observed that the interior of the tube was blackened by a material which they later identified as hercynite, when

the oxygen concentration was equal to or above 0.058 wt-% (54).

Brokloff also equilibrated liquid iron, hercynite and alumina with water vapour - hydrogen gas mixtures between 1450 and 1700°C, and showed that hercynite could form at oxygen levels even lower than 0.058 wt-% (55) in close agreement with McLean and Ward who showed the critical level to be = 0.051 wt-%.

The free energies for the formation of hercynite from

1. dissolved oxygen, liquid iron and alumina
2. its component oxides and
3. dissolved oxygen, aluminium and liquid iron ...

are available in recent publications (52).

$$Fe(l) + \underline{O} + Al_2O_3 = FeO.Al_2O_3(s) \quad \ldots\ldots\ldots \quad 4.1$$

$$Fe_xO(l) + (1-x)\,Fe(l) + Al_2O_3 = FeO.Al_2O_3(s) \quad 4.2$$

$$Fe(l) + 2Al + 4\underline{O} = FeO.Al_2O_3(s) \quad \ldots\ldots\ldots \quad 4.3$$

$$\Delta G^\circ\ (4.1)\ (\text{calories/mole}) = -34{,}950 + 12.99T\ (\pm 500) \quad 4.4$$

$$\Delta G^\circ\ (4.2)\ (\text{calories/mole}) = -7{,}918 + 1.46T\ (\pm 1200) \quad \ldots \quad 4.5$$

$$\Delta G^\circ\ (4.3)\ (\text{calories/mole}) = -328{,}170 + 106.36T\ (3{,}500) \quad \ldots \quad 4.6$$

At 1600°C

$$\Delta G^\circ(4.1)\ (\text{calories/mole}) = -10{,}619 \quad \ldots\ldots\ldots\ldots\ldots \quad 4.7$$

$$\Delta G^\circ\ (4.2)\ (\text{calories/mole}) = -5{,}183 \quad \ldots\ldots\ldots\ldots\ldots \quad 4.8$$

ΔG° (4.3) (calories/mole) = -128,957 ..... 4.9

From the relationship $\Delta G = -RT\ln Kp$ 4.10

At 1600°C the equilibrium constant for the reactions (4.1), (4.2), (4.3) as written are:

Kp (4.1) = 17.36 .....4.11

Kp (4.2) = 4.03 .....4.12

Kp (4.3) = 1.13×10^{15} 4.13

The Henrian activities of carbon and oxygen corresponding to some CO-CO_2 mixtures in molten iron at 1600°C are shown in table 3.1. The oxygen Henrian activity, h_O corresponding to 90 CO - 10CO_2, 92CO - 8CO_2, 96CO - 4 CO_2, 98CO - 2 CO_2 are 0.137, 0.107, 0.051, 0.025 wt-% respectively. Thus the formation of hercynite is feasible, except at 2% CO_2.

Observed failures due to the chemical attack were either in the form of:

(i) reduction in stopper rod and crucible thickness

(ii) total cleavage of stopper rod whenever the melt was stirred by gas bubbling.

The reduction in the thickness of the crucible would ultimately lead to its failure since it had to withstand a pressure differential of one atmosphere.

4.5.5 SPALLING OF ALUMINA

Spalling is a tension or shear fracture of a refrac-

tory oxide resulting from any or a combination of:
(i) a temperature gradient in the material due to uneven heating or cooling that is sufficient to set up stresses of such a magnitude as to cause failure.
(ii) compression due to expansion of the material from a rise of temperature sufficient to cause shear failure or
(iii) variation in the coefficient of expansion between the surface layer and the body of the material due to slag penetration or to a structural change in service great enough to shear off the surface layer.
At the initial stage of the programme the system was lowered before the stopper rod was pulled out, and left in the same position until the metal flow was complete. The operational technique had to be changed, (section 4.2.13) when it was realised that lowering the system often resulted in tube failure.

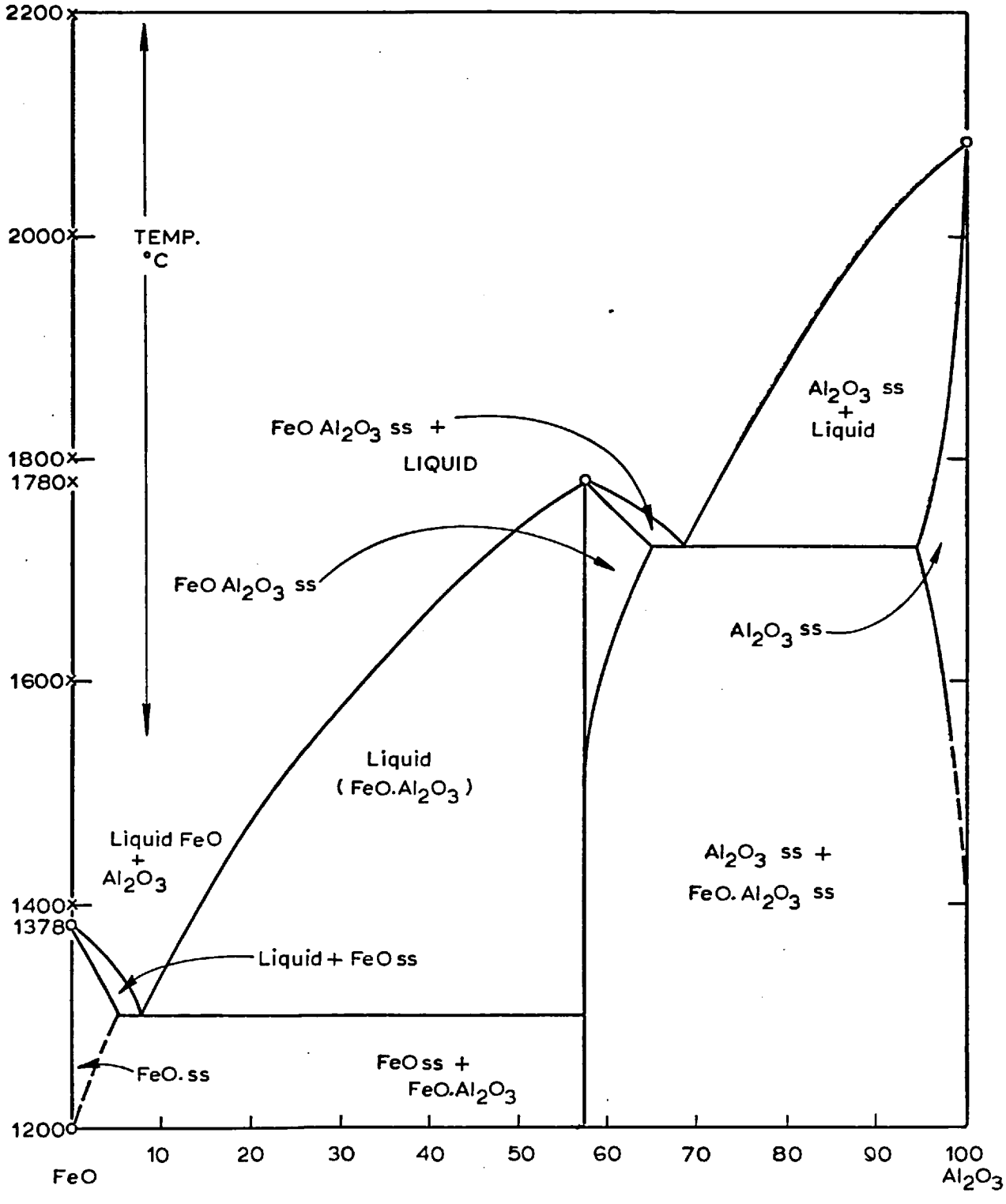

FIG.4.20 FeO - Al_2O_3 PHASE DIAGRAM (51)

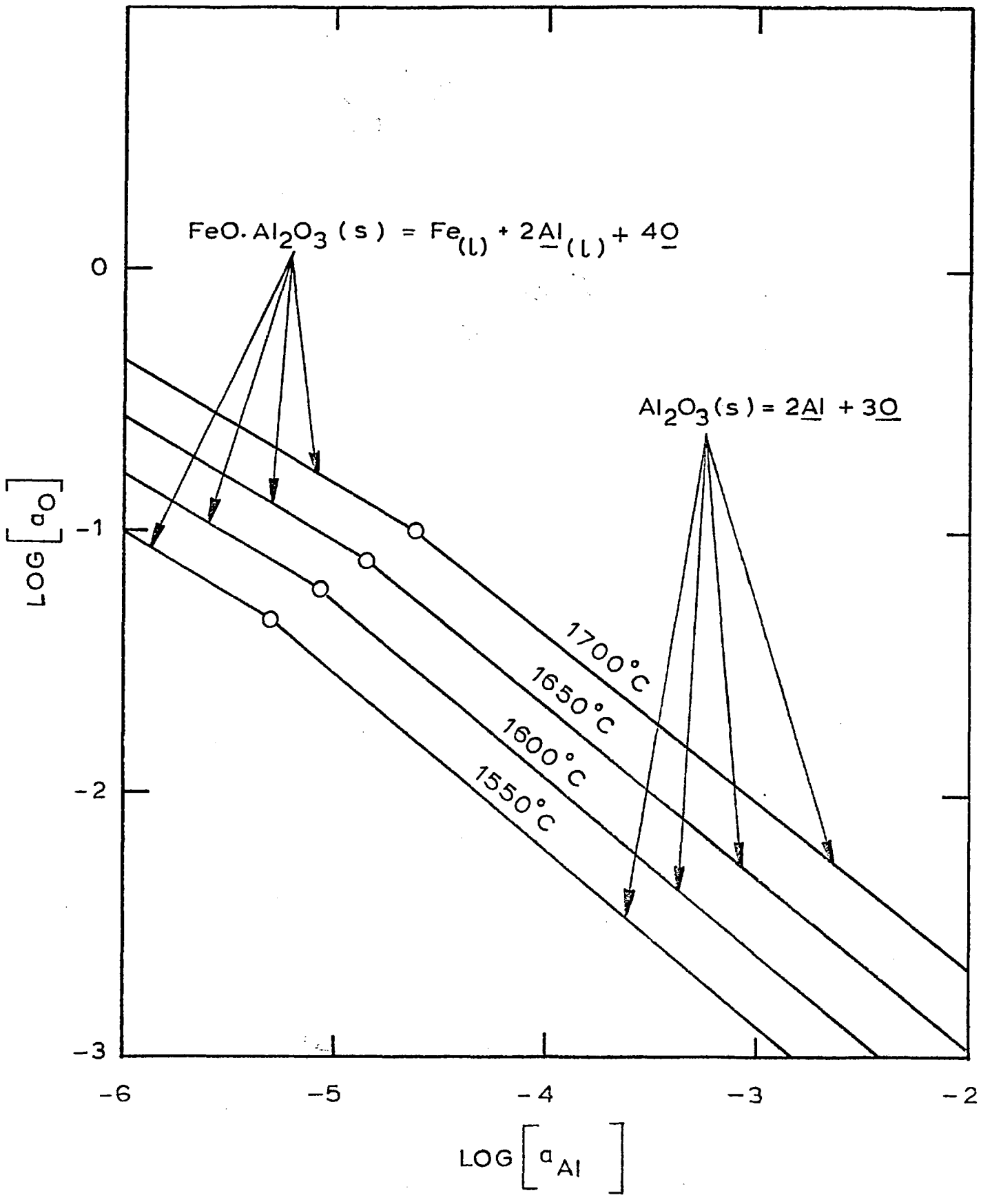

FIG.4.21 DEOXIDATION DIAGRAM FOR ALUMINIUM IN LIQUID IRON AT STEELMAKING TEMPERATURES (52)

C H A P T E R 5

RESULTS.

5.1 DISCHARGE COEFFICIENT AND MASS FLUX

5.1.1 Discharge coefficient

5.1.2 Mass flux

5.2 MAJOR SOURCES AND ESTIMATION OF ERRORS

5.3 GENERAL CLASSIFICATION

5.3.1 General

5.4 GAS SATURATED IRON STREAMS IN SHORT, SMOOTH NOZZLES

5.4.1 Discharge coefficient measurements

5.4.2 Stream appearance

5.4.3 Chamber pressure in the course of the run

5.4.4 The growth of CO, and nitrogen gas bubbles

5.5 GAS SATURATED IRON STREAMS IN LONG, SMOOTH NOZZLES

5.5.1 Introduction

5.5.2 Discharge coefficient measurements

5.5.3 Stream appearance

5.5.4 Chamber pressure in the course of the run

5.5.5 The growth of gas bubbles

5.6 GAS SATURATED IRON STREAMS IN ROUGH NOZZLES

5.6.1 Introduction

5.6.2 Discharge coefficient measurements

5.6.3 Stream appearance, chamber pressure and bubble growth

CHAPTER 5

RESULTS

5.1 DISCHARGE COEFFICIENT AND MASS FLUX

5.1.1 Discharge coefficient, C_D

$$C_D = Q_{actual}/Q_{Bernoulli} \quad \ldots\ldots\ldots \quad 5.1$$

$$Q_{actual} = C_D.a[2\Delta P_t/\rho_L(1 - \beta^4)]^{\frac{1}{2}} \quad \ldots\ldots \quad 5.2$$

where a = nozzle cross sectional area

Q = mass flow rate

A = cross sectional area of crucible

$$\beta = (a/A)^{\frac{1}{2}} \quad \ldots\ldots \quad 5.3$$

$$\Delta P_t = (P_a + \rho_L gh - P_v) \quad \ldots\ldots \quad 5.4$$

Since P_v and h vary during the run arithmetical mean values were taken to calculate C_D, hence

$$C_D \text{ (mean)} = 1.60\ M(1-\beta^4)^{\frac{1}{2}}d^{-2}(\Delta t)^{-1}\rho_L^{\frac{1}{2}}(\Delta P_t)^{-\frac{1}{2}} \quad \ldots\ldots 5.5$$

where M, d, Δt, ρ_L, are the mass of charge, diameter of nozzle, time of stream flow, and density of melt respectively.

5.1.2 Mass Flux density.

$$G_{mean} = \frac{4\ M}{\Delta t\ \pi d^2} \quad \ldots\ldots 5.6$$

$$= 1.27\ M(\Delta t)^{-1}d^{-2} \quad \ldots\ldots 5.7$$

5.2 MAJOR SOURCES AND ESTIMATION OF ERRORS

$$\text{If } Y = f(a,b,c, \ldots) \qquad \ldots\ldots 5.8$$

where a,b,c, ... are independent, the systematic uncertainty $(\Delta Y)_a$, due to the undertainty Δa in the measurement a is given by $(\Delta Y)_a$

$$(\Delta Y)_a = (\partial Y/\partial a)\,\Delta a \qquad \ldots\ldots 5.9$$

In practice two techniques are often used to obtain the overall systematic uncertainty ΔY, the first combines them by arithmetic addition, and the other in quadrature:

$$\Delta Y = \partial Y/\partial a \,.\, \Delta a + \partial Y/\partial b \,.\, \Delta b + \partial Y/\partial c \,.\, \Delta c + \ldots 5.10$$

$$(\Delta Y)^2 = (\partial Y/\partial a)^2 (\Delta a)^2 + (\partial Y/\partial b)^2 (\Delta b)^2 + \cdots\cdots \qquad \ldots\ldots 5.11$$

The technique by equ. 5.11 is likely to overestimate the size of the total systematic uncertainty, and may be considered as an estimate of the maximum possible limit whereas the second method employing equ. 5.10 tends to underestimate the uncertainty particularly when one of the components is considerably larger than the others.

Considering elemental increments in the parameters involved in equ. 5.5

$$\Delta C_D/C_D = \Delta M/M + 2\Delta d/d + \Delta t/t + \tfrac{1}{2}\Delta\rho/\rho + \tfrac{1}{2}\Delta P_t/P_t \qquad \ldots\ldots\ldots 5.12$$

$\Delta M/M$, $\Delta d/d$, $(\Delta t)/_t$, $\Delta P_t/P_t$ are 0.3, 4, 3, and 1%

respectively. Substituting these in equ. 5.12 the % error in discharge coefficient lies between 8.3 and 5.1. Similarly the percentage error in mass flux lies between 8.8 and 5.1.

For the heat-, mass transfer and mixed controlled growth of an isolated spherical bubble, neglecting the effects of liquid viscosity, inertia and surface tension, previously considered in section 3.4, for which

$$R = 2\beta(Dt)^{\frac{1}{2}} \quad \ldots\ldots\ldots\ldots \quad 3.44$$

where β = growth rate constant

R = bubble radius

D = diffusivity of the rate controlling species

t = time since bubble growth commences

$$\Delta\beta/\beta = \tfrac{1}{2}(\Delta D/D) + \tfrac{1}{2}(\Delta t/t) + (\Delta R/R) \quad \ldots\ldots\ldots \quad 5.13$$

$\Delta D/D$, $\Delta t/t$, $\Delta R/R$, are 10, 10, and 5% respectively, hence the maximum percentage error in β lies between 15 and 9.

5.3 GENERAL CLASSIFICATION

5.3.1 General.

The results are presented in five subsections in the same sequence as the experimental programme developed. All the runs were carried out at chamber pressures lower than 20 mmHg. Where the chamber pressure at the beginning

of a run was significantly lower, except in the case of degassed and nitrogen saturated iron, the chamber pressure at the end of the run increased due to gas evolution, the extent of which depended on the degree of stream disintegration. Hence the starting and finishing chamber pressures were averaged as the mean pressure for each run.

The silver and iron melts were each saturated at one atmosphere pressure and 1100, 1600°C respectively.

Two different types of nozzles were used for the experiments:

1. The 'smooth' nozzles were of thermal recrystallised alumina which were either in the form of a hole drilled at the base of the alumina crucible (short, smooth nozzles) or in the form of another thermal recrystallised narrow-bore alumina tube sintered to the base of an alumina crucible (long, smooth nozzles). In either case the length of the nozzle was the length of the parallel section of the duct.

2. The 'rough' nozzles consisted of alumina powder sintered to the base of an alumina crucible bearing a hole of equal nominal diameter as that formed through the sintered cement. Since, in general, the length of

the short, smooth component was much less ($\sim$ 4 mm) than that of the rough nozzle ($\sim$20mm), the length of the sintered section was always taken as the overall length of the rough nozzle.

5.3.2 Classification of the results.

Five broad classifications will be employed:

1. Gas-saturated iron streams in short, smooth nozzles.
2. Gas-saturated iron streams in long, smooth nozzles.
3. Gas-saturated iron streams in rough nozzles.
4. Air- and oxygen-saturated silver streams in both smooth and rough nozzles.
5. Degassed silver and iron streams in rough and smooth nozzles.

5.4. GAS SATURATED IRON STREAMS IN SHORT, SMOOTH NOZZLES.

5.4.1 Discharge coefficient measurements.

The discharge coefficient data are presented in table 5.1. Their values lie between 0.49 and 0.74.

Those obtained for the nitrogen series are higher than for the CO-CO_2 and hydrogen-saturated iron streams.

Run. No.	Gas Solute	Nozzle diameter (mm)	l/d	Mean discharge coefficient C_D
A33	H_2	1.49	2.44	0.69
P4	"	1.54	2.01	0.56
B5	$92CO-8CO_2$	1.60	2.3	0.51
B8	"	1.60	3.3	0.56
B9	"	1.60	1.89	0.51
C10	$96CO-4CO_2$	1.60	2.58	0.57
C5	"	1.60	1.86	0.53
B4	"	1.50	3.0	0.49
B15	"	1.60	2.34	0.51
A29	N_2	1.70	2.85	0.73
A30	"	1.42	3.38	0.72
C9*	"	1.62	3.39	0.74

Table 5.1

* 0.1 wt-% S added.

DATA ON GAS-SATURATED IRON STREAMS IN SHORT, SMOOTH NOZZLES.

5.4.2 Stream appearance.

No stream break-up was obtained for either the nitrogen- or hydrogen-saturated iron streams. The addition of sulphur up to 0.1 wt-% did not alter the stream behaviour.

There were, however, occasional isolated bubble appearances, the diameter of which typically varied between 10 mm and 22 mm. In general, the streams exhibited 'Rayleigh' type of break-up.

Fig. 5.6 illustrates the typical behaviour of nitrogen- and hydrogen-saturated iron.

In the case of the $96CO\text{-}4CO_2$, $92CO\text{-}8CO_2$ saturated iron streams, homogeneous, bubbly flow was obtained and this is illustrated by Fig. 5.2.

5.4.3 Chamber pressure in the course of the run.

The chamber pressure rise during the run resulted from gas evolution during

(a) stream disintegration

(b) splashing in the collector and

(c) solidification.

Figs. 5.3 and 5.4 are the typical curves experimentally

obtained for nitrogen, and CO-CO_2 saturated iron streams respectively.

5.4.4 The Growth of Carbon Monoxide and Nitrogen Gas Bubbles.

The growth of typical carbon monoxide and nitrogen bubbles was analysed. Fig. 5.5, and 5.6 show the sequence of growth of nitrogen and carbon monoxide bubbles.

Figs. 5.7 and 5.8 are the corresponding curves obtained by plotting the bubble diameter against the square root of the life of the bubbles. Time zero was arbitrarily assigned to the time the bubble first became visible [$2R_o \sim$ stream diameter] and it should be appreciated that the growth of the bubble must have commenced earlier than assumed.

The growth constant, β of carbon monoxide was found higher than for nitrogen bubbles.

5.5 GAS SATURATED IRON STREAMS IN LONG, SMOOTH NOZZLES.

5.5.1 Introduction

Since the stream breakup in the short, smooth nozzles was limited it was presumed that increasing the contact area between the nozzle and metal stream might significantly affect the stream behaviour and hence runs were carried out in longer, smooth nozzles.

FIG. 5.1

(a) Degassed iron stream. Run P6.

(b) Nitrogen saturated iron stream. Run P3.

(c) An example of 'Warner's stream'; although apparently breaking up, the origin of which could be fluid dynamic effects, heterogeneous nucleation within the nozzle or Rayleigh breakup.

Run B4.
Fe-C-O stream exhibiting homogeneous bubbly flow.

FIG. 5.2

FIG.5.1

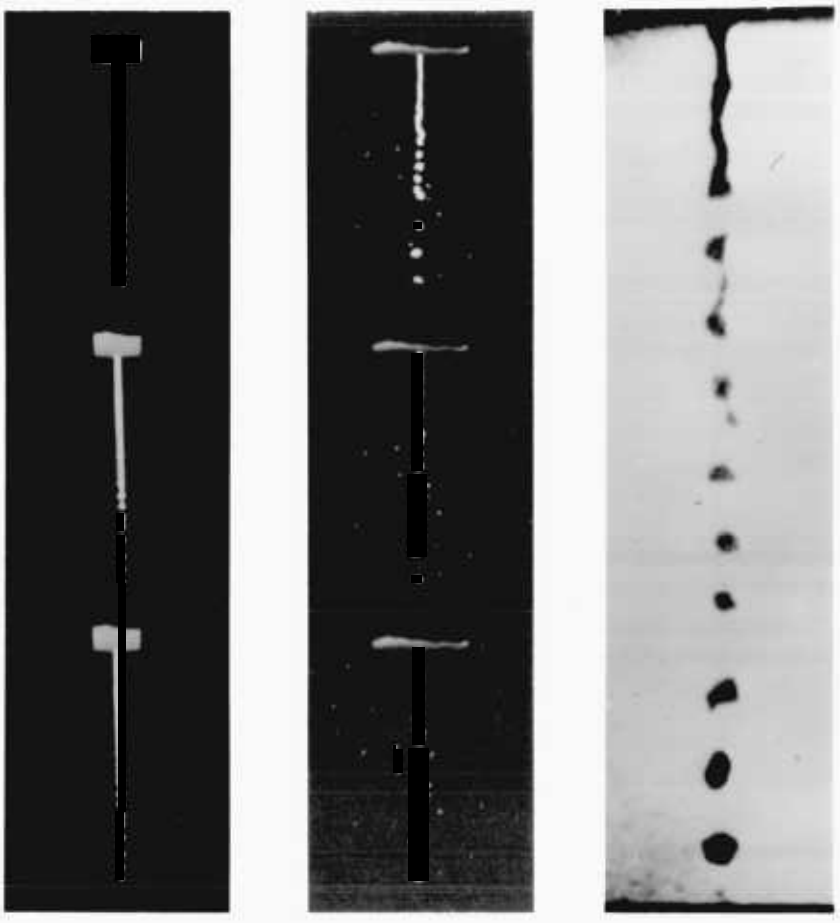

(a) (b) (c)

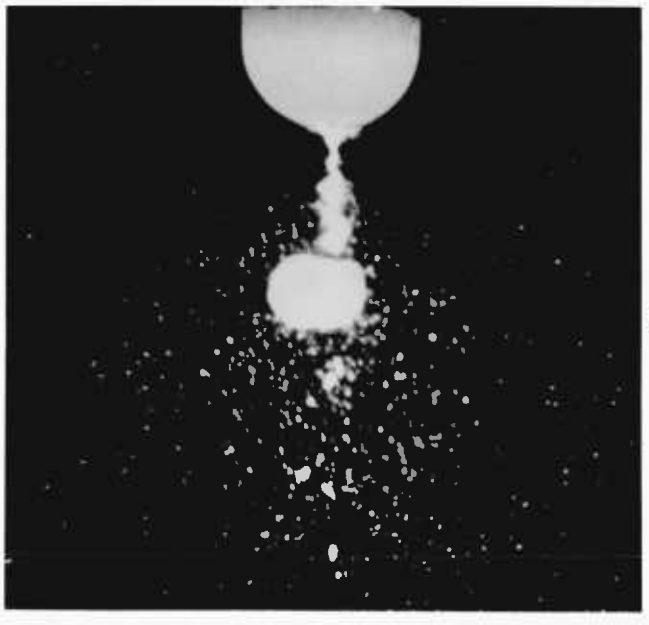

FIG.5.2

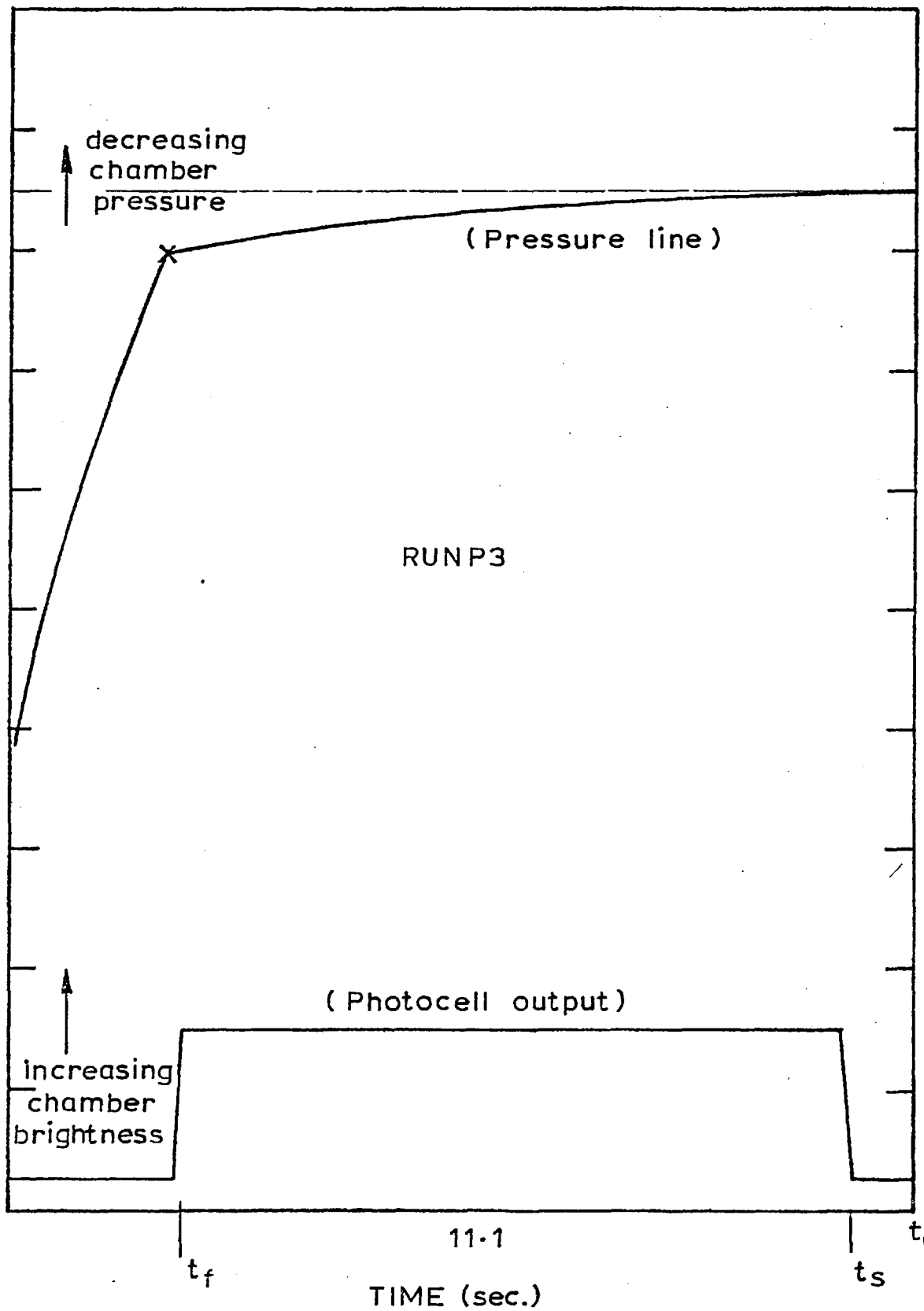

FIG.5.3 TYPICAL CHAMBER PRESSURE-TIME CURVE FOR Fe-N STREAM FLOWING THROUGH ROUGH ALUMINA NOZZLES

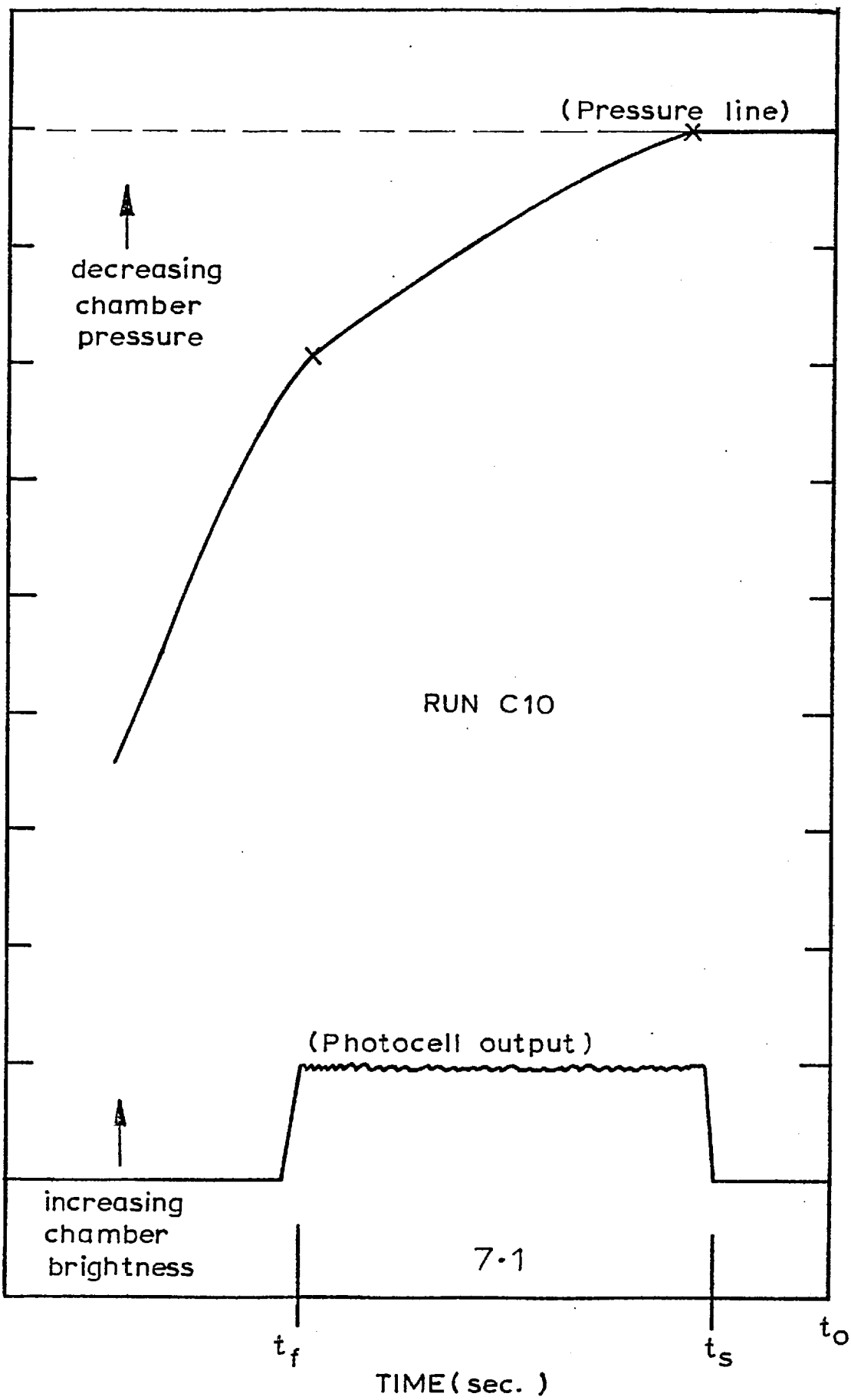

FIG.5.4 TYPICAL CHAMBER PRESSURE-TIME CURVE FOR Fe-C-O STREAMS FLOWING THROUGH SMOOTH ALUMINA NOZZLES

FIG. 5.5

KINETICS OF CARBON MONOXIDE BUBBLE GROWTH IN IRON AT 1600°C, 20 mmHg.

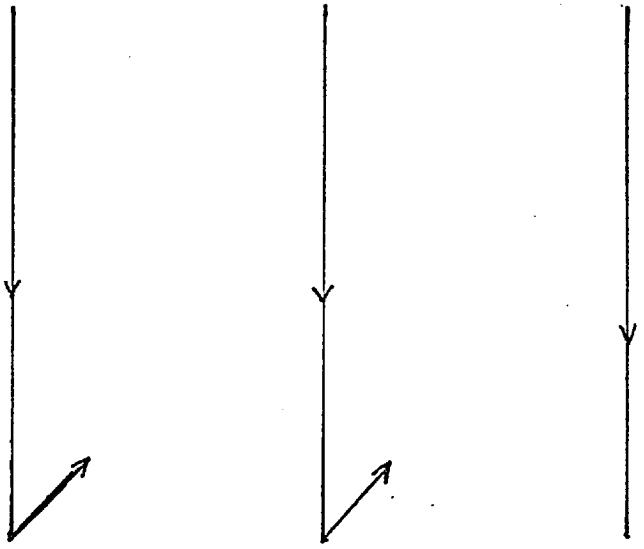

The arrows indicate the direction of the sequence of bubble growth.

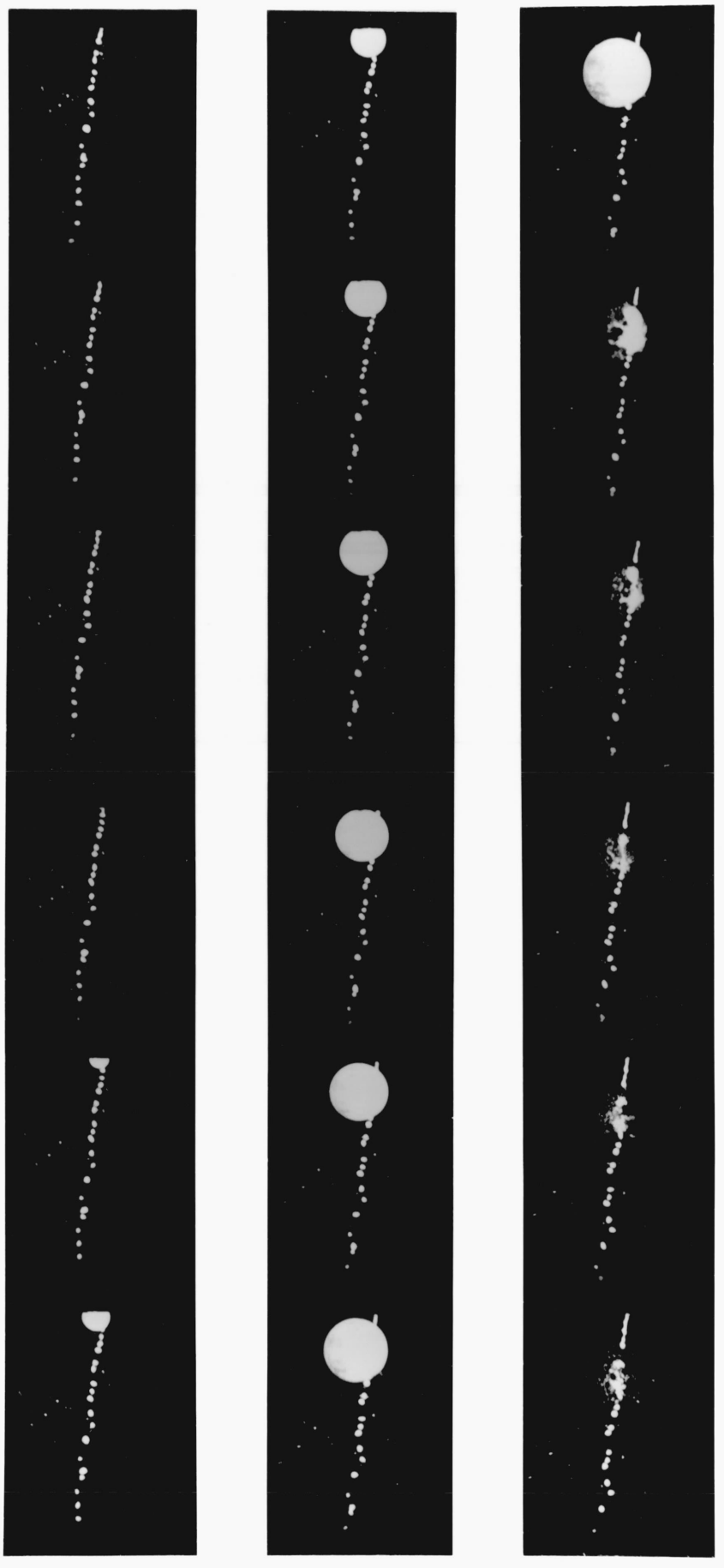

FIG. 5.5

FIG. 5.6

KINETICS OF NITROGEN BUBBLE GROWTH IN IRON AT 1600°C
20 mmHg.

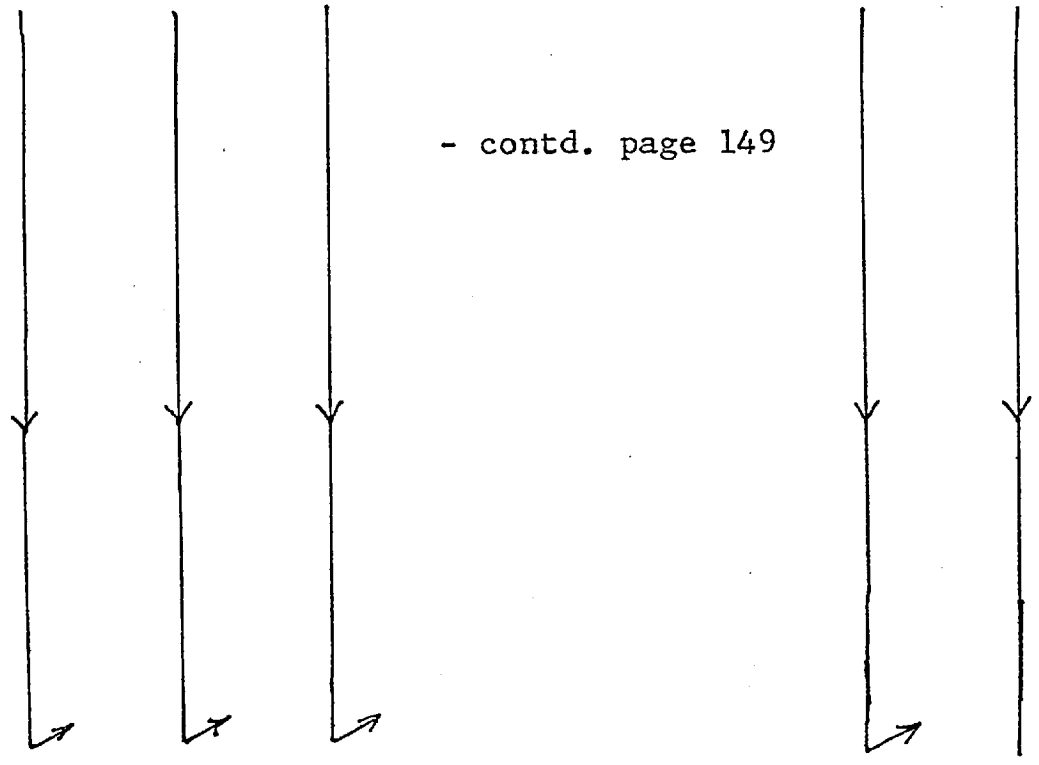

- contd. page 149

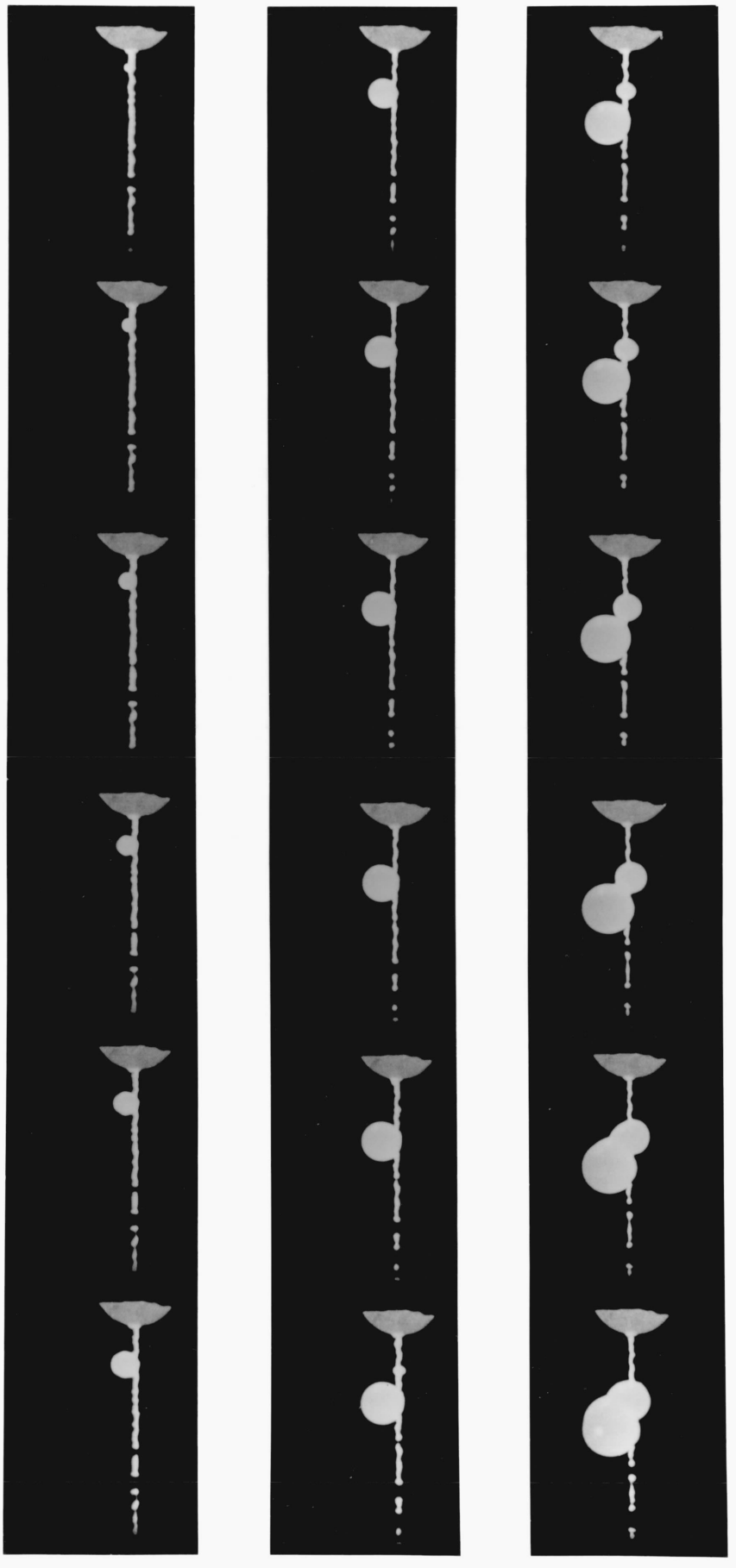

FIG. 5.6 contd. pp.149

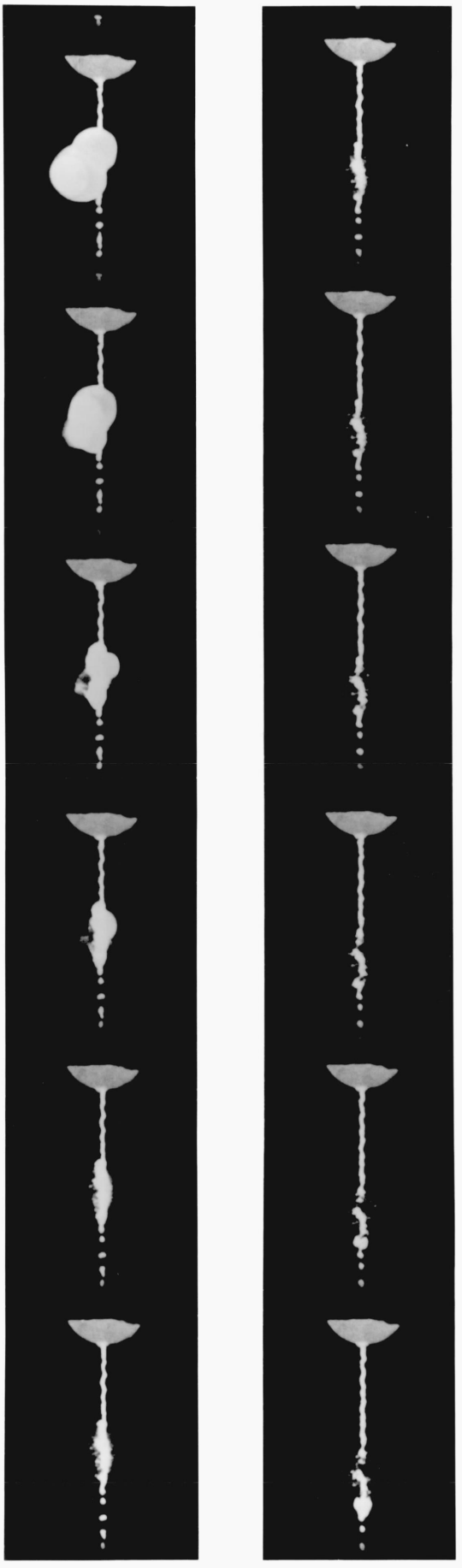

FIG. 5.6 contd.

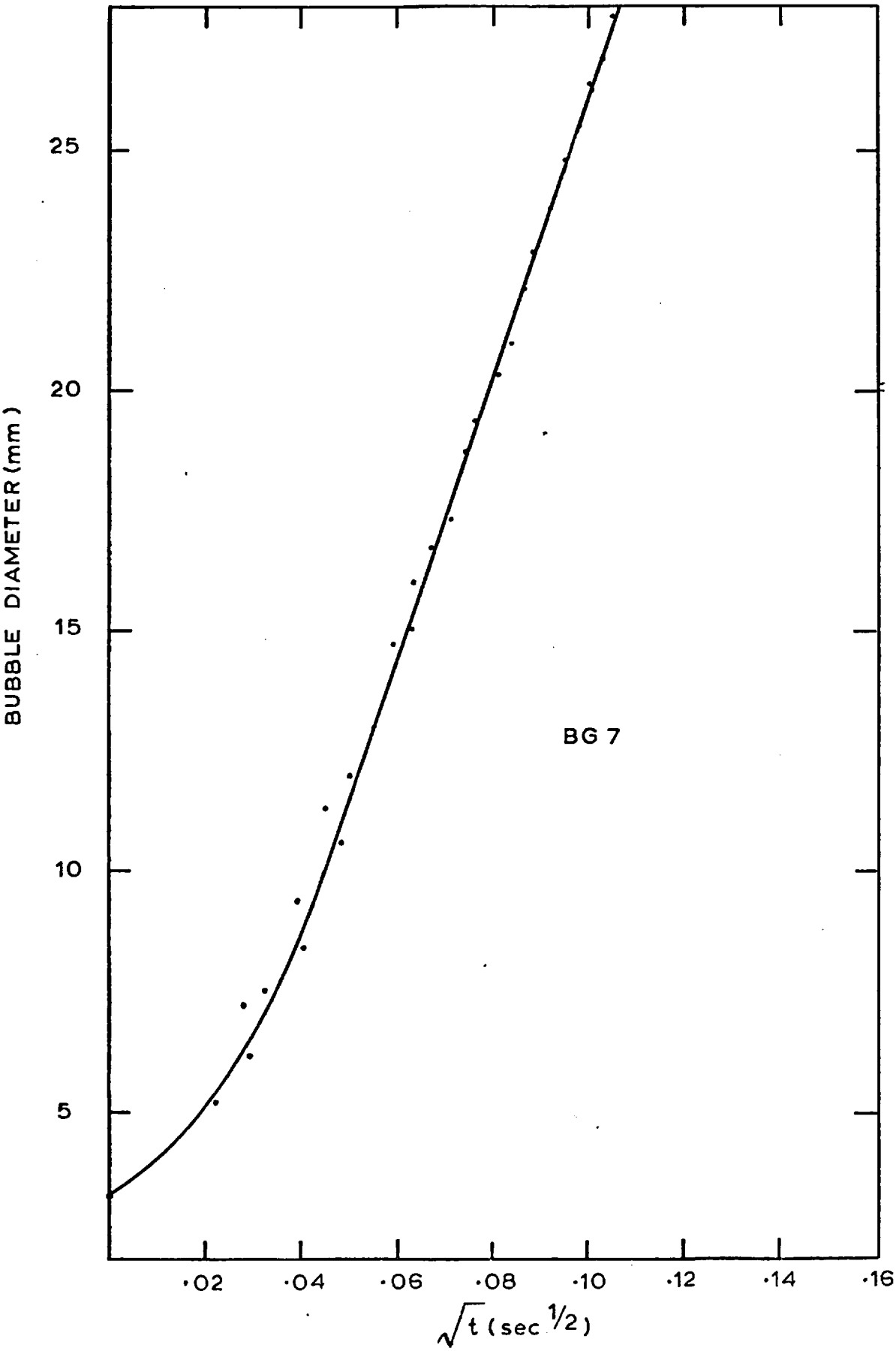

FIG.5.7 CARBON MONOXIDE BUBBLE GROWTH (EARLY RETARDATION)

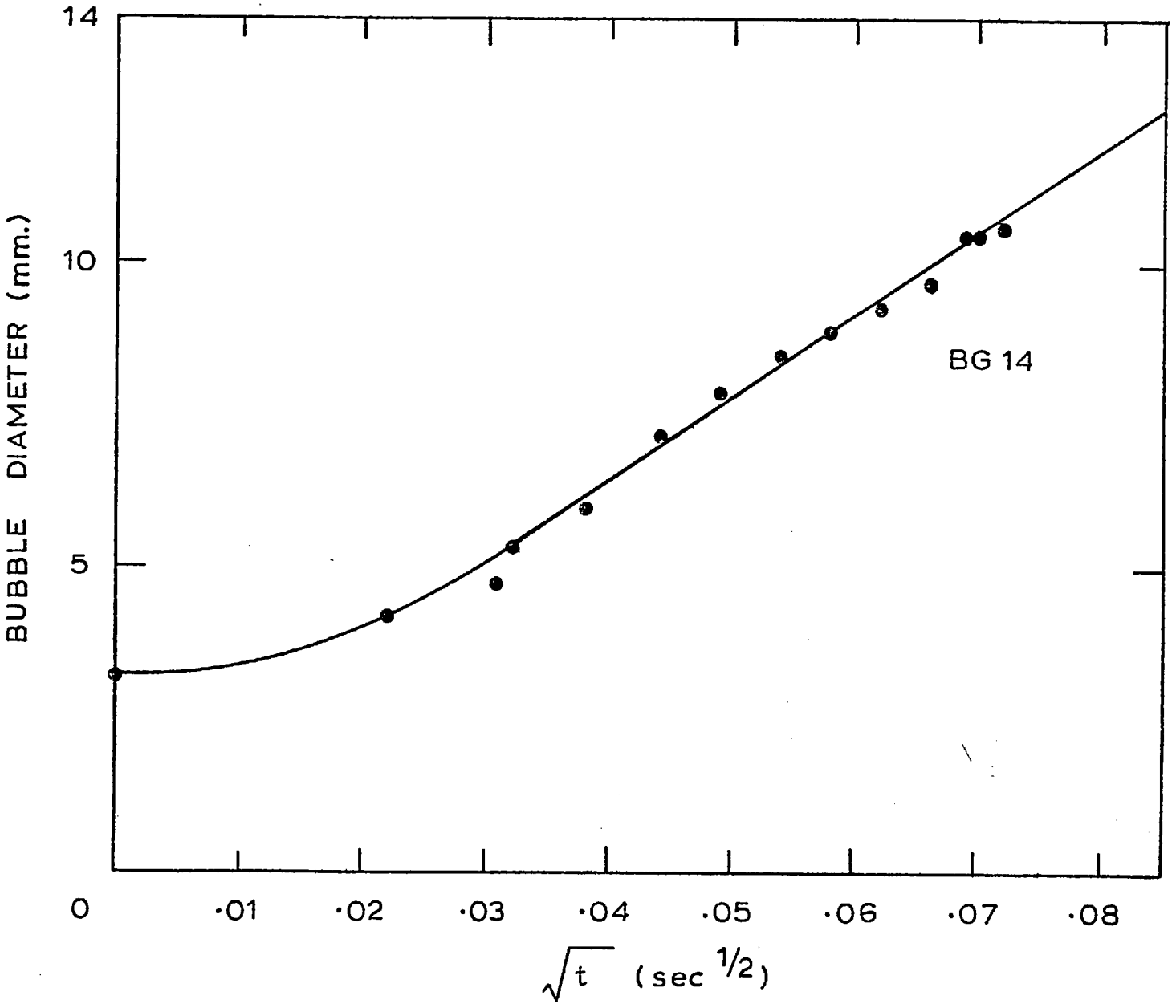

FIG.5.8 NITROGEN BUBBLE GROWTH (EARLY RETARDATION)

5.5.2 Discharge Coefficient Measurements.

Run No.	Gas Solute	Nozzle diameter (mm)	l/d	Mean discharge coefficient, C_D.
D3	H_2	1.50	9.06	0.63
E2	"	"	8.9	0.59
E3	"	"	7.68	0.59
$ST_{LSN}9$	96CO-4CO_2	"	7.03	0.50
$ST_{LSN}7$	"	"	7.85	0.51
$ST_{LSN}17$	"	"	7.33	0.45
$ST_{LSN}14$	"	"	6.39	0.57

TABLE 5.2

DATA ON GAS-SATURATED IRON STREAMS IN LONG, SMOOTH NOZZLES

The discharge coefficient data for gas-saturated iron in long, smooth nozzles are presented in Table 5.2. In general these are lower than those obtained for the same system in short, smooth nozzles.

Here again, those obtained for the hydrogen series are in general higher than for the CO-CO_2 series; the discharge coefficient decreases as the l/d ratio increases for a particular system.

5.5.3 Stream Appearance.

The pattern of break-up obtained with the CO-CO_2

series is the same as that obtained with the short, smooth nozzles. There was no significant difference in the stream appearance.

The hydrogen series showed greater break-up than obtained with the short, smooth nozzles. A typical stream behaviour is illustrated with Fig. 6.3.a .

The nitrogen saturated iron streams did not break up; nor did the addition of 0.1 wt-% sulphur alter the stream behaviour. In general, the stream behaviour was the same as obtained with the short, smooth nozzles - exhibiting only Rayleigh break-up.

5.5.4 Chamber pressure in the course of the run.

The recorded chamber pressures for the hydrogen series confirmed greater gas evolution in the course of the run than obtained with similar but shorter nozzles.

The pattern for the nitrogen and CO-CO_2 series are the same as with shorter nozzles.

5.5.5 The growth of gas bubbles.

The growth of the typical, isolated CO, N_2 gas bubbles showed the same pattern as for the short, smooth nozzles. However, the hydrogen bubbles were very short-lived, with typical maximum life of 0.001 sec. and below.

5.6 GAS SATURATED IRON IN ROUGH NOZZLES.

Since the nitrogen-saturated iron did not break up and the break-up of the hydrogen series in long, smooth nozzles was limited, it was decided to carry out some runs in rough nozzles.

The measured discharge coefficients were significantly lower than obtained for the runs carried out in smooth nozzles of both categories. Here again, those obtained for the hydrogen series were again lower than the corresponding values obtained for the nitrogen series.

5.6.2 Discharge coefficient measurements

Run No.	Gas Solute —	Nozzle diameter (mm)	l/d —	Mean discharge coefficient, C_D
G2	H_2	1.8	5.0	0.34
G3	"	1.8	"	0.35
G5	"	"	"	0.33
P5	"	1.62	3.3	0.30
G11	N_2	2.42	5.8	0.45
E4	"	1.84	5.9	0.41
G1	"	1.80	5.0	0.39
P3	"	1.60	6.0	0.39
G6	$10\%H_2$-$90\%N_2$	1.80	5.0	0.49
G12	"	2.62	6.3	0.42

Table 5.3

DATA ON GAS-SATURATED IRON STREAMS IN ROUGH NOZZLES.

5.6.3 Stream appearance, chamber pressure and bubble growth.

There was extensive break-up with the hydrogen-saturated iron streams in rough nozzles. Up to 80% of the stream was collected, in the form of fine powder with average particle size of about 250 microns, outside the plumbago collector located directly below the nozzle orifice.

No hydrogen bubbles were visible outside the nozzle exit as these completely collapsed at the nozzle exit. Figs. 6.3 (b) and 5.11(a) illustrate the typical stream behaviour and chamber pressure respectively during the run of hydrogen-saturated iron flowing through a rough nozzle.

The behaviour of the nitrogen series was essentially the same as with smooth nozzles since the stream exhibited mainly Rayleigh break-up. The very low discharge coefficients were not associated with a homogeneous bubbly flow in this case.

The occasional, isolated nitrogen bubbles showed the same pattern of growth rate as obtained with the smooth nozzles.

5.7 AIR AND OXYGEN SATURATED SILVER STREAMS IN ROUGH AND SMOOTH NOZZLES.

5.7.1 Introduction.

The discharge coefficient obtained by Mizoguchi for silver streams flowing through Nimonic 75 nozzles at chamber pressures of the order of 11 mmHg and below, were in the range 0.900 and 0.875 for air-saturated silver streams (with 3/16" dia. ½" long nozzle) and between 0.711 and 0.705 for oxygen-saturated silver streams (with 3/32" dia. ½" long nozzle).

The former exhibited intermittent bubble growth while the latter showed homogeneous, bubbly, choked flow.

Measured discharge coefficients in rough nozzles for nitrogen-saturated iron were as low as 0.39 and yet the stream appearance revealed no break-up, suggesting that the contributions of the entry loss and friction coefficients to the measured discharge coefficients were large. Auxiliary experiments involving air- and oxygen-saturated silver streams, flowing through both smooth and rough alumina nozzles, were planned as these would permit a realistic comparative evaluation of the friction coefficients for silver flowing through both alumina and Nimonic 75.

5.7.2 Discharge coefficient measurements.

The data on discharge coefficients for both the air- and oxygen-saturated silver streams are given in Tables 5.4 - 5.7 inclusive. The C_D values are lower than obtained for the runs carried out in Nimonic 75; similarly the values for saturated silver in rough nozzles are generally lower than obtained with the same system in smooth nozzles - the same pattern as obtained with the gas-saturated iron streams.

The growth of gas bubbles was analysed. These bubbles were rather unstable and irregular in shape (not spherical).

The stream behaviour was the same as obtained with the Nimonic 75 nozzles, (Fig. 5.11 b, c).

Run No.	Nozzle diameter (mm)	l/d	Mean discharge coefficient, C_D
SA11	1.5	13.68	0.77
SA16	2.05	1.62	0.79
SA13	1.5	11.63	0.77

Table 5.4

DATA ON AIR-SATURATED SILVER IN SMOOTH NOZZLES.

Run No.	Nozzle diameter (mm)	$\frac{l}{d}$ —	Mean discharge coefficient, $\bar{C}_D$ —
SA1	1.803	10.47	0.61
SA2	1.803	10.47	0.62
SA8	2.09	10.47	0.64

TABLE 5.5

DATA ON AIR-SATURATED SILVER IN ROUGH NOZZLES.

Run No.	Nozzle diameter (mm)	$\frac{l}{d}$ —	Mean discharge coefficient, $\bar{C}_D$ —
SA10	1.5	13.68	0.51
SA14	2.05	1.62	0.60
SA18	1.5	7.67	0.63
SA20	1.5	14.93	0.50
SA22	1.5	14.93	0.54
SA26	1.5	8.52	0.60
SA27	1.5	8.52	0.58
SA35	1.5	11.63	0.55

TABLE 5.6

DATA ON OXYGEN-SATURATED SILVER IN SMOOTH NOZZLES.

Run No.	Nozzle diameter (mm)	l/d	Mean discharge coefficient, C_d
SA3	1.803	10.47	0.41
SA7	2.09	9.56	0.43
SA29	2.19	4.84	0.54
SA30	2.19	4.84	0.54

TABLE 5.7

DATA ON OXYGEN-SATURATED SILVER IN ROUGH NOZZLES.

5.8 DEGASSED SILVER AND IRON STREAMS IN SMOOTH AND ROUGH NOZZLES

5.8.1 Introduction.

Because of the need to evaluate the entry loss coefficient the need arose to carry out some experiments with degassed silver and iron streams.

In the limit of the nozzle length tending to zero, the measured discharge coefficient would be a function of the entry loss coefficient only.

5.8.2 Discharge Coefficient Measurements

Because the alumina nozzles must have varied slightly depending on the individual characteristics of the bond at the alumina tube/ nozzle joint, the exact nature of the chamfered nozzle entry and other properties of the nozzle, it was considered not worthwhile trying high re-

producibility in discharge coefficient measurements. In fact, the values are quite consistent in view of the inevitable variation in nozzle 'quality'.

The measured discharge coefficients for degassed silver in smooth nozzles lie between 0.90 and 0.80 while those obtained for degassed iron lie between 0.80 and 0.75 in similar nozzles. Those obtained for silver in Nimonic 75 nozzles were 0.915 and 0.866 for the 3/16" dia. ½" long; 3/32" dia. ½" long respectively. The discharge coefficient measurements are again lower in rough than smooth alumina nozzles.

5.8.3 Stream appearance.

Close examination of the streams showed no flow separation. A typical stream appearance is shown in Fig. 5.1(a).

Run No.	Nozzle diameter (mm)	$\frac{1}{d}$	Mean discharge coefficient C_D
SA17	2.05	1.62	0.89
SA23	1.5	10.26	0.83
SA24	"	"	0.85
SA32	"	11.63	0.80
SA34	"	"	0.81

Table 5.8

DATA ON DEGASSED SILVER IN SMOOTH NOZZLES.

Run No.	Nozzle diameter (mm)	l/d —	Mean discharge coefficient, C_D —
SA4	1.8	10.47	0.73
SA9	2.09	9.56	0.69

TABLE 5.9

DATA ON DEGASSED SILVER IN ROUGH NOZZLES.

Run No.	Nozzle diameter (mm)	l/d —	Mean discharge coefficient, C_D —
G9	1.6	2.23	0.76
B12	1.58	2.2	0.77
C3	1.62	2.3	0.79

TABLE 5.10

DATA ON DEGASSED IRON IN SMOOTH NOZZLES.

Run No.	Nozzle diameter (mm)	l/d —	Mean discharge coefficient, C_D —
G10	2.47	6.7	0.48
P6	1.76	3.32	0.53

TABLE 5.11

DATA ON DEGASSED IRON IN ROUGH NOZZLES .

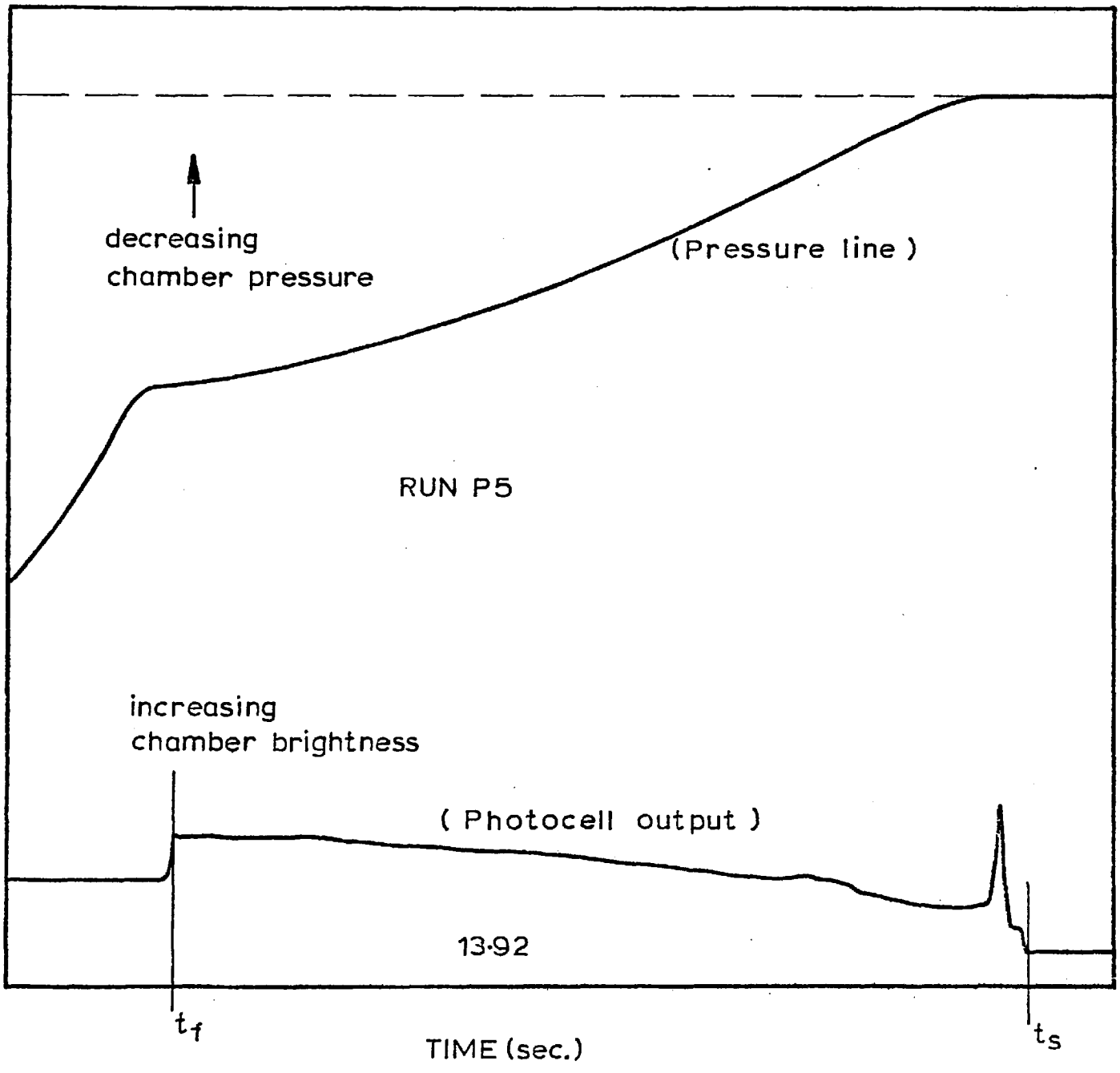

FIG. 5.11a TYPICAL CHAMBER PRESSURE-TIME CURVE FOR Fe-H STREAMS FLOWING THROUGH ROUGH ALUMINA NOZZLES

AIR SATURATED SILVER STREAM FLOWING THROUGH NIMONIC 75 NOZZLE 10 mmHg (AFTER MIZOGUCHI).

FIG. 5.11(b)

OXYGEN SATURATED SILVER FLOWING THROUGH NIMONIC 75 NOZZLE 100 mmHg (AFTER MIZOGUCHI)

FIG. 5.11(c)

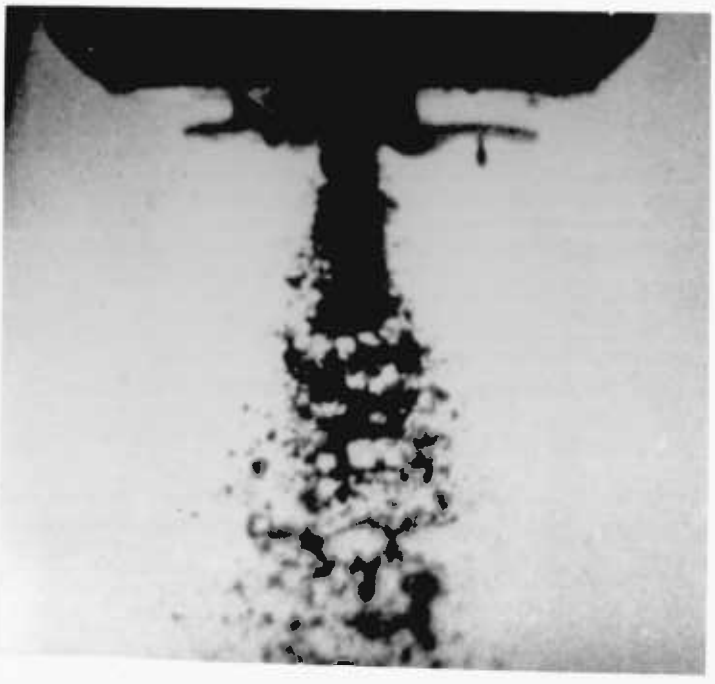

5.9 GENERAL REVIEW OF RESULTS

Degassed Iron Streams.

Analysis of the metal streams on cine films showed no flow separation. The streams exhibited Rayleigh break-up downstream. Measured discharge coefficients are rather low, ranging between 0.79 and 0.76 for iron streams flowing through short smooth alumina nozzles, and of the order of 0.50 in sintered alumina powder nozzles.

Nitrogen Saturated Iron Streams.

Nitrogen-saturated iron streams showed no break-up in both smooth and rough alumina nozzles. Although there was intermittent bubble nucleation, the break-up was essentially the Rayleigh type - the same exhibited by degassed iron streams.

Measured discharge coefficients were of the order of 0.39, and 0.73 in rough and smooth nozzles respectively. The addition of sulphur up to 0.1 wt-% did not affect the stream behaviour.

Hydrogen Saturated Iron Streams.

Hydrogen-saturated iron streams showed limited break-up when flowing through short, smooth alumina nozzles; the intensity of break-up increased with l/d of the nozzles. The break up became rigorous in rough nozzles.

Measured discharge coefficients were of the order of 0.33 and 0.60 in rough and smooth nozzles respectively.

CO-CO_2-saturated iron streams.

Both $96CO$-$4CO_2$ and $92CO$-$8CO_2$-saturated iron streams exhibited homogeneous bubbly flow when flowing through both smooth and rough alumina nozzles.

Growth of carbon monoxide and nitrogen bubbles.

The growth constants obtained experimentally for carbon monoxide and nitrogen bubbles were

888 ± 133, 448 ± 67 respectively.

C H A P T E R 6

DISCUSSION OF RESULTS.

CHAPTER 6

DISCUSSION OF RESULTS.

6.6.4 Discussion

6.6.5 Conclusion

CHAPTER 6

DISCUSSION OF RESULTS.

6.1 INTRODUCTION.

The main objective of the experimental programme was to examine the factors leading to good stream break-up, using molten iron containing different gases dissolved at 1 atmosphere pressure and flowing through either rough or smooth nozzles. In the stream degassing process degassing normally takes place in three distinct steps.

1. The gas evolved resulting from the spontaneous formation of gas bubbles within the nozzle.
2. Stream break-up downstream due to the subsequent growth and collapse of the gas bubbles that were nucleated either previously as in step 1, or downstream.
3. Subsequent degassing once the stream is in the receiver in the chamber.

Step 3 will invariably take place to an extent and at a rate depending on the efficiency of step 2. The second step is the most important in an efficient stream degassing process and the measurement of the size distribution of the resulting metal droplets following the stream disintegration may be taken as an index of the process efficiency.

Experimental work was not carried out at a sufficiently wide chamber pressure range to prove the existence of choking absolutely unequivocally, however the observed

sudden expansion of the stream outside the nozzle exit may be taken as confirming choking under a particular set of conditions. This then permits the use of theories applicable to two-phase choked flow.

The results emanating from this investigation, presented in Chapter 5, will now be reviewed to show that:

1. Gas bubbles can be nucleated on the nozzle wall under certain conditions and that nozzle roughness is not the sole overriding factor for rapid bubble nucleation.
2. The important factors influencing stream break-up include:
   (a) gas content in iron
   (b) nozzle wall roughness
   (c) diffusivity of the dissolved species
   (d) the nature and amount of adsorbed molecules on the melt surface.

In the rest of the chapter the approach used for analysing the results is first presented and the special features of the nozzles used are once again briefly summarised. For the sake of continuity the results are analysed, assessed and correlated with relevant previous work at the same time.

6.2 ANALYSIS OF RESULTS

6.2.1 Pressure drop due to bubble growth and friction in a nozzle.

Mizoguchi (7) showed that the mass flow per unit time, per unit area of nozzle (G) for a homogeneous bubbly flow is given by the equation:

$$\Delta P_t = (G^2/2\rho_L)(1 + K_L + 4C_{fm}\, l/d + 2\delta_e) \quad .. \quad 6.1$$

where ΔP_t = total pressure drop

$= (P_a + \rho_L gh - P_v)$

K_L = entry loss coefficient

C_{fm} = mean friction coefficient

δ_e = ratio of gas to liquid volume in the stream at the nozzle exit.

For flow which is not choked $P_e = P_v$ and equation 6.1 therefore yields:

$$1/C_D^2 = 1 + K_L + 4C_{fm}\, l/d + 2\delta_e \quad ..... \quad 6.2$$

If no bubble growth occurs $\delta_e = 0$ and values of C_D can be used to calculate $(K_L + 4C_{fm}\, l/d)$. Experiments with different nozzle l/d ratios allow estimation of K_L and C_{fm} separately; similarly as l/d tends to zero for a degassed stream C_D values give K_L.

When bubble growth occurs the value of C_D can be used

to estimate δ_e provided K_L and C_{fm} are known. For a flow which is choked at the exit

$$P^*_e = G^{*2} \delta^*_e / k^2 \rho_L \quad \ldots\ldots\ldots 6.3$$

and $P_e \neq P_v$. Provided K_L and C_{fm} are known P^*_e and δ^*_e can be calculated from values of C_D using the following equations:

$$P_a + \rho_L gh - (1 + k^2) P^*_e = \Delta P_t \quad C_D^2 \, [1 + K_L + 4C_{fm} \, 1/d] \quad \ldots\ldots\ldots 6.4$$

and by substituting $G^{*2} = \rho_L^2 \, C_D^2 \, \left(\frac{2\Delta P_t}{\rho_L} \right)$

into equation 6.3

$$\delta^*_e = (k^2/2) \, P^*_e / C_D^2 \Delta P_t \quad \ldots\ldots\ldots 6.5$$

k is a modification factor for the effect of surface tension on the compressibility of small bubbles, and of the form:

$$k = [(1 + 2\sigma/(3P.r + 4\sigma)]^{-1/2} \quad \ldots\ldots\ldots 6.6$$

where r = radius of bubble, P = ambient pressure, σ = surface tension, and k has a value ranging between 0.82 and 1.0 for small and large $P.r/\sigma$ values respectively (56).

6.2.2 Features of the nozzles used.

Fig. 6.1 shows a diagram of a long smooth nozzle (a detailed description of the manufacturing procedure has already been given in Section 4.2.14).

The essential features that were critical to the

analysis and interpretation of the results are enumerated below.

1. The thickness of the base of the alumina crucible (i.e. the length of short, smooth nozzles) varied from one tube to another.

2. It was extremely difficult to obtain a well-rounded profile because of the difficulty of access to the inside base of the alumina tube and the need for a conical section to seal with the stopper rod.

3. In the case where a tube was used for more than one run the surface characteristics were found to have altered from the initial condition, it was necessary to widen the bore at the base of each crucible following each run to ensure that the metal stream came into contact with a clean alumina surface. The snag accompanying this was the alteration of the entry profile and the 1/d ratios. These variations would certainly have affected the results.

The accuracy of results did not permit the quantification of the effect of small changes because of the magnitude of experimental errors as already indicated in section 5.2.

4. Since another tube was sintered to the base, there could have been a flow disturbance at the base/extension interface; similarly although extreme precautions were

taken to ensure alignment, any small degree of misalignment, which could not be completely ruled out, would have affected the flow pattern.

5. Where rough nozzles were prepared the protuberances from the surface of the sintered alumina were found to be irregular. The mean height of roughness projections, e inside the nozzles varied between 0.1 and 0.3 mm. This meant that for a 2 mm diameter nozzle $e/d \sim 0.2$ which is a very high value. These values were obtained by examining the cross section typical fired rough nozzles under the microscope (Figs. 4.16 and 4.17)

6.3 EXPERIMENTAL EVALUATION OF NOZZLE ENTRY LOSS AND SKIN FRICTION.

Since the nozzles used in this work were rough and did not have a smooth rounded entry it was not possible to estimate the entry loss or friction factor from theory. The results of Nikuradse on pipe friction experiments were graphically presented by Vennard (57). This is shown in Fig. 6.2. It can be seen that C_f values of about 0.1 are to be expected for very rough pipes. Colebrook (58) obtained:

$$1/(C_f)^{\frac{1}{2}} - 2 \log(d/e) = 1.14 \quad \ldots\ldots\ldots\ldots \quad 6.7$$

so that for $d/e \sim 5$ (as obtained for our rough nozzles) $C_f \sim 0.16$. (d = pipe diameter, e = equivalent sand grain

size of the surface protuberances).

From the results on degassed iron and silver we obtain, on substitution into equation:

$$(C_D^{-2} - 1) = K_L + 4C_{fm}\,1/d \qquad \ldots\ldots\ldots 6.8$$

the following results given in table 6.1. The simultaneous equations obtained by the substitution of 1/d and C_D values which are subject to experimental errors, will not normally yield unique values of K_L, C_{fm}. Various values of C_{fm} were assumed to test the region where the most consistent values of K_L were obtained. The results for degassed silver in smooth alumina nozzles are presented in table 6.2.

Key to Fig. 6.1

1. Base thickness may vary from one tube to another.

2. Sharp entry, following the drilling of a hole through the base.

3. Chamfered, but entry not well rounded.

4. The alumina cement after firing (in situ) could project into the nozzle bore thus causing excessive entry loss.

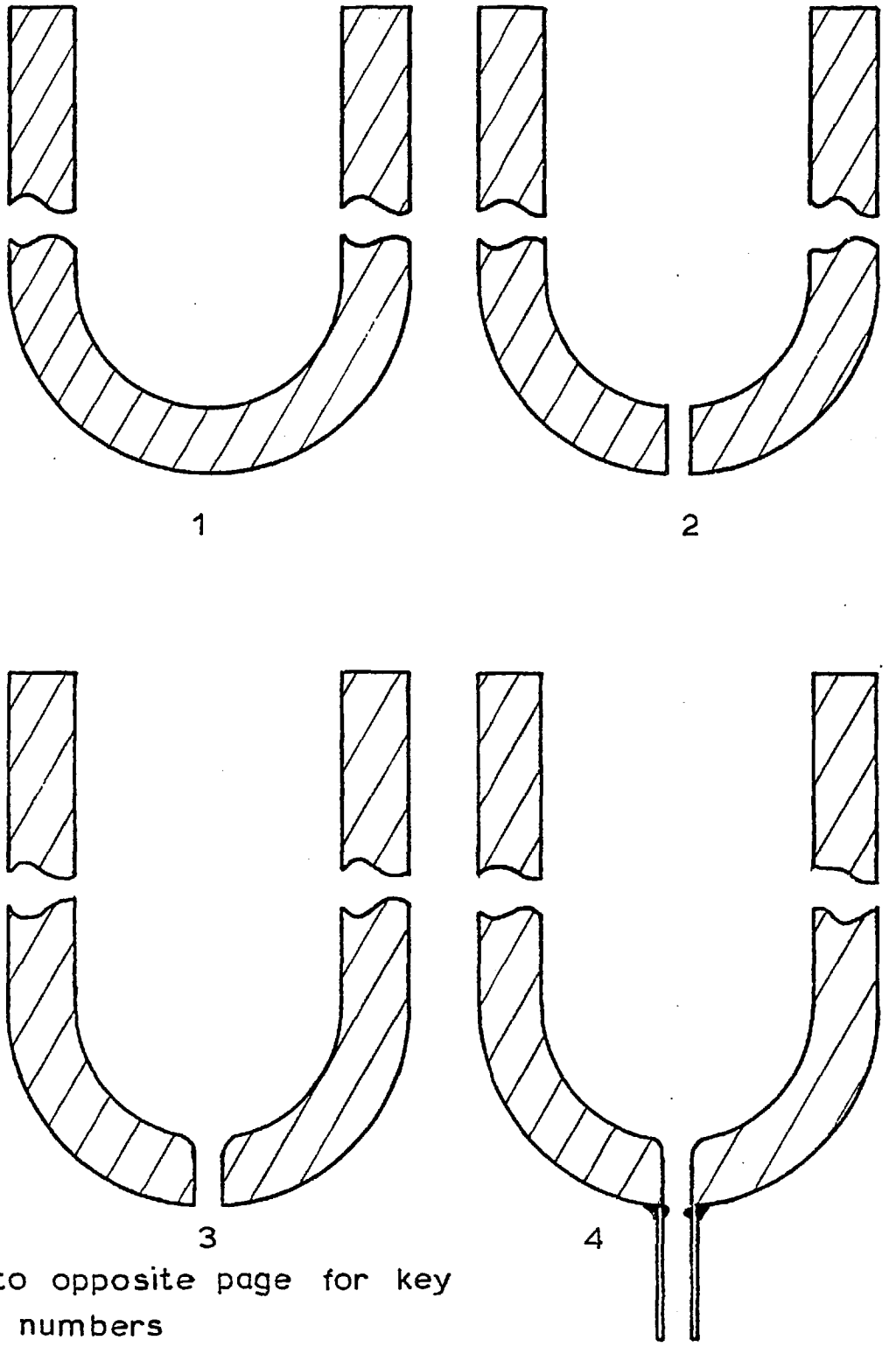

Refer to opposite page for key to numbers

FIG.6.1 SEQUENCE OF THE PREPARATION OF A LONG NOZZLE ILLUSTRATING THE ANOMALIES

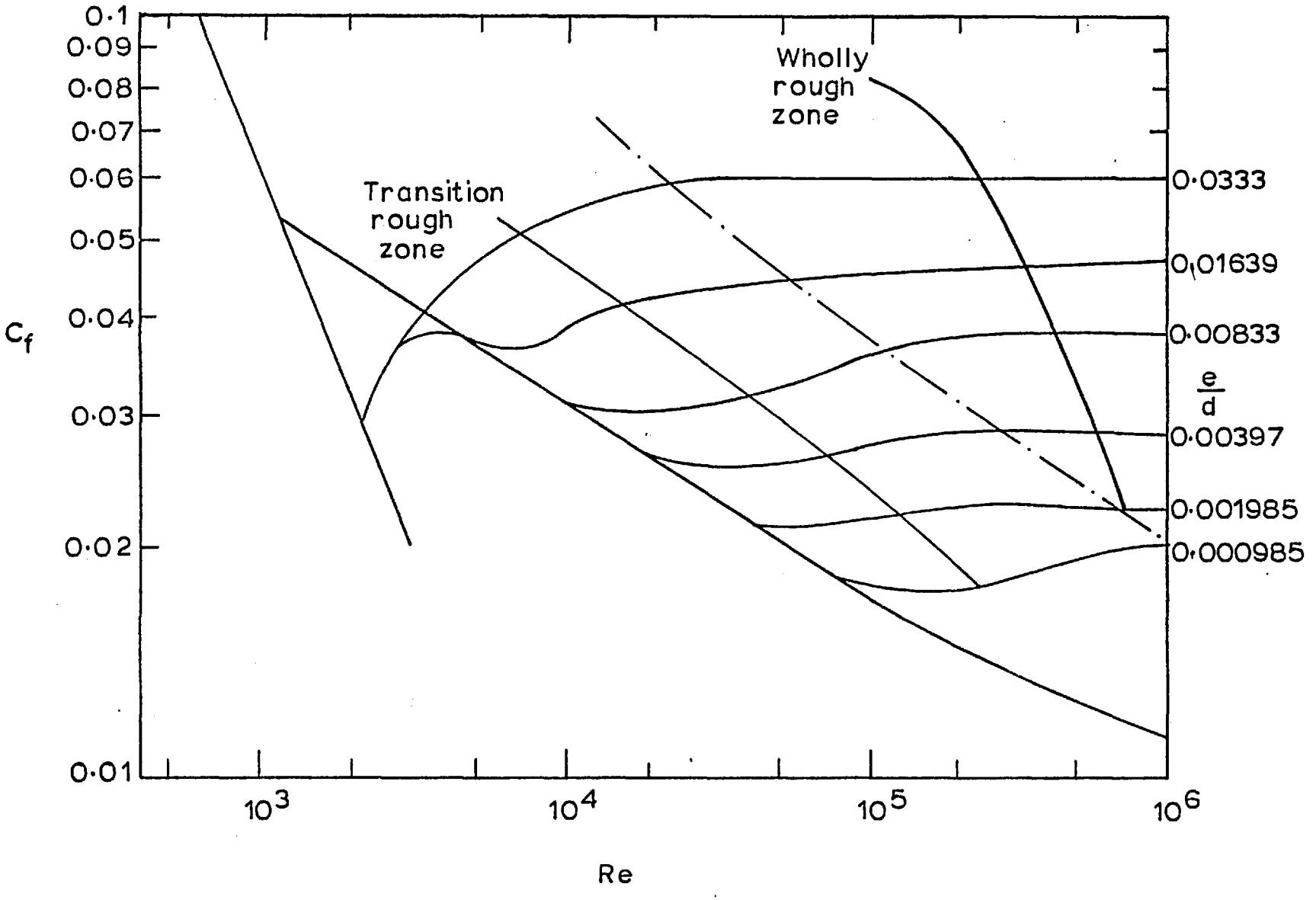

FIG.6.2 FRICTION FACTOR AGAINST REYNOLDS NUMBER WITH SURFACE ROUGHNESS AS A PARAMETER (57)

Key	Run No.	1/d	Re_3 ($\times 10^3$)	C_D	$(C_D^{-2} - 1)$
1	SA 17	1.62	23.7	0.89	0.26
	SA 23	10.26	16.09	0.83	0.45
	SA 24	10.26	16.20	0.85	0.38
	SA 32	11.63	15.52	0.80	0.56
	SA 34	11.63	15.58	0.81	0.52
2	SA 9	9.56	20.85	0.69	1.10
	SA 4	10.47	19.20	0.73	0.88
3	B 12	2.2	7.59	0.77	0.69
	G 9	2.23	7.94	0.76	0.73
	C 3	2.3	7.91	0.79	0.60
4	P 6	3.32	8.76	0.53	2.56
	G 10	6.7	9.07	0.48	3.34

Table 6.1

DATA FOR THE ESTIMATION OF K_L, C_{fm} FOR DEGASSED METAL STREAMS IN ROUGH AND SMOOTH NOZZLES.

KEY

1. Degassed silver in smooth alumina nozzles
2. " " " rough " "
3. " iron " smooth " "
4. " " " rough " "

K_L - values					
Run No. / C_{fm} assumed	SA 17	SA 23	SA 24	SA 32	SA 34
.002	.25	.37	.30	.47	.43
.004	.23	.29	.22	.37	.33
.0045	.23	.26	.20	.35	.31
.005	.23	.25	.18	.32	.29
.0055	.22	.22	.17	.29	.26
.006	.22	.20	.13	.28	.24
.01	.20	.04	-.03	.09	.05

TABLE 6.2

K_L FOR DIFFERENT C_{fm} FOR DEGASSED SILVER FLOWING THROUGH SMOOTH ALUMINA NOZZLES.

The following pattern emerges from the data presented in table 6.1.

1. For the same type of nozzle the $(C_D^{-2} - 1)$ values obtained for degassed iron are higher than for degassed silver despite the lower l/d ratios.

2. For a given system - either degassed silver or iron - the $(C_D^{-2} - 1)$ values for the rough nozzles are higher than for the smooth nozzles, because of the increased e/d ratio of the surface characteristics.

3. While l/d varied between 1.62 and 11.63 for Ag - O runs in smooth alumina the corresponding values of $(C_D^{-2}-1)$ only varied between 0.26 and 0.56 suggesting that the contribution of the skin friction factor, C_{fm} to the measured C_D values was significantly lower than the contribution of the entry loss coefficient, K_L.

Run No.	1/d	Re_3 ($\times 10^3$)	C_D	$(C_D^{-2} - 1)$
B 12	2.2	7.59	0.77	.69
C 3	2.3	7.91	0.79	.60
G 9	2.23	7.94	0.76	.73
A 29	2.85	7.82	0.73	.88
A 30	3.38	6.33	0.72	.93
C 9	3.39	7.46	0.74	.83

TABLE 6.3

DATA FOR THE ESTIMATION OF K_L, C_{fm} FOR DEGASSED AND NITROGEN-SATURATED IRON IN SMOOTH NOZZLES.

For degassed silver the best equation for the discharge coefficient was

$$(C_D^{-2} - 1) = (0.23 \pm 0.03) + (0.022 \pm .001)\ 1/d \quad .. \quad 6.9$$

so that $K_L \sim 0.23$ and $C_{fm} \sim 0.0055$. The consistency of the results is very good in view of the experimental accuracy in C_D measurement which is only about $\pm$ 6% relative.

For degassed iron and nitrogen in smooth alumina nozzles the results are given in Table 6.3. All the nozzles were short so that it was possible only to estimate mainly the loss in the entry. The C_D values did not vary much beyond the experimental limits of accuracy. From the data we can conclude only that for nozzles of $1/d \sim 2.2$

$$(K_L + 4C_{fm}\ 1/d) \sim 0.7$$

The results on the combined loss due to the entry and to friction in short nozzles were of course vital in estimating the corresponding cases in flows with nucleation since nucleation was assumed not to occur in the nozzle entry.

Although it is regrettable that measurements of C_{fm} were not made, they would not have been very useful in trying to estimate C_{fm} in bubbly flows where the friction factor must be affected by the nucleating and growing bubbles.

Run No.	1/d	Re_3 ($\times 10^3$)	C_D	$(C_D^{-2} - 1)$
G1	5.0	5.66	0.39	5.57
G11	5.79	8.27	0.45	3.94
E4	5.89	6.77	0.41	4.95
P3	5.98	4.57	0.39	5.57
G12	6.31	7.94	0.47	4.67

Table 6.3(a)

Data for the estimation of K_L, C_{fm} for rough alumina nozzles, using degassed and nitrogen-saturated streams.

K_L - values					
Run No. / C_{fm} assumed	G1	G11	E4	P3	G12
.2	1.57	- .69	.24	.79	.67
.15	2.57	.47	1.42	1.98	0.88
.1	3.57	1.6	2.6	3.56	2.15
.08	3.97	2.09	3.07	3.66	2.67
.05	2.78	3.77	4.57	4.37	3.41

Table 6.3(b)

K_L values for different assumed C_{fm} for rough alumina nozzles using degassed and nitrogen-saturated iron streams.

Run No. -	l/d -	P_v (mmHg)	ΔP_t (mm Hg)	C_D -	P_e^* (mmHg)	ρ_e^* -
G2	5.0	10^{-3}	786	0.34	160.3	.59
G3	5.0	1.5	791	0.35	141.4	.49
G5	5.0	1.0	790	0.33	179.2	.69
P5	8.3	10^{-3}	792	0.30	175.2	.82

Table 6.3(c)

Estimated ratio of volumetric fluxes at nozzle exit for Fe-H flowing through rough alumina nozzles.

$(C_{fm} \sim 0.1;\ K_L \sim 3.0)$

Photographic observation of the Fe-H streams showed that the break-up of Fe-H flowing through the rough nozzles was more vigorous than through the long, smooth nozzles. Fig. 6.3 (a,b).

The C_D- values are extremely low and most consistent with K_L- value of $\sim$ 3.0 and $C_{fm} \sim$ 0.1 (Tables 6.3 a,b). Tables 6.3 (c) and 6.4 contain the estimated ratios of the volumetric fluxes at the nozzle exit for Fe-H flowing through rough and long smooth nozzles respectively. These confirm that the gas released at the nozzle exit was greater in the former case.

The raw data for the Fe-N, Fe-H and degassed molten iron in rough nozzles are contained in the appendix, (pages 226, 227 and 231 respectively). It is apparent from these data that the behaviour of the Fe-N, Fe-H systems are significantly different from the C_D measurements.

The data for the rough alumina nozzles are given in Tables 6.3 (a), (b) and (c) for molten iron.

The reasons for the high K_L and C_{fm} values for molten iron flow are not understood.

The values obtained for silver, which are in line with expectations, suggest that the timing, measurement of nozzle diameter, and other experimental tasks were properly carried out.

These results demonstrate that in the rough nozzles the flow characteristics were too poor to be used as a basis for modelling flow in larger nozzles.

6.4. ESTIMATION OF THE VOLUMETRIC RATIO OF GAS FORMING IN NOZZLES.

The work of Mizoguchi (7) has been reviewed in section 2.1. Of particular interest is his experimental observation that the static pressure at the nozzle exit for the choked flow was higher than and nearly independent of the chamber pressure. In his system pressure remained at about 200 mmHg when the chamber pressure was varied between 10 and 100 mmHg.

In our system the gas volumetric ratios at the nozzle exit were estimated using equ. 6.4 and 6.5 since no direct exit pressure measurements were practicable.

The gas volumetric ratios for Fe - H are given in Table 6.4 for smooth nozzles. The calculations indicate the the flow was choked in the smooth nozzles. Photographic observation of the streams showed that there was vigorous break-up.

Run No.	1/d -	P_v (mmHg)	ΔP_t (mmHg)	C_D -	P^*_e (mmHg)	δ^*_e
A33	2.44	0.1	783	0.69	69.7	0.06
D 3	5.06	1	790	0.63	116.9	0.13
E 3	7.68	10^{-3}	788	0.59	143.7	0.18
P 4	8.01	12	780	0.56	179.2	0.25
E 2	8.9	10^{-3}	791	0.59	136.25	0.17

TABLE 6.4

ESTIMATED RATIO OF VOLUMETRIC FLUXES AT NOZZLE EXIT FOR Fe - H FLOWING THROUGH SMOOTH ALUMINA NOZZLES.

$C_{fm} = 0.01 \quad K_r = 0.69$

The same argument may be extended to the Fe - C - O system. This mainly exhibited homogeneous bubbly flow as illustrated with Fig. 5.2 The results of the calculations confirm choking. Tables 6.4 and 6.5 also confirm the better break-up of the Fe - C - O than the Fe - H systems in the same type of nozzle.

Table 6.6 contains the data on the estimated ratio of the volumetric fluxes at the nozzle exit for Ag - O system flowing through smooth alumina nozzles.

The average δ^*_e value obtained by Mizoguchi for Ag - O flowing through Nimonic 75 nozzles $\sim$ 0.20 compared to an average value of 0.35 in our system.

The results can only be compared with caution since the nozzle materials differ very widely in both cases. Tables 6.4, 6.5 and 6.6 also indicate that break-up improves with increasing l/d ratios. Too far-reaching conclusions cannot be made because of the rather narrow range of l/d covered in the current work and the sensitivity of the estimated δ^*_e values to the nozzle constants.

Key	Run No. —	1/d —	P_v (mmHg)	ΔP_t (mmHg)	C_D —	P^*_e (mmHg)	δ^*_e —
	C 5	1.86	1.0	781	0.53	236.1	.36
	B15	2.34	2.0	781	0.50	251.7	.41
	C10	2.58	10^{-3}	782	0.57	195.1	.33
1	B4	3.0	0.2	781	0.49	264.3	.47
	$S_{T_{LSN}}$ 9	7.03	1.0	774	0.50	235.0	.41
	$S_{T_{LSN}}$ 7	7.85	1.0	784	0.51	225.2	.37
	B 9	1.89	0.2	788	0.51	251.8	.42
2	B 5	2.3	1.0	777	0.51	250.0	.42
	B 8	3.3	0.2	785	0.56	201.0	.27

TABLE 6.5

ESTIMATED RATIO OF VOLUMETRIC FLUXES AT NOZZLE EXIT FOR Fe - C - O SYSTEMS FLOWING THROUGH SMOOTH ALUMINA NOZZLES.

KEY

1. Iron saturated with 96CO - 4 CO_2
2. Iron saturated with 92CO - 8 CO_2

$K_L = 0.69 \quad C_{fm} = 0.01$

Run.No.	1/d —	$P_{\dot{v}}$ (mmHg)	ΔP_t (mmHg)	C_D —	P^*_e (mmHg)	δ^*_e —
SA 14	1.62	10^{-3}	787	0.60	256.2	0.30
SA 18	7.67	1.8	784	0.63	208.9	0.23
SA 26	8.52	1.0	794	0.60	232.7	0.27
SA 27	8.52	1.0	788	0.58	247.0	0.31
SA 33	11.63	0.16	799	0.55	262.7	0.37
SA 10	13.68	1.7	785	0.51	281.1	0.46
SA 20	14.93	1.0	783	0.50	285.9	0.49
SA 22	14.93	1.0	787	0.54	256.6	0.38

TABLE 6.6

ESTIMATED RATIO OF VOLUMETRIC FLUXES AT NOZZLE EXIT FOR Ag - O FLOWING THROUGH SMOOTH ALUMINA NOZZLES.

$K_L = 0.23 \quad C_{fm} = 0.0055$

6.5 GENERAL REMARKS ON THE DIFFERENCES IN THE BEHAVIOUR OF THE DIFFERENT SYSTEMS INVESTIGATED.

This section contains a general discussion of the arguments to explain the different behaviours between the Fe-H, Fe-N, Fe-N-S, Fe-C-O systems.

6.5.1 Nozzle Roughness.

The reason for the decision to carry out experiments in rough nozzles was to impose conditions nearer to industrial situations as far as actual surface structure was concerned. The arguments in support of heterogeneous nucleation on solid walls, and in particular the work of Davies et al on the importance of refractory cavity size, have been reviewed in Section 2.2. Bradshaw has shown that for heterogeneous nucleation on a flat surface in the molten steel-hydrogen system a contact angle as high as 100 - 150° only allowed trivial reductions over the requirements for homogeneous nucleation, but that a cavity radius of $\sim 10^{-3}$ cm would only require a supersaturation of ½-2 atmosphere at contact angles $\sim$ 90°.

A physical model of a nucleation sequence has been considered as illustrated with Fig. 3.4. This provides information on the interrelationship between the cavity radius (R_c), embryo radius (r_c), stable bubble nucleus (r_o), and the saturation pressure (P_b). It can be shown that $2R_c = r_c \leqslant l_c$ where l_c is the depth of the cavity,

for stable bubble nuclei to be produced, a condition more favourably met by a rough nozzle with deep cavities.

From Table 6.7 the average calculated exit pressure for Ag-O in smooth alumina nozzles = 253.5 mm Hg. Obviously nucleation would have commenced further upstream where the local pressure would be higher. Considering Run SA 22, which is typical of this series, and substituting for C_{fm}, the local pressure = 413 mm Hg at the start of the parallel section. Assuming the depth and radius of the active cavities, and the size of the bubble nuclei are all close to the minimum then $l_c \sim 2R_c$, and $r_o \sim r_c$, and substituting into

$$r_o \simeq 2\sigma / P_b - P_{local} \quad \ldots\ldots\ldots\ldots\ldots 6.7$$

the saturation pressure, P_b and local pressure, P_{local} $r_o \sim 3 \times 10^{-3}$ cm, and $l_c \sim 6 \times 10^{-3}$ cm.

Where $P_b - P_{local}$ becomes smaller as in the event of a smaller degree of supersaturation, R_c and l_c would have to be correspondingly higher for stable nuclei to be produced. This is the basis for the use of rough nozzles.

In the case of molten iron saturated with hydrogen where σ = 1750 dynes/cm and the maximum value of P_{local} = 370 mm Hg the value of l_c would need to be at least 1.3×10^{-2} cm.

The typical gas content in industrial plants has been given earlier (Table 3.2) and discussed in section 3. It is apparent that these are below the saturation level. The fact that such streams do break up may be partly accounted for by the availability of numerous deep cavities on the nozzle wall (Table 3.3). It is however appreciated that there would be a cavity size above which the molten iron will penetrate into the crevice and therefore be rendered unsuitable as a nucleation site. The rough nozzles were sectioned for close microscopic examination and there was no evidence of chemical attack or metal penetration via any available open pores.

It is significant that while little break-up occurred in the smooth nozzles with Fe-H, the same system gave vigorous break-up in rough nozzles (Fig. 6.3).

The work on rough nozzles has illustrated the complexity of the interplay between the laboratory experiments and the industrial process, and the caution demanded while applying results of model studies to industrial problems.

6.5.2. <u>The effect of l/d ratio of nozzles, and surface tension.</u>

The surface tension of Fe - H is high (σ = 1750 dynes/cm) since hydrogen is not a surface active element and the requirement for large cavities had to be

met before hydrogen would nucleate vigorously. The probability of having an occasional cavity meeting this criterion increases with high l/d ratios. This may well explain the fact that the nucleation of hydrogen on the smooth nozzles further decreases with shorter nozzles. However, in work at room temperature with smooth nozzles, and with no possibility of there being any large cavities (9), increasing l/d ratio does appear to increase the amount of bubble nucleation. This effect may be the result of increasing turbulence as l/d is increased. Eddies resulting from turbulence may well cause regions of low pressure and thus enhance heterogeneous nucleation.

The results presented in Tables 6.4 and 6.6 suggest that nucleation intensity increases with l/d ratio.

In the Fe - C - O system the surface tension was lower due to the presence of dissolved oxygen (this is further discussed later). The cavity size requirements will be less stringent and this may partly explain the difference between the Fe - C - O and Fe - H systems in the same type of nozzles.

The solubilities of nitrogen, hydrogen and C - O in molten iron at 1600°C under some of our experimental conditions are presented in Table 6.7. Fig. 6.4 illus-

trates the relative appearance of typical Fe - N, Fe - H, Fe - C - O systems.

6.5.3. Solute diffusivity.

The Fe - N system did not break up in either smooth or rough nozzles. As shown in table 6.7 the solubility of nitrogen in iron is about the same as that of hydrogen when measured in moles/cm^3. Although the Fe - N did not break up in rough nozzles and at tank pressures down to 10^{-3} mmHg vigorous break-up was obtained with Fe - H in rough nozzles. This suggests that apart from nozzle roughness, other conditions must be simultaneously satisfied for nucleation to occur. Since nitrogen has a greater effect than hydrogen in lowering the surface tension of molten iron, nitrogen will be expected to be at an advantage. Since the residence time of the stream in the nozzle is small (velocity $\sim$ 250 cm/sec., residence time $\sim$ 4 m sec.) the low diffusivity of nitrogen into the cavities at the refractory surfaces may explain the difference between the Fe - H and Fe - N systems.

6.5.4. Effect of surface active elements.

The work of El-Kaddah (32) demonstrated the supersaturation pressures at which homogeneous nucleation can occur depends on the oxygen activity in the Fe - C - O system and also on the presence of oxygen in the Fe - N system. At low oxygen activities, defined by

$P_{CO_2}/P_{CO} <$. 03 the critical supersaturation required becomes greater than 20 atmospheres.

The work requirement for the formation of a critical sized new phase in metastable equilibrium with an existing one is of the form

$$\Delta F^* = 1/3 \ \sigma A^* \quad \ldots\ldots\ldots\ldots\ldots\ldots 6.8$$

ΔF^* = critical work

A^* = surface area of the critical nucleus

σ = effective surface tension.

The nucleation frequency of a critical sized nucleus is related to ΔF^*.

$$I \ \alpha \ \exp(-\Delta F^*/kT) \quad \ldots\ldots\ldots\ldots\ldots\ldots 6.9$$

Thus nucleation frequency is a function of the surface tension.

The addition of 0.1 wt-% sulphur to the Fe-N system was designed to test whether lowering of the surface tension alone would significantly improve the nucleation frequency as to bring about improved break-up. Fig. 6.5 shows the surface tension of iron at 1500°C in the presence of S, O, N, P, C.

Sulphur has a negligible effect on the solubility of nitrogen in molten iron. $e^S_N = 0.013$ so that for an 0.1 wt-% sulphur addition the value of $f_S^N = 1.003$

Fig. 6.6 shows the relative appearance of (a) Fe - N, and (b) Fe - N - S flowing through long, rough nozzles. This

shows that the addition of sulphur, despite its effect in lowering the surface tension, does not aid stream break-up. From this observation it can be concluded that the presence of a surface active element with the accompanying lowering of surface tension is not necessarily significant in the heterogeneous nucleation of the gas phase.

El-Kaddah (32) studied in a levitation cell nucleation in Fe - N with N_2 saturation pressures of 100 atm. which was equivalent to Fe - C - O ($92CO-8CO_2$) in terms of lowering of surface tension. He observed no homogeneous nucleation. Levine (60) has suggested that oxygen probably plays a significant role in gas bubble nucleation in molten iron and this has been confirmed by El-Kaddah.

Some runs were carried out with CO - CO_2 mixtures. The Henrian activities of some of these mixtures in molten iron at 1600°C are tabulated in Table 3.1. In the sixth column of the same table the term $(h_c/h_o)(D_c/D_o)^{\frac{1}{2}}$ is also given. From the stoichiometry of the reaction $\underline{C} + \underline{O} = CO$, 12 grams of carbon will be expected to react with 16 grams of oxygen at the reaction interface. Therefore the ratio of $\underline{C}/\underline{O}$ in the bulk should be equal to 0.75 for equimolar concentrations of oxygen and

carbon in the melt, and this corresponds roughly to 93.5 CO - 6.5 CO_2.

The major problem with the Fe - C - O series was the attack on the crucible as discussed in section 4.5. This would have permitted a clearer understanding of the role of increased oxygen potential in break-up. It is significant that within the limited range covered some light is shed on the importance of oxygen activity: the less oxidising 98CO - 2CO_2 mixture produced less break-up than obtained with 96CO - 4CO_2 mixture, other conditions remaining constant. However, there is no significant difference between iron saturated with 96CO - 4CO_2 and 92CO -8 CO_2 gas mixtures (Table 5.1.). The later observation may be due to the fact that the excess surface concentration of oxygen is nearly constant above 0.04 wt-% which corresponds to about 96CO - 4CO_2.

Hence from the qualitative observations of the relative effects of nitrogen, sulphur and oxygen on heterogeneous nucleation in molten iron it can be suggested that the amount and nature of the adsorbed molecules on the melt surface has a significant effect on the nucleation event.

Diffusing species	H	N	$96CO - 4CO_2$		$98CO - 2CO_2$	
			O	C	O	C
Solubility in Iron at 1600°C (wt-%)(10^{-3})	2.68	45.04	51	39.8	24.8	82
Diffusion co-efficient (cm^2/sec) (10^{-5})	150	6-8	5.2	41.2	5.2	41.2
Source of data	20c	20c	59	59	59	59

Table 6.7.

SOME PHYSICAL PROPERTIES OF SOLUTE ELEMENTS RELEVANT TO THEIR DISSOLUTION IN MOLTEN IRON AT 1600°C

FIG. 6.3

(a) HYDROGEN-SATURATED IRON STREAM FLOWING THROUGH A LONG, SMOOTH ALUMINA NOZZLE. RUN E3.

(b) HYDROGEN-SATURATED IRON STREAM FLOWING THROUGH A LONG, ROUGH ALUMINA NOZZLE. RUN P5.

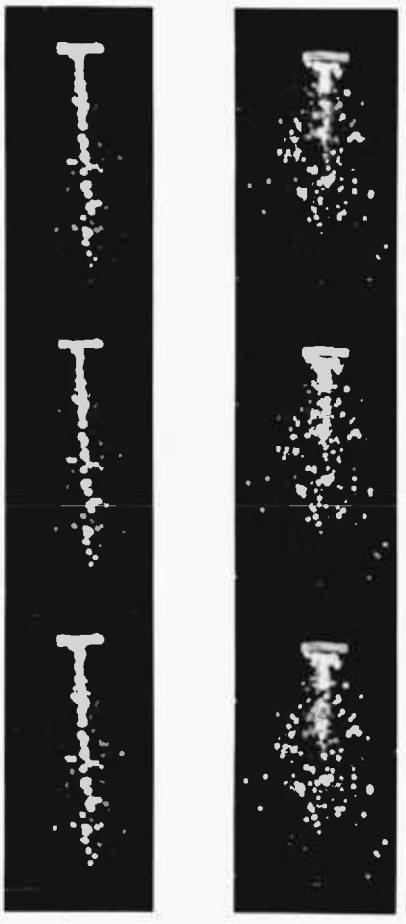

(a) (b)

FIG.6.3

FIG. 6.4

(a) NITROGEN-SATURATED IRON STREAM FLOWING THROUGH A LONG ROUGH NOZZLE. RUN G11.

(b) Fe-C-O STREAM FLOWING THROUGH A SHORT, SMOOTH NOZZLE. RUN B8.

(c) HYDROGEN SATURATED IRON FLOWING THROUGH A LONG, SMOOTH NOZZLE. RUN E2.

FIG. 6.6

(a) Fe-N-S STREAM FLOWING THROUGH A ROUGH NOZZLE. RUN C9.

(b) Fe-N STREAM FLOWING THROUGH A ROUGH NOZZLE. RUN G11.

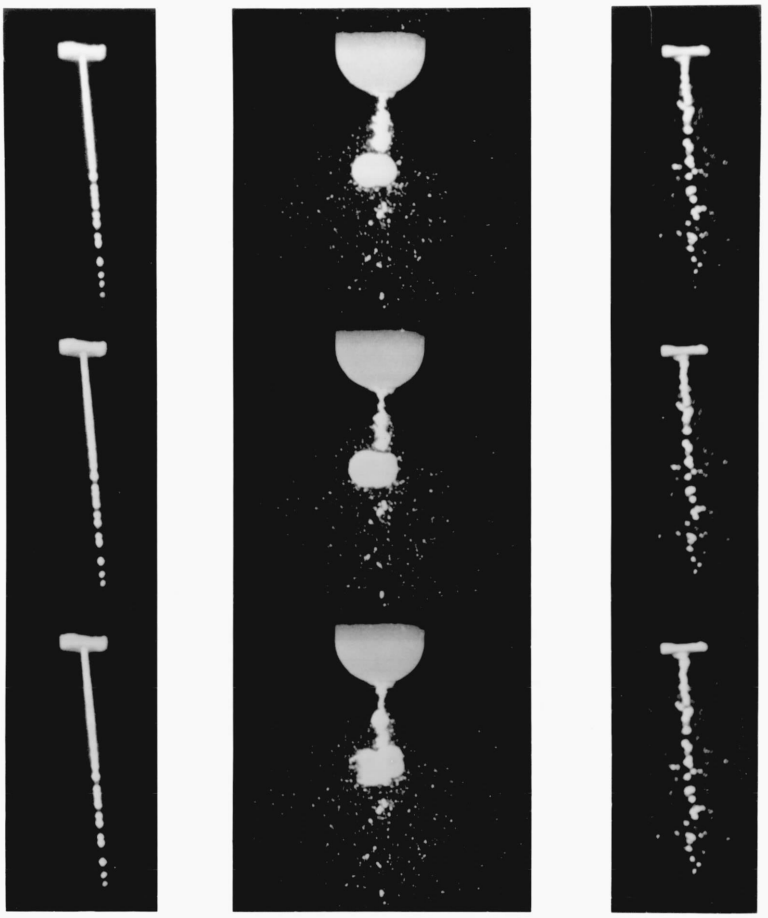

(a) (b) (c)

FIG.6.4

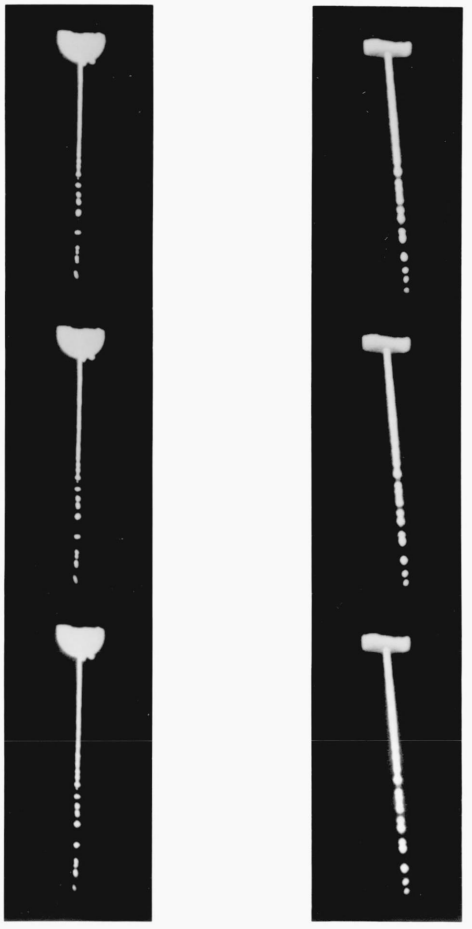

(a) (b)

FIG.6.6

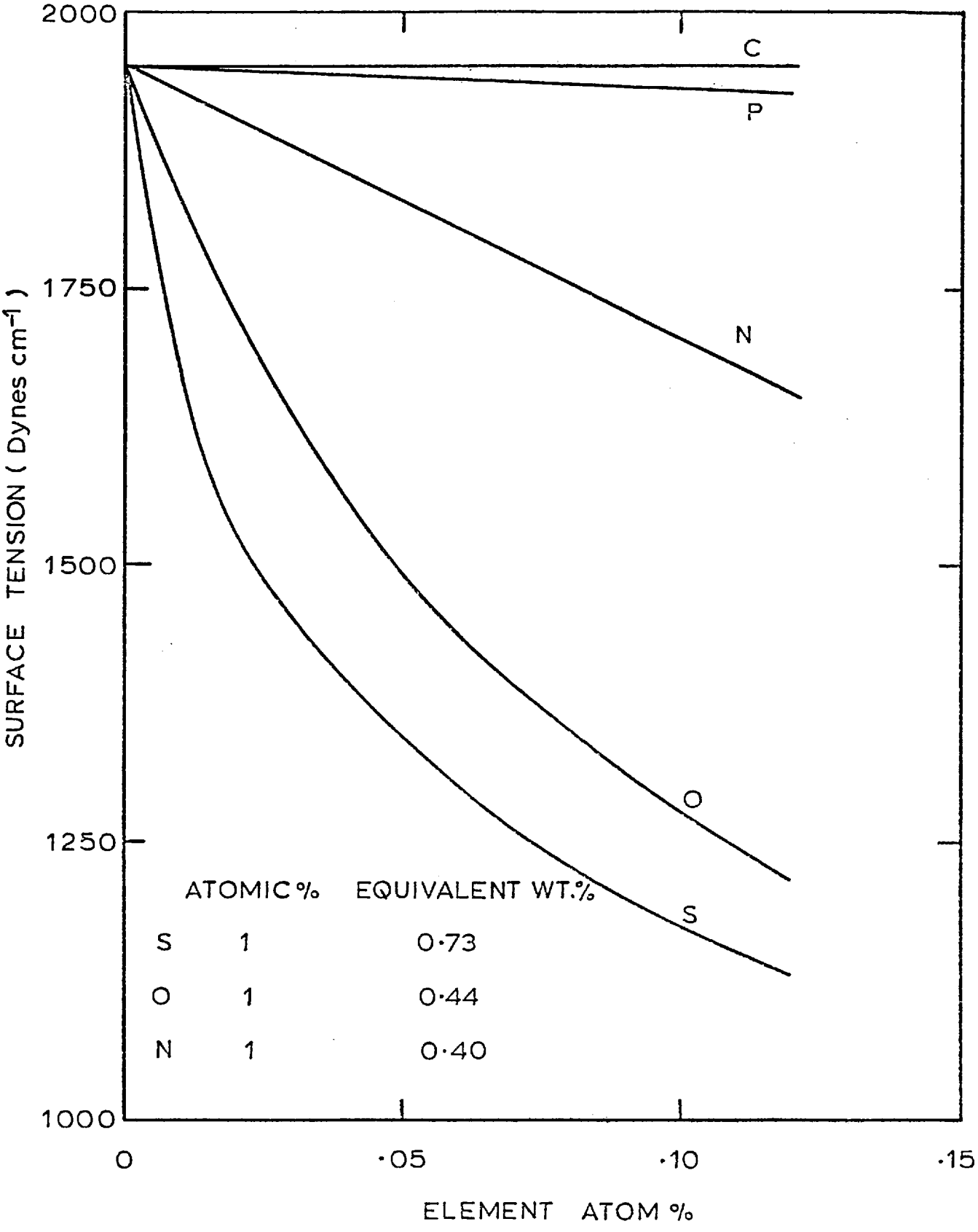

FIG. 6.5 EFFECT OF THE ADDITION OF SOME SOLUTE ELEMENTS IN IRON AT 1550°C ON SURFACE TENSION (20)

6.5.5. Fluid dynamic effects.

The work of Min et al.(9), Eisenklam and Hooper(8) has been reviewed in section 2.1. Their results show how stream break-up may occur as a result of phase changes from liquid to vapour and/or turbulence. With a view to testing whether the behaviour observed in this work can be correlated in the same category as that of the work mentioned above, the Reynolds and modified cavitation numbers of our streams have been calculated.

The detailed experimental results are presented in the appendix. There was no distinct pattern into which the flow with different gases could be classified in terms of modified cavitation number. The modified cavitation and Reynolds numbers of some runs are given in Table 6.8. The modified cavitation numbers of runs B.15, C.10 are respectively 9.1, 8.0; whereas these streams exhibited homogeneous bubbly flow, the Fe - N systems - Runs G.11, G.12 - with Ca' = 28.1, 36.2, did not break up.

According to Min et al. in their system, for

$Ca' < 9$, metastable single phase flow;

$9 < Ca' < 15$ unstable flow;

$15 < Ca'$ < two phase flow;

where Ca' is as defined by equ. 2.4.

RunNo	System	Nozzle type	Modified cavitation number, Ca`	Diameter Reynolds number, Re	Comments (observation)
G 2	Fe-H	Rough	42.5	5.32	Break-up
G 3	"	"	42.0	5.22	"
G 5	"	"	46.9	4.74	"
G11	Fe-N	"	28.1	8.27	No break-up
E 4	"	"	34.9	6.77	"
G 6	"	"	20.8	7.08	"
G12	"	"	36.2	7.94	"
B15	Fe-C-O	Smooth	9.1	5.04	Break-up
C10	"	"	8.0	5.70	"

TABLE 6.8

THE REYNOLDS AND MODIFIED CAVITATION NUMBERS OF TYPICAL RUNS.

6.5.5(a). Rayleigh break-up, secondary and multiple nucleation.

One of the main criticisms of Warner's work (5) was the difficulty in interpreting the cause of his observed stream break-up as the nozzle exit was not visible and observation was limited to between 9 - 22 cm downstream of the nozzle exit. Secondly he used porous nozzles which were conducive to entrainment of residual gas in the stream. Hence it was difficult to ascertain whether the locally observed break-up was as a result of gas entrainment, fluid dynamic effects or spontaneous nucleation of gas bubbles on the nozzle wall.

In our system the nozzle was not porous and we were able to observe up to 30 mm of the lower end of the crucible (in the case of short nozzles), the nozzle exit and up to 300 mm downstream. It was therefore possible to make the following observations:

1. Although the degassed nitrogen-saturated iron streams were continuous at the nozzle exit they exhibited Rayleigh break-up downstream (Fig. 5.1 (a), (b)). This is believed to be a fluid dynamic effect as discussed in section 3.5.2. A typical appearance of Warner's stream is illustrated in Fig. 5.1(c) from which it becomes apparent that the origin of the break-up in our

system would have been a matter of conjecture if the nozzle exit were not visible.

2. Secondary nucleation featured prominently downstream. It commenced, in most cases, in the immediate region of the collapse of the large gas bubbles. These bubbles were unstable and relatively shortlived and did not contribute significantly to stream break-up (Fig.6.8). The secondary nuclei were probably gas "pockets" trapped in the stream as it collapsed back after bubble bursting.

3. Multiple nucleation and 'satellites' were also frequently observed. The satellites were bubbles which grew on the expanding film of the primary bubbles. The satellites grew at the expense of the main bubble and when both were about the main size they burst explosively, resulting in vigorous stream disintegration (Figs. 6.9).

These observations illustrate the variety of reasons causing break-up and hence the need to be able to observe the nozzle exit and a substantial length downstream before correct interpretation of the origins of break-up could be made. The design of an apparatus to allow the attainment of this objective was the main feature of our design philosophy.

6.5.6. Droplet formation following the collapse of gas bubbles.

The formation of droplets following stream break-up due to the collapse of gas bubbles downstream provides the most effective path for degassing. This is due to the large surface area created and exposure of the droplets to the vacuum. Fig. 5.2 shows the explosion of a single bubble and the resulting metal fragmentation. In our system the time available for fall was ~0.4 seconds. Bradshaw and Richardson (20b) considered the case where circulation within individual droplets died down in the vacuum and calculated the fraction of materials transferred as a function of $[Dt/R^2]^{\frac{1}{2}}$, where R is the radius of the drop, D the diffusion coefficient and t the time. Their results, discussed in section 2.2., demonstrate the importance of droplet size.

In our work detailed size analysis was not practicable due to the coalescence of the droplets. However a few measurements were made on the cine film and these were supplemented by sieve analysis of typical powders. In one particular run - G3 - the powder analysis yielded the results shown in Table 6.9 .

Since it was not practicable to collect all the powders, comparison between the various systems and the effect of small variations in tank pressure in the range 10^{-3} - 4 mmHg were not possible.

The results of the powder analysis suggest the feasibility of powder production via this route particularly if an oil stable at low pressures was employed as a quenchant.

Sieve size (microns)	Cumulative weight of powder through sieve (grams)	Cumulative percentage of the total free powder.
105	3.7	3.7
250	9.8	9.9
353	13.2	13.4
500	21.4	21.7
599	34.7	35.2
700	41.0	41.5
1000	52.8	53.2
1500	74.2	75.2
2000	98.7	100

TABLE 6.9

ANALYSIS OF TYPICAL POWDER RESULTING FROM STREAM BREAK-UP.

* The total mass of charge was 315.5 grams. Only 98.7 grams were collected as free powder while the balance coalesced in the plumbago collector.

6.6. KINETICS OF BUBBLE GROWTH AT REDUCED PRESSURES.

6.6.1. Introduction.

If a gas becomes saturated in a solvent a bubble may nucleate at cavities in the solid container. Bubble nucleation and subsequent growth have been the subject of many theoretical (36)(38)(61)(61a) and experimental investigations (37)(61)(61a)(62). These authors have considered the effects of ambient pressure, liquid inertia, viscosity, surface tension and transport of heat and volatile material through the liquid to the surface on bubble growth.

Little experimental work has, however, been reported on gas bubbles growing in molten streams discharging into regions of reduced pressure. This section is concerned with a brief description of observed bubble growth in our system during all but the earliest stages.

6.6.2. Experimental technique.

Typical processed films were analysed by projecting the images into a smoked glass screen of a movie analyser using the diameter of the bottom part of our alumina crucible as the reference dimension. The time lapse between successive frames was evaluated either by means of the timing marks on the edge of the film or was estimated by the method described below: by noting the position of the section in which the measurements were to

be carried out and using the typical film speed - footage-driving voltage curves supplied with the camera.

Isolated gas bubbles were selected to avoid any overlap between adjacent growing bubbles competing for dissolved solutes. For spheroid bubbles the radius was taken as half the arithmetic average of the two main axes. The zero time was taken as that corresponding to the frame on which the appearance of the bubble was first observed. In most cases the gas bubbles only became large enough ($\sim$ 2mm) to be detected after travelling several nozzle diameters downstream and then rapidly grew to the maximum size $\sim$ 30 mm diameter before bursting. In this region bubble sizes were measured and the growth constant, as defined by Scriven (36), determined.

6.6.3. Results.

Winterton (62) developed a quantitative expression for predicting bubble size on detachment from nozzle crevice in a flowing stream:

$$r = Cd \left[\frac{F(\theta)}{We}\right]^{n} Re^{m} \qquad \ldots\ldots\ldots 6.10$$

n, m, C are constants depending on the initial bubble size relative to the pipe diameter, d; We, Re are Weber and Reynolds numbers based on nozzle diameter; $F(\theta)$ is related to the contact angles between the solid wall and

Notes on the validity of the application of Scriven's Law to the gas bubbles surrounded by a film growing in a narrow stream in the vacuum chamber. (Ref. Fig 5.6).

Assumptions

1) The bubble grows from within a cylindrical stream element of diameter and height 0.2 cm respectively, the average diameter of our nozzles.

2) The bubble is spherical with maximum diameter of ~10mm (see Appendix A.2: BG14, 15, 16, 17, 18).

3) The pressure inside the bubble is entirely due to that of nitrogen ~ 20 mm Hg, the typical chamber pressure at the end of the run.

4) The mean temperature remains constant at ~ 1600°C.

Assuming that the stream element is nitrogen saturated at 1 atm. pressure its mass of ~ 4.5×10^{-3} gram. contains ~ 2.2×10^{-6} grams. N. Applying the gas laws the mass of nitrogen inside the bubble ~ 2.5×10^{-6} gram. Thus all of the original nitrogen content of the film had been transferred inside the bubble.

Since the liquid film surrounding the bubble must contain nearly the initial concentration if Scriven's Law is applicable to describe its kinetics, it is clear that the Law can only be applied for bubble diameters up to ~ 5 mm.

detaching bubble (62). Considering the case F (θ) at its maximum value of unity and substituting typical values of Re $\sim 10^4$, We ~ 50; d ~ 1.5 mm, the initial bubble size on detachment to the stream, $R_o \sim 5 \times 10^{-3}$ cm.

Tables 6.10 - 6.11 contain typical data obtained for the growth of CO, and N_2 bubbles at a chamber pressure of $\sim$20 mmHg. Figs. 5.5, 5.6 show the relative bubble sizes; the plots from the data satisfy the general relationship $R \alpha t^{\frac{1}{2}}$ as shown in Fig. 5.7, 5.8, and by taking the average slope of the several curves (data given in appendix) a value of 256 $\pm$ 39, 170 $\pm$ 26 (mm $sec^{-\frac{1}{2}}$) was obtained for CO and N_2 bubbles respectively, and the estimated growth constants were also 888 $\pm$ 133, 448 $\pm$ 67 respectively.

6.6.4 Discussion.

In the general case the equations of continuity and motion can be combined in the form

$$P_{bubble} - P_{\infty} = \Delta P_v + \Delta P_I + \Delta P_\sigma \quad \ldots\ldots\ldots 6.11$$

where

$$\Delta P_v = 4\mu \dot{R}/R \quad \ldots\ldots\ldots\ldots 6.12$$

$$\Delta P_I = \rho_L(R\ddot{R} + (3/2)\dot{R}^2 \quad \ldots\ldots\ldots\ldots 6.13$$

$$\Delta P_\sigma = 2\sigma/R \quad \ldots\ldots\ldots\ldots 6.14$$

Equations 6.12, 6.13, 6.14 denote the pressure constraints against bubble growth due to viscosity, inertial and surface

tension respectively.

Since our curves satisfy the general relationship $R^2 = At$ during the later stage of bubble growth (A is a constant experimentally determined) by differentiating R with respect to t it can be shown that

$$\Delta P_I = (\rho/2)(A/R)^2 \qquad \ldots\ldots\ldots \quad 6.15$$

This illustrates that the effect of the inertial forces is inversely proportional to the square of the bubble radius, suggesting diminishing inertial effects as growth continued.

Considering a bubble radius of 1.0mm, close to the size first observed in the stream and substituting the experimental value of A = 164 $cm^2/sec.$ in equation 6.15 ΔP_I, ΔP_σ are approximately 45 and 8 mm Hg. respectively. This indicates that the inertial effect may still be very important in this region of bubble growth.

Dimensionless quantities are normally used to quantify the relative importance of the dominant effects controlling growth: Φ, a surface tension parameter, $= 2\sigma/R(P_{Sat} - P_\infty)$. In our systems Φ varies between 0.65 for $R_o \sim 5 \times 10^{-3}$ cm in the choked nozzle with upstream pressure at 300 mm Hg. and 0.013 in the region of bubble observation where $R \sim 1.5 \times 10^{-1}$cm, $\Delta P \sim 760$ mmHg. The effect of decreasing Φ is to reduce the effect of surface tension in slowing down the initial stages of

bubble growth. The parameter $\bar{B}$ is a measure of the relative significance of diffusion and inertial effects and combines the effects of the Jakob number, Ja and the ratio: available pressure driving force/driving force due to diffusion. For $\bar{B} << 1$ the process would be diffusion controlled whereas for $\bar{B} >> 1$ growth would be expected to be inertia controlled.

$$\bar{B} = \overline{Ja}^2/G^{\frac{1}{2}} \quad \ldots\ldots\ldots (6.16)$$

$$\overline{Ja} = \Delta C/\overline{\rho}_G \quad \ldots\ldots\ldots (6.17)$$

$$G = R_o^2 \Delta P/\rho_L D^2 \quad \ldots\ldots\ldots (6.18)$$

where $\Delta C = C - C_{sat}$, R_o = initial bubble radius, D = gas diffusivity, ρ_L = liquid density. For our growing bubbles the estimated value of $\bar{B} \sim 2.1 \times 10^4$, suggesting again that the inertia effect was significant.

Viscous forces are apparently negligible in view of the very low values of $Sc/\sqrt{G} \sim .02$.

The growth constant predicted by Scriven law is given by:

$$\beta = (\rho_L/\rho_g)[(C_b - C_{sat})/(1 - C_{sat})] \quad \ldots\ldots 3.45$$

where C_b, C_{sat}, expressed in gram of solute per gram of solvent, corresponds to the solute conc. at partial pressure of 1 atm and 20 mmHg respectively. An average partial pressure of 20 mmHg may be assumed inside the expanding bubble without much error.

$(\rho_L/\rho_g) \sim$ 1.49335 x 10^6 for both N_2 and CO at 1600°C, 20 mmHg.

The diffusivities of $\underline{C}$, $\underline{O}$ and the h_c, h_o corresponding to 96CO-4CO_2 in iron are given in Table 6.7 since $h_c \sim h_o$ but $D_c \gg D_o$, it may be assumed that the transport of oxygen is rate controlling.
Equ. 3.4, 3.15 may be used to evaluate $C_{sat}(\underline{N})$, $C_{sat}(\underline{O})$, and hence $(C_b - C_{sat})(1 - C_{sat})$, substituting these in equ. 3.45 $\beta \sim 560$, 760 for N_2, CO respectively, compared with the experimental values of 448 $\pm$ 67, 888 $\pm$ 133.

Although the agreement appeared good it should be pointed out that the evaluated β-value, which is a function of (ρ_L/ρ_g), is very sensitive to small changes in pressure inside the bubble particularly at very low pressures.

6.6.5 Conclusion.

For the growth of spherical gas bubbles in iron saturated at 1 atm pressure and discharged into an environment at a pressure of ~20 mmHg., the growth rate of the bubbles is controlled by liquid inertia in the early stages. Later growth is controlled by liquid diffusion of the solute gas.

BG7	BG10	BG12	$t^{\frac{1}{2}}$
BUBBLE DIAMETER 2R (mm)			$(sec^{\frac{1}{2}})$
3.30	3.32	4.80	0
5.20	4.71	7.08	.022
7.52	6.47	9.07	.032
9.37	8.05	11.09	.039
11.32	9.14	12.09	.045
12.04	10.74	13.27	.050
12.97	11.67	14.66	.055
14.71	12.90	16.12	.059
15.99	14.13	16.73	.063
16.70	15.15	17.52	.067
17.33	16.05	18.88	.071
18.72	17.24	19.60	.074
19.27	17.86	20.32	.076
20.32	18.72	21.41	.081
21.00	19.44	22.27	.084
22.11	20.32	22.99	.087
22.85	21.41	23.87	.089
23.78	22.16	24.87	.092
24.80	22.92	25.22	.095
25.52	23.50	26.31	.098
26.40		27.03	.100
26.89		27.96	.103
27.82		28.81	.105
28.54		29.19	.107
29.14			.110

Table . 6.10

Typical data on the kinetics of carbon monoxide bubble growth in molten iron discharging into a vacuum at $\sim^{20}$ mmHg pressure.

BG15	BG16	BG17	Run No. / $(t)^{\frac{1}{2}}$ $(sec^{\frac{1}{2}})$
BUBBLE	DIAMETER	2R (mm)	
3.74	6.24	3.94	0
7.89	7.26	7.87	.020
9.91	7.84	9.86	.028
10.72	8.19	10.32	.035
11.07	8.49	10.90	.040
11.76	9.26	11.16	.045
12.04	9.37	11.97	.049
12.71	9.86	12.09	.053
13.91	10.35	12.92	.057
14.13	11.11	13.76	.060
14.42	11.41	14.34	.063
15.36	11.48		.066
	12.34		.069
	13.20		.072
	14.08		.075
	14.71		.077
	14.99		.080
	15.78		.082
	15.85		.085
	16.22		.087

TABLE 6.11

Typical data on the kinetics of nitrogen bubble growth in molten iron discharging into a vacuum at ~20 mmHg pressure.

FIG. 6.8

(a), (b)

EXAMPLES OF A BURSTING GAS BUBBLE AND THE RESULTING DROPLET FORMATION. RUN E3.

FIG 6.9

AN EXAMPLE OF A SECONDARY/MULTIPLE NUCLEATION. RUN E3.

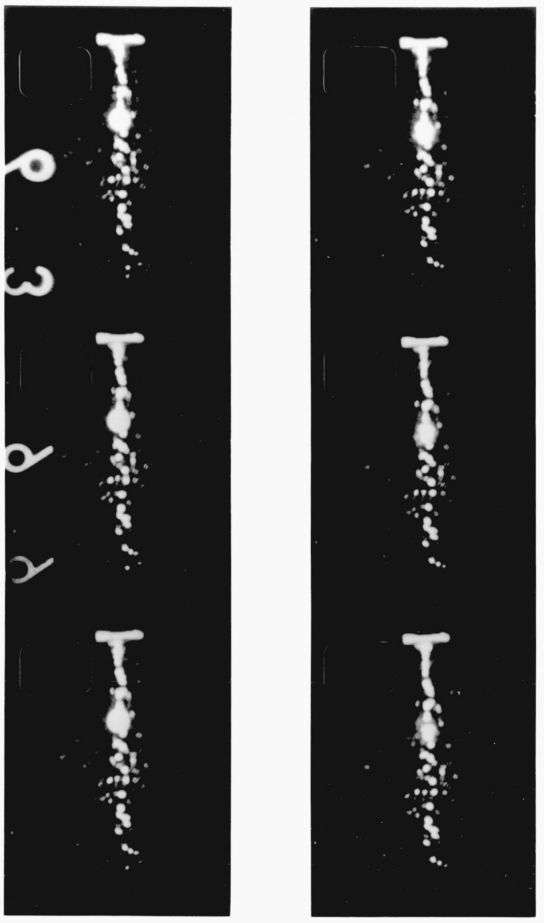

(a) (b)

FIG.6.8

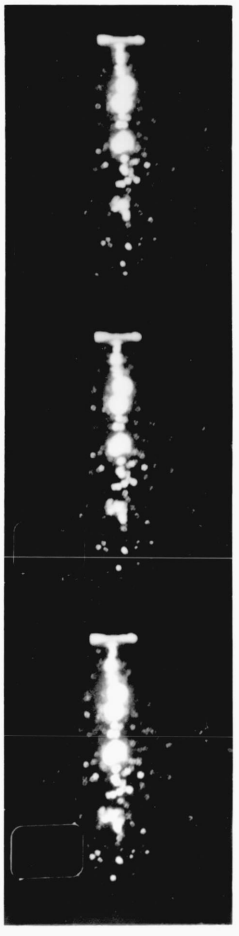

FIG.6.9

C H A P T E R 7.

CONCLUSION.

CHAPTER 7

CONCLUSION.

The objective of this work was to investigate the parameters that affect the spontaneous nucleation of gas bubbles on nozzle walls during the stream degassing of molten iron, particularly the effect of surface roughness and different gas solutes.

A special apparatus was developed during preliminary experiments. The main feature of the system was its versatility, since the crucible constituted a replaceable unit. Thus different materials could be used as crucibles depending upon the basic requirements.

The main experimental difficulties encountered in the programme, which limited the scope of the work, were essentially associated with crucible failures due to chemical attack of alumina, in the cases where oxidising gases were used, and poor resistance to thermal shock. It would be possible to substitute magnesia for alumina as a crucible material while the main system remained unaltered.

A photocell was used as a metal stream flow duration measuring device. A suitable stopper rod and a technique for sintering nozzles to the crucible have been successfully developed. The latter technique would provide an

opportunity for extending the current investigation to the study of the suitability of different commercial refractories used in the steel industry as nozzles in stream degassing plants.

The discharge coefficient (C_D) values of gas saturated molten iron in rough nozzles were very low and hence auxiliary runs were carried out with Ag - O (since this was the subject of recent investigation in Nimonic 75 nozzles) in both smooth and rough nozzles. For the same type of nozzle and l/d range the C_D values obtained for degassed iron were lower than for degassed silver. For a given system, either degassed silver or iron, the C_D values obtained in the smooth nozzles were significantly higher than for rough nozzles. The behaviour of the rough nozzles was rather irreproducible. The apparently high entry losses were possibly due to losses at the junction between the substrate and sinter. The results with the rough nozzles demonstrated that the flow characteristics were too poor for the results to be used as a basis for modelling flow in longer nozzles.

Hydrogen-saturated iron was found to break up more vigorously in rough nozzles than in smooth nozzles. Nitrogen saturated iron streams did not break up in either smooth or rough nozzles, while the addition of up to 0.1wt-%S

did not alter the stream behaviour. Iron streams containing dissolved carbon and oxygen (96CO - $4CO_2$; 92CO - $8CO_2$) showed homogeneous bubbly flow in both smooth and rough nozzles. These results suggested that although nozzle roughness might be an important parameter, other conditions affecting stream break-up include:

1. The solubility and diffusivity of dissolved gas;
2. Substantial nozzle l/d ratios;
3. The nature and amount of adsorbed surface active elements.

The choked flow theory was applied to the cases where stream break-up occurred in smooth nozzles and showed that for a given system showing break-up the ratio of gas to liquid volume in the stream at the nozzle exit (δ_e) generally increased with l/d ratios.

A study of the movie film of streams outside the nozzle exit confirmed an early retardation of bubble growth due to the combined effect of liquid surface tension and inertia, while the subsequent growth conformed with the parabolic growth law.

Finally it is hoped that this investigation will pave the way for similar mission-orientated attempts to establish a more realistic laboratory investigation of this and related problems.

A P P E N D I C E S

The appendices contain the raw data used for the calculation of discharge coefficient and all the related parameters; these are grouped according to systems, e.g. nitrogen-saturated iron in rough nozzles is contained in a separate table. They also contain the raw data on the kinetics of nitrogen and carbon monoxide bubble growth in molten iron in the vacuum chamber. Comments are made on the kinetics of iron melt saturation originally planned as part of the current programme.

A.1 The raw data used for the calculation of discharge coefficient and all the related parameters.

A.2 The raw data on the kinetics of nitrogen and CO bubble growth in molten iron in the vacuum chamber.

A.3 The kinetics of nitrogen saturation of iron melts.

A.1. RAW DATA FOR THE CALCULATION OF DISCHARGE COEFFICIENT AND RELATED PARAMETERS.

Run No. -	Charge Mass (Gram)	Nozzle Diameter (mm)	Length/ Diameter ratio -	tank pressure (mmHg)	ΔP_{total} (average) (mmHg)	Flow duration (secs)	Mean discharge coefficient C_D	Mass Flux (gram/ cm^2 sec)	Reynolds Number (10^3) -
SA17	361.22	2.05	1.62	0.5	787	2.8	0.89	3921	23.7
SA23	398.37	1.5	10.26	1.0	786	6.2	0.82	3636	16.09
SA24	401.04	1.5	10.26	1.0	785	6.2	0.85	3661	16.20
SA32	396.61	1.5	11.63	0.15	787	6.4	0.80	3507	15.52
SA34	391.81	1.5	11.63	0.14	786	6.3	0.81	3520	15.58
DEGASSED MOLTEN IRON IN SMOOTH NOZZLES									
G9	309.67	1.6	2.23	1.0	788	5.2	0.76	2963	7.94
B12	332.61	1.58	2.2	20.0	788	5.7	0.77	2977	7.59
C3	344.1	1.62	2.3	0.6	784	5.5	0.79	3036	7.91.

	Run No.	Charge mass	Nozzle diameter	Length/ diameter ratio	tank pressure	ΔP_{total} average	Flow duration	Mean discharge coefficient	Mass flux	Reynolds number	Modified cavitation number
	-	(gm)	(mm)	-	(mmHg)	(mmHg)	(secs)	-	(gm/ cm^2. sec)	(10^3)	-
	NITROGEN SATURATED IRON IN SMOOTH NOZZLES										
	A29	289.20	1.70	2.85	0.7	786	4.5	0.73	2831	7.82	5.34
	A30	283.31	1.42	3.38	0.1	781	6.48	0.72	2760	6.33	6.6
*	C9	339.24	1.62	3.39	10^{-3}	786	5.76	0.74	2859	7.46	6.2
	NITROGEN SATURATED IRON IN ROUGH NOZZLES										
	G11	312.07	2.42	5.79	10^{-3}	788	3.85	0.45	1762	8.27	28.1
	E4	270.66	1.84	5.89	10^{3}	783	6.4	0.41	1590	6.77	34.9
	G1	312.6	1.80	5.0	1.0	785	8.1	0.39	1519	5.66	32.4
	P3	336.66	1.60	5.98	10^{-3}	790	11.1	0.39	1509	4.57	39.6
**	G6	309.39	1.80	5.0	1.5	787	6.4	0.49	1903	7.08	20.8
**	G12	316.22	2.62	6.31	10^{-3}	794	3.6	0.42	1627	7.94	36.2

* with 0.1 wt-% sulphur added

** 10% H_2-90% N_2 gas solute dissolved.

Run No.	Charge mass	Nozzle diameter	length/ diameter ratio	tank pressure	ΔP_{total} average	Flow duration	Mean discharge coefficient	Mass flux	Reynolds number	Modified cavitation number
-	(gm)	(mm)	-	(mmHg)	(mmHg)	(secs)	-	(gm/ cm^2. sec)	(10^3)	-
HYDROGEN SATURATED IRON IN SMOOTH NOZZLES										
A33	362.0	1.49	2.44	0.1	783	7.8	0.69	2661	6.39	5.2
P4	340.83	1.54	8.01	12.0	780	8.43	0.56	2174	5.42	6.3
D3	311.41	1.50	5.06	1.0	790	7.24	0.63	2298	5.86	23.2
E2	284.75	1.50	8.9	10^{-3}	791	7.00	0.59	2298	5.56	22.5
E3	313.42	1.50	7.68	10^{-3}	788	7.8	0.59	2270	5.49	22.4
HYDROGEN SATURATED IRON IN ROUGH NOZZLES										
G2	212.77	1.8	5.0	10^{-3}	786	6.3	0.34	1330	5.32	42.5
G3	315.50	1.8	5.0	1.5	791	9.26	0.35	1341	5.22	42.0
G5	309.21	1.8	5.0	1.0	790	9.6	0.33	1268	4.74	46.9
P5	337.90	1.62	8.3	10^{-3}	792	13.92	0.30	1178	4.33	36.0

Run No.	Charge mass	Nozzle diameter	Length/ diameter ratio	tank pressure	ΔP_{total} average	Flow duration	Mean discharge coefficient	Mass flux	Reynolds number	Modified cavitation number
-	(gm)	(mm)	-	(mmHg)	(mmHg)	(secs)	-	(gm/ cm^2. sec)	(10^3)	-
OXYGEN SATURATED SILVER IN SMOOTH NOZZLES										
SA10	400.50	1.5	13.68	1.7	785	10.1	0.51	2244	9.93	46.5
SA14	389.65	2.05	1.62	10^{-3}	787	4.5	0.60	2632	15.93	4.5
SA18	381.04	1.5	7.67	1.8	784	7.8	0.63	2764	12.24	19.3
SA20	404.57	1.5	14.93	1.0	783	10.4	0.50	2202	9.75	59.1
SA22	406.60	1.5	14.93	1.0	787	9.8	0.54	2348	7.14	35.9
SA26	558.11	1.5	8.52	1.0	794	11.9	0.60	2654	11.75	23.5
SA27	376.0	1.5	8.52	1.0	788	8.3	0.58	2564	11.35	25.1
SA35	377.16	1.5	11.63	0.16	799	8.8	0.55	2426	10.73	38.7
OXYGEN SATURATED SILVER IN ROUGH NOZZLES										
SA3	355.0	1.803	10.47	10^{-3}	791	7.75	0.41	1795	10.76	62.9
SA7	378.69	2.09	9.56	10^{-3}	783	5.9	0.43	1872	12.95	52.3
SA29	388.47	2.19	4.84	10^{-3}	781	4.4	0.54	2344	18.82	16.9
SA30	416.12	2.19	4.84	0.2	781	4.7	0.54	2357	18.93	16.7

Run No.	Charge mass	Nozzle diameter	length/ diameter ratio	tank pressure	ΔP_{total} average	Flow duration	Mean discharge coefficient	Mass flux	Reynolds number	Modified cavitation number
-	(gram)	(mm)	-	(mmHg)	(mmHg)	(secs)	-	(gm/ cm^2. sec)	(10^3)	-
AIR SATURATED SILVER IN SMOOTH NOZZLES										
SA11	407.91	1.5	13.68	1.7	785	6.8	0.77	3087	13.65	24.6
SA16	389.68	2.05	1.62	0.5	787	3.4	0.79	3484	21.05	2.6
SA33	427.88	1.5	11.63	0.03	774	7.2	0.77	3363	14.88	19.5
AIR SATURATED SILVER IN ROUGH NOZZLES										
SA1	407.16	1.803	10.47	10^{-3}	793	5.9	0.61	2704	16.21	27.8
SA2	374.48	1.803	10.47	10^{-3}	791	5.4	0.62	2717	16.29	27.5
SA8	402.80	2.L9	10.47	10^{-3}	784	4.2	0.64	2797	17.68	23.5

CO-CO_2 MIXTURE SATURATED IRON IN SMOOTH NOZZLES

	Run No.	Charge mass	Nozzle diameter	length/ diameter ratio	tank pressure	ΔP_{total} average	Flow duration	Mean discharge coefficient	Mass flux	Reynolds number	Modified cavitation number
	-	(gm)	(mm)	-	(mmHg)	(mmHg)	(secs)	-	($gm/cm^2.sec$)	(10^3)	-
1.	$ST_{LSN}9$	304.39	1.50	7.03	1.0	774	9.0	0.50	1914	4.64	28.4
	$ST_{LSN}7$	192.15	1.50	7.85	1.0	784	5.5	0.51	1977	4.79	30.1
	$ST_{LSN}17$	296.12	1.50	7.33	0.2	781	9.7	0.45	1728	4.19	36.7
	B4	277.20	1.50	3.0	0.2	781	8.3	0.49	1887	4.57	12.5
	B15	243.73	1.60	2.34	2.0	781	6.2	0.51	1956	5.04	9.1
2.	C10	314.08	1.60	2.58	10^{-3}	782	7.1	0.57	2201	5.70	8.0
	C5	342.58	1.60	1.86	1.0	781	8.3	0.53	2053	5.32	6.6
	$ST_{LSN}14$	297.03	1.50	6.39	0.5	793	7.6	0.57	2212	5.35	19.8
	B5	278.0	1.6	2.3	1.0	777	7.0	0.51	1976	5.10	8.74
3.	B8	311.85	1.6	3.3	0.2	785	7.2	0.56	2155	5.58	10.7
	B9	313.17	1.6	1.89	0.2	778	7.9	0.51	1972	5.08	7.2

1. Saturated with 96CO-4CO_2;
2. 0.149 wt-% O, 0.12 wt-% C added, topped up with 96CO-4CO_2, 5 minutes bubbling;
3. Saturated with 92CO-8CO_2

Run No.	Charge Mass	Nozzle Diameter	Length/ Diameter ratio	Tank pressure	ΔP_{total} average	Flow duration	Mean discharge coefficient	Mass Flux	Reynolds Number
-	(gram)	(mm)	-	(mmHg)	(mmHg)	(secs)	-	gm/ cm^2. sec	(10^3)
DEGASSED SILVER IN ROUGH NOZZLES									
SA4	375.96	1.8	10.47	10^{-3}	787	4.6	0.73	3203	19.2
SA9	402.93	2.09	9.56	10^{-3}	784	3.9	0.69	3013	20.85
DEGASSED MOLTEN IRON IN ROUGH NOZZLES									
G10	314.87	2.47	6.7	10^{-3}	791	3.5	0.48	1878	8.76
P6	350.17	1.76	3.32	1.0	776	7.1	0.53	2027	9.07

A.2

The following tables contain the data on the kinetics of nitrogen and carbon monoxide bubble growth in molten iron discharging into a vacuum chamber at $\sim$20 mmHg. A summary table (A.2-1) is given to indicate the gas solute and the experimental value of the slope of the curve obtained from the plot of diameter (2R) against the square root of time ($t^{\frac{1}{2}}$) for each bubble analysed..

BUBBLE GROWTH KINETICS

A.2.1.

Serial No.	Gas Solute	Experimental $4\beta D^{\frac{1}{2}}$ (mm $sec^{-\frac{1}{2}}$)
BG1	96CO - $4CO_2$	289
2	"	225
3	"	246
4	"	288
5	"	236
6	"	220
7	"	295
8	"	206
9	"	271
10	"	267
11	"	236
12	"	275
13	92CO - $8CO_2$	275
14	OFN	138
15	"	175
16	"	187
17	"	169
18	"	181

A.2.2.

BG1

Bubble Diameter 2R(mm)	$t^{\frac{1}{2}}$ ($sec^{\frac{1}{2}}$)
2.71	0
8.97	.032
11.85	.045
14.47	.055
17.28	.063
19.99	.071
22.34	.077
24.45	.084
26.30	.089
27.77	.095

BG2	BG14	
Bubble Diameter 2R (mm)		$t^{\frac{1}{2}}$ ($sec^{\frac{1}{2}}$)
3.25	3.18	0
3.29	4.18	.022
3.97	4.83	.031
4.45	5.99	.038
5.89	7.19	.044
8.42	7.91	.049
9.19	8.49	.054
9.63	8.84	.058
10.72	9.35	.062
11.32	9.70	.066
11.95	10.49	.069
-	10.63	.072

BG3	BG4	BG5	
Bubble Diameter 2R (mm)			$t^{\frac{1}{2}}$ ($sec^{\frac{1}{2}}$)
2.95	3.25	3.39	0
3.18	3.46	4.25	.022
4.55	4.62	5.92	.032
5.78	6.06	7.42	.039
7.15	7.19	8.51	.045
8.31	8.86	10.02	.050
9.74	10.09	10.97	.055
10.74	11.25	12.25	.059
12.18	12.32		.063
BG6	BG8	BG9	$t^{\frac{1}{2}}$ ($sec^{\frac{1}{2}}$)
3.39	3.97	3.29	0
5.38	4.45	5.27	.022
6.82	5.92	6.84	.032
8.35	7.56	8.14	.039
9.65	8.72	9.23	.045
10.44	9.93	10.23	.050
11.53	10.74	11.74	.055
12.99	11.53	13.11	.059
13.90	12.04	13.85	.063
	12.67	15.06	.067
	13.69	16.15	.071
	14.34		.074
	15.20		.076
	15.96		.081
	16.57		.084
	16.91		.087

BG7	BG10	BG12	
Bubble diameter 2R(mm)			$t^{\frac{1}{2}}(sec^{\frac{1}{2}})$
3.30	3.32	4.80	0
5.20	4.71	7.08	.022
7.52	6.47	9.07	.032
9.37	8.05	11.09	.039
11.32	9.14	12.09	.045
12.04	10.74	13.27	.050
12.97	11.67	14.62	.055
14.71	12.90	16.12	.059
15.99	14.13	16.73	.063
16.70	15.15	17.52	.067
17.33	16.05	18.88	.071
18.72	17.24	19.60	.074
19.37	17.86	20.30	.076
20.32	18.72	21.41	.081
21.00	19.44	22.27	.084
22.11	20.32	22.99	.087
22.85	21.41	23.87	.089
23.78	22.16	24.87	.092
24.80	22.92	25.22	.095
25.52	23.50	26.31	.098
26.40		27.63	.100
26.89		27.96	.103
27.82		28.81	.105
28.54		29.19	.107
29.14			.110

BG11	BG18	
Bubble diameter 2R(mm)		$t^{\frac{1}{2}}(sec^{\frac{1}{2}})$
3.39	4.59	0
4.48	6.82	.022
5.92	13.62	.032
7.22	14.89	.039
8.84	15.71	.045
9.70	16.33	.050
10.81	17.38	.055
12.02	18.14	.059
	18.91	.063
	19.84	.067
	20.25	.071
	21.00	.074
	21.30	.076

BG 13

Bubble Diameter 2R(mm)	$t_{\frac{1}{2}}$ sec
4.52	0
6.23	.020
7.56	.029
9.24	.035
10.87	.041
11.96	.046
13.08	.050
13.93	.054
14.65	.058
15.37	.061
16.89	.065
18.06	.068
19.11	.071
20.04	.074
21.22	.076
22.22	.079
23.04	.082
23.47	.084
24.11	.087

BG15	BG16	BG17	
Bubble diameter 2R(mm)			$t^{\frac{1}{2}}(sec^{\frac{1}{2}})$
3.74	6.24	3.94	0
7.89	7.26	7.87	.020
9.91	7.84	9.86	.028
10.72	8.19	10.32	.035
11.07	8.49	10.90	.040
11.76	9.26	11.16	.045
12.04	9.37	11.97	.049
12.71	9.86	12.09	.053
13.91	10.35	12.92	.057
14.13	11.11	13.76	.060
14.42	11.41	14.34	.063
15.36	11.48		.066
	12.34		.069
	13.20		.072
	14.08		.075
	14.71		.077
	14.99		.080
	15.78		.082
	15.85		.085
	16.22		.087

A.3. GAS SATURATION OF IRON MELT.

The review of the kinetic factors included in the earlier part of this thesis (section 3.2) was to provide background information for the experimental determination of the mass transfer coefficients of different gases dissolved in molten iron.

It was shown in section 3.2.2 that

$$[\log(1 - C_b/C_s)] = \frac{K_L A.t}{2.303V} \quad \ldots\ldots\ldots 3.37$$

By standardising the bubbling procedure, mass of charge, crucible dimensions, melt temperature and by measuring K_L for nitrogen it should be possible to estimate the times required to attain the various levels of equilibrium saturation for the dissolution of other gases in molten iron since

$$K_{L_{(1)}}/K_{L_{(2)}} \quad (D_1/D_2)^{\frac{1}{2}} \quad \ldots\ldots\ldots 3.38$$

where there are uncertainties in the accurate estimation of the effective melt/gas interfacial area, A^1 such when the melt is bubble-agitated the slope of $[\log(1-C_b/C_s)]$ against bubbling duration provides a means of evaluating $K_L A^1/V$.

The orifice through the base of an old alumina crucible was blocked with alumina cement. A charge of 300 gram iron was melted. The saturation procedure

was as described in section 4.2.12. In these experiments nitrogen was bubbled for 5,10,15,20 minutes and a separate run was carried out in which the charge was degassed. Each melt was 'killed' with aluminium wire and solidified in situ. Drillings were taken from various sections of the solidified ingot and analysed for nitrogen by both vacuum fusion and wet chemical techniques. The results are shown in tables A.3.1 and A.3.2.

These results are surprisingly inconsistent. However two out of the four runs (FeN5, FeN15) showed rapid saturation of the melt while the less rapid ones indicate a degree of saturation (C_b/C_s) greater than 85% after thirty minutes bubbling.

The results indicate that the failure of the nitrogen saturated iron to break up had nothing to do with the gas content of the melt.

Since the diffusivities of $\underline{H}$, $\underline{C}$, $\underline{O}$ are higher than that of nitrogen (table 6.7) the iron melts containing these solutes must have been fully saturated after thirty minutes of bubbling.

Sample No.	Bubbling duration (mins)	Nitrogen analysis (10^{-3} wt-%)		
		By vacuum fusion		Duplicate by wet chemical method
		(i)	(ii)	
FeNo	0	6	6	8
FeN5	5	39	38	41
FeN10	10	11	11	13
FeN15	15	40	40	49
FeN20	20	25	25	26

TABLE A.3.1

RESULTS ON NITROGEN SATURATION OF IRON MELTS.

Sample No.	$(K_L A^1/V)$ $(10^{-3} sec^{-1})$
FeN5	6.46
FeN10	0.46
FeN15	2.43
FeN20	1.45

TABLE A.3.2

RESULTS ON NITROGEN SATURATION OF IRON MELTS.

ACKNOWLEDGEMENT

Sincere appreciation is extended to Dr. D.G.C. Robertson for his general encouragement, guidance and thorough supervision.

The advice and assistance of Mr. Roy Baxter, Mr. Alec Neve and their colleagues in the design and fabrication of the main apparatus are gratefully acknowledged.

Mr. Philip Wilson worked as a technician on the project from April 1975. He displayed perseverance and skill throughout the difficult times and contributed significantly to the programme. His services are gratefully acknowledged. The same goes for Mrs. Walker and Mr. J. Tipple who efficiently typed the thesis and prepared the tracings respectively.

I must express my profound gratitude to the members of my family, and those friends and relations who readily agreed to take on the supervision of the education of my children and brothers. I offer my unqualified gratitude to those affected by my choice of 'adventure' and who accepted my prolonged absence from home, particularly my children.

The University of Ife, Nigeria, provided the sponsorship for this work. The opportunities thus offered me are gratefully acknowledged.

R E F E R E N C E S

REFERENCES.

1. Winkler O. and Bakish R., Vacuum Metallurgy, Elsevier Publishing Company, Amsterdam - London - New York, 1971.

1a. Ibid, Chapter 4, page 337-463.

2. Herbert W.M.P., Vacuum degassing of stainless and alloy steels, Iron and Steel Engineer, 43, 131-133, (1966).

3. London University: Regulations for Internal Students proceeding to Higher Degrees.

4. Richards, E.J.(Panel Chairman), Academic - Industrial collaboration in engineering research, A Report to the Engineering Board, Science Research Council, London.

4a. Fishlock, D., Glad tidings for research, The Financial Times, ppl3, Jan 21, 1976.

5. Warner, N.A., Vacuum treatment of molten metals, Imperial College Report, June 1967.

5a. Warner, N.A., Stream break-up in vacuum degassing, JISI, 207, 44-50, (1969).

6. Baxter, R.T., Behaviour of liquid metal streams containing dissolved gases in vacuum. Report in the Department of Metallurgy, Imperial College, (July 1969).

7. Mizoguchi, S., A study of the stream degassing process using the silver-oxygen system. Ph.D. thesis, University of London, (November 1972).

8. Eisenklam, P., Hooper, P.C. The flow characteristics of laminar and turbulent jets of liquid. Interim Report, Imperial College, JRL, No.42, (September 1958).

9. Min, T.C., Fauske, H.K., Petrick, M. Effect of flow passages on two-phase critical flow. Ind. and Eng. Chem. Fundamentals, 5, 50-55, (1966).

10. Charan, V. Two-phase non-equilibrium flow of dichlorodifluoromethane through nozzles. Ph.D. thesis, University of London, (1967).

11. Silver, R.S., Mitchell, J.A., The discharge of saturated water through nozzles. Trans. N - E Cst. Inst. Engrs. Shipb., 62, 45-56, (1962).

12. Simpson, H.C., Silver, R.S., Theory of one-dimensional two-phase homogeneous non-equilibrium flow. Pro. Instn. Mech. Engrs. 45-56, (1962).

13. Fauske, H., Critical two-phase, steam-water flows, Pro. of Heat Transfer and Fluid Mechanics Institute, 79-89, (1961).

14. Chedaille, J., Sivet, M., Saint-Martin, L., Busette pour la coutee sous vide de lacier Revue de Metallurgie, 60, 663-668, 1963.

15. Tangreen, R.F., Dodge, C.H., Seifert, H.S., Compressibility effects in two-phase flow, Journal Appl. Phys. 20, 637-645, 1949.

16. Meadowcroft, T.R., Milbourne R.J., A new process for continuously casting aluminium killed steel. J. Met. 23, 11-17, 1971.

17. Hornak J.N., Orehoski, M.A., Vacuum Casting of Steel, J. Met., 10, 471-475, 1958.

18. Stream degassing meeting, Corporate Laboratory, and visit to the River Don Works, Special Steel Division, B.S.C., Sheffield, 29th March, 1973.

19. Knagg, K., Steel, Peech and Tozer, Special Steel Division, B.S.C., Sheffield, private works visit and communication, June 1969.

20. The Vacuum Degassing of Steel, I.S.I. Special Report no. 92, 8, 1965.

20a. Ibid, page 50.

20b. Ibid, page 24.

20c. Ibid, page 29.

21. Hokansen, A.E., Trans. Vac. Met. Conf. 1963. Ed. Bunshah, R.F., AVS, Boston, Mass., 238, 1964.

21a. Kraus, T., Ibid page 50.

21b. Meadowcroft, T.R., Elliott, J., Ibid pp 1-32.

21c. Fruehan, R.J., Rates of several gas-metal reactions in the Q-BOP, Ironmaking and Steelmaking, Vol. 3, No. 1, 33-37, 1976.

21d. Dukelow, D.A., Gower, R.C., Pilot plant data for the rates of several gas-metal reactions in Q-BOP, U.S. Steel Research Laboratory, Monroeville, Pa., Unpublished work.

22. Ward, R.G., An introduction to the physical chemistry of iron and steelmaking, page 177.

22a. Ibid, page 186.

22b. Ibid, page 179.

22c. Ibid, page 187.

22d.

23. Marshall, S., Chipman, J., Trans. A.S.M., 695, 1942.

24. Chipman, J., Elliott, J.F., Electric Furnace Steelmaking, Vol. II, 95-175, 1963.

25. Distin, P.A., et al, JISI, 206, 821-832, 1968.

25a. Delve, F.D., et al, JISI, 206, 1218, 1968.

26. Baker, L.A., et al, Trans. AIME, 230, 1228, 1964.

27. King, T.B., Vacuum Metallurgy, (ed. Bunshah), Reinhold, New York, 35, 1958.

28. Riddiford, A.C., J. Phys. Chem., 56, 746, 1952.

29. Astarita, G., Mass transfer with chemical reaction, Elsevier, Amsterdam, page 4, 1967.

30. Richardson, F.D., Physical Chemistry of Melts in Metallurgy, Vol. 2, Academic Press, London, New York, pp. 414.

31. Bradshaw, A.V., Kinetic aspects of vacuum refining, Le Vide, 138, 376-415, 1968.

32. El-Kaddah, N.H., Carbon-oxygen equilibrium and homogeneous nucleation of carbon monoxide bubbles in levitated molten iron. Ph.D. thesis, University of London, 1975.

33. Paurise, J.C., Circ. Inform. Techn. 22, 125, 1965.

34. Bennette, G.H.J., et al, JISI, 195, 195, 1960.

35. Davies et al, In Chemical Metallurgy of Iron and Steel, A symposium organised by the Iron and Steel Institute and Sheffield University, pp 107, 1968.

36. Scriven, L.R., On the dynamics of Phase Growth, Chem. Eng. Science, 10, 1-13, 1959.

37. Gale, R.S., The nucleation and growth of bubbles in supersaturated solution of gases in viscous liquids, Ph.D. thesis, University of London, 1966.

38. Rosner, D.E., Epstein, M., Effects of interface kinetics, capillarity and solute diffusion on bubble growth rates in highly saturated liquids, Chem. Eng. Sci., 27, 69-88, 1972.

39. Keith, F.W., Hixson, A.N. Ind. Eng.Chem., 47, 258-267, 1955.

40. Merrington, A.C., Richardson, E.G., Pro.Phys. Soc. London, 59, 1, 1947.

41. Lord Rayleigh, Proc. Lond. Math. Soc., 10, 4, (1878-1879).

42. Lord Rayleigh, Phil. Mag. 48, 321, 1899.

43. Lord Rayleigh, Phil. Mag. 34, 177, 1892.

44. Jackson, A., Oxygen steelmaking for steelmakers, London, Newness - Butterworth, 2nd Edition.

45. Norton, F.H., Refractories, fourth edition, McGraw Hill Book Company.

46. Lucas, L.D. et al. Physical Chemistry of Process Metallurgy, The Richardson Conference, IMM Publication, 187-195, 1974.

47. Fisher, W-A, Hoffmann, A., Arch. Eisenhüttenw, 27, 563, 1956.

48. Brotzmann, K., Arch. Eisenhüttenw, 31, 67, 1960.

49. Elliott, J.F. et al. Thermochemistry for Steelmaking Vol. II, Reading, Mass.; Addison-Wesley 1963.

50. Sims, C. Trans. AIME, 215, 367, 1959.

50a. Ibid, 224, 1288-1289, 1962.

51. Levin, M.E., Robbins, C.R., McMurdie, H.F., Phase Diagrams for Ceramists, page 43, Fig. 26.

52. McLean, A., Ward, R.G., Thermodynamics of hercynite formation JISI, pp 8-11, Jan. 1966.

53. Tenenbaum, M., Nonmetallic phases in low-carbon sheet steels of various origins. Trans. Met. Soc. AIME, 245, 1675-1697, 1969.

54. Pillay, T.C.M. et al, J. Amer. Ceram. Soc., 43, 583-5, 1960.

55. Brokloff, J.E., Ph.D. thesis, University of Michigan, 1964.

56. Marchal, R., Sur la stabilite des ecoulements dans les tuyauteries parcourues par une emulsion de liquide et de gaz, Compt. Rend. Acad. Sci., 254, 1962, 2524-2526.

57. Vennard, J.K., Elementary fluid mechanics, 4th Edition, New York. London, John Wiley & Sons, Inc. pp 283.

58. Colebrook, C.F., Turbulent flow in pipes with particular reference to the transition region between the smooth and rough pipe laws, Jour. Inst. Civil Engrs. London, pp 133, Feb. 1939.

59. Solar, M.Y., Guthrie R.I.L., Metallurgical transactions, 3, March 1972, 713.

60. Levine, H.S., Formation of vapour nuclei in high temperature melts. J. of Phys. Chem., 76, 2609-2614, 1972.

61. Szekely, J. and Martins, G.P., On spherical phase growth in multicomponent systems. Trans. Met. Soc. AIME, 245, 1741, August 1969.

61a. Ibid, Non-equilibrium effects in the growth of spherical bubbles due to diffusion. Chem.Eng.Sci., Vol. 26, 147-159, (1971).

62. Winterton, R.H.S., Sizes of bubbles produced by dissolved gas coming out of solution on the walls of pipes in flowing systems. Chem. Eng. Sci., Vol 27, 1223-1230, (1972).